

# NNPDFPOL2.0: unbiased global determination of polarized PDFs and their uncertainties at next-to-next-to-leading order

Juan Cruz-Martinez<sup>1</sup>, Toon Hasenack<sup>2,3</sup>, Felix Hekhorn<sup>4,5</sup>, Giacomo Magni<sup>3,6</sup>, Emanuele R. Nocera<sup>7</sup>,  
Tanjona R. Rabemananjara<sup>3,6</sup>, Juan Rojo<sup>3,6</sup>, Tanishq Sharma<sup>7</sup>, and Gijs van Seeverster<sup>2,3</sup>

<sup>1</sup>*CERN, Theoretical Physics Department, CH-1211 Geneva 23, Switzerland*

<sup>2</sup>*Institute for Theoretical Physics, Utrecht University, Leuvenlaan 4, 3584 CE Utrecht*

<sup>3</sup>*Nikhef Theory Group, Science Park 105, 1098 XG Amsterdam, The Netherlands*

<sup>4</sup>*University of Jyväskylä, Department of Physics, P.O. Box 35, FI-40014 University of Jyväskylä, Finland*

<sup>5</sup>*Helsinki Institute of Physics, P.O. Box 64, FI-00014 University of Helsinki, Finland*

<sup>6</sup>*Department of Physics and Astronomy, Vrije Universiteit, NL-1081 HV Amsterdam*

<sup>7</sup>*Dipartimento di Fisica, Università degli Studi di Torino and  
INFN, Sezione di Torino, Via Pietro Giuria 1, 10125 Torino, Italy*

## Abstract

We present NNPDFPOL2.0, a new set of collinear helicity parton distribution functions (PDFs) of the proton based on legacy measurements of structure functions in inclusive neutral-current longitudinally polarised deep-inelastic scattering (DIS), and of  $W$ -boson, single-inclusive, and di-jet production asymmetries in longitudinally polarised proton-proton collisions. The determination is accurate to next-to-next-to-leading order in the strong coupling, and includes heavy quark mass corrections in the analysis of DIS data. Uncertainties due to missing higher-order corrections are systematically incorporated by means of a covariance matrix determined by scale variations. NNPDFPOL2.0 is based on a machine learning methodology, that makes use of Monte Carlo sampling for the representation of uncertainties into PDFs, of a neural network for the parametrisation of PDFs, of stochastic gradient descent for the optimisation of PDF parameters, and of hyperoptimisation for the selection of the best fitting model. We study the impact on PDFs of higher-order corrections, of the positivity constraint, and of the data. We demonstrate two phenomenological applications of NNPDFPOL2.0, specifically the determination of the proton spin fraction carried by gluons and quarks, and of theoretical predictions for single-hadron production in longitudinally polarised DIS and proton-proton collisions.

# Contents

|          |   |           |
|----------|---|-----------|
| <b>1</b> | <b>Introduction</b>   | <b>2</b>  |
| <b>2</b> | <b>Experimental and theoretical input</b>                               | <b>4</b>  |
| 2.1      | The NNPDFPOL2.0 data set . . . . .                                      | 4         |
| 2.2      | Perturbative accuracy . . . . .   | 8         |
| <b>3</b> | <b>Fitting methodology</b>  | <b>11</b> |
| 3.1      | Parametrisation . . . . .   | 11        |
| 3.2      | Parameter optimisation . . . . .  | 12        |
| 3.3      | Hyperparameter optimisation . . . . .                                   | 14        |
| <b>4</b> | <b>Results</b>  | <b>17</b> |
| 4.1      | Fit quality, parton distributions, and perturbative stability . . . . . | 18        |
| 4.2      | Comparison to NNPDFPOL1.1 and to other PDF sets . . . . .               | 22        |
| 4.3      | Dependence on the positivity constraint and on the data set . . . . .   | 26        |
| <b>5</b> | <b>Phenomenological applications</b>                                    | <b>28</b> |
| 5.1      | The spin content of the proton revisited . . . . .                      | 29        |
| 5.2      | Single-inclusive particle production . . . . .                          | 31        |
| <b>6</b> | <b>Summary and delivery</b>   | <b>31</b> |
| <b>A</b> | <b>Benchmark of the PINEAPPL grids</b>                                  | <b>34</b> |

## 1 Introduction

Helicity-dependent (polarised, henceforth) parton distribution functions (PDFs) [1] are defined as differences between the density of partons with spin aligned parallel or anti-parallel to the spin of the proton to which they belong. The interest in their determination is mainly related to the fact that their lowest moments are proportional to the proton axial currents, which express the fraction of proton spin carried by gluons and quarks [2]. In spite of impressive experimental and theoretical investigations over the past thirty years, knowledge of polarised PDFs remains limited in comparison to their unpolarised counterparts, in particular concerning the distributions of sea quarks and gluons. This fact hinders the fundamental understanding of proton spin decomposition in the framework of Quantum Chromodynamics (QCD) [3].

The Electron-Ion Collider (EIC) [4, 5], expected to start its operations in the early 2030s, is designed to revolutionise this state of affairs. The EIC will have the possibility to collide polarised proton and lepton beams, so to measure the polarised inclusive and semi-inclusive deep-inelastic scattering (DIS) structure functions, to which polarised PDFs are related through factorisation theorems [6]. These measurements are forecast to cover an unprecedented range of proton momentum fraction  $x$  and virtuality  $Q^2$  (see *e.g.* Fig. 1 in [1]) while attaining percent-level precision (see *e.g.* Sect. II in [4]). These prospects call for a matching accuracy of the corresponding theoretical predictions, which require in turn an improvement in the accuracy of the perturbative computations involving polarised protons in the initial state, and of the polarised PDF determinations extracted from these.

Concerning the accuracy of perturbative computations, significant progress has been made to incorporate next-to-next-to-leading order (NNLO) QCD corrections into the matrix elements of a range of polarised observables. For polarised inclusive DIS, the massless polarised structure function  $g_1$  has been known at NNLO for a long time [7]. Very recently, N<sup>3</sup>LO corrections have been computed [8], as have NNLO massive contributions [9], their asymptotic limit [10–17], and NNLO parity-violating massless polarised structure functions [18]. For polarised semi-inclusive DIS, the massless polarised structure function  $g_1^h$  has been determined up to NNLO lately: first using an approximation based on the threshold resummation formalism [19]; then exactly using various analytical methods [20–22]. Finally, NNLO corrections have also been obtained for  $W$ -boson production in polarised proton-proton collisions [23]. In the last years, a similar effort was put to compute NNLO corrections to polarised splitting functions entering DGLAP evolution equations [24–27], and their matching conditions for heavy quarks [14].

Concerning the accuracy of PDF determinations, a first polarised NNLO set was determined some time ago by analysing only inclusive DIS data [28]. This data does not allow for a separation of polarised quark and antiquark PDFs and has a limited sensitivity to the polarised gluon PDF. Therefore, other polarised PDF sets, *e.g.* DSSV14 [29] and NNPDFPOL1.1 [30], despite being accurate only to next-to-leading order (NLO), have been more widely used so far. The NNLO analysis presented in [28] has been followed by two newer NNLO determinations last year: MAPPDFPOL1.0 [31] and BDSSV24 [32]. These two determinations incorporate experimental data other than inclusive DIS in a NNLO analysis. Both of them, however, are approximated. The former [31], which is based on polarised inclusive and semi-inclusive DIS measurements, relies on the approximation of [19] to analyse the latter. The necessary fragmentation functions (FFs) are determined consistently using the same approximation. The latter [32], which is based on polarised inclusive and semi-inclusive DIS measurements and on single-inclusive jet, gauge boson, and hadron production measurements in polarised proton-proton collisions, is based on the same approximation. The necessary FF sets are used at NLO. Unknown NNLO corrections in the matrix elements of single-inclusive jet and hadron production in polarised proton-proton collisions are neglected. Whereas the more extended data set provides a better sensitivity to polarised PDFs, these approximations introduce additional theory uncertainties which are not accounted for.

As a further step towards the understanding of the polarised partonic structure of the nucleon, in this paper we present NNPDFPOL2.0, a new determination of the proton polarised PDFs based on the NNPDF methodology [33]. This determination improves our previous one, NNPDFPOL1.1 [30], in three main respects, which set it apart from the other two recent NNLO fits of polarised PDFs [31, 32] described above.

1. We significantly extend the range of fitted data sets. We specifically consider measurements of polarised inclusive lepton-nucleon DIS, including legacy measurements from HERMES and COMPASS, and measurements of  $W$ -boson, single-inclusive jet, and di-jet production from STAR. Many of these data sets have become available after the publication of NNPDFPOL1.1, and represent the legacy of experimental programs that are now completed. In contrast to NNPDFPOL1.1, we drop measurements of open charm production, which were demonstrated to be immaterial [30, 34]. As in NNPDFPOL1.1, we do not consider measurements of single-hadron production in polarised DIS and polarised proton-proton collisions, the analysis of which requires explicit knowledge of the FFs.
2. We incorporate higher-order corrections to both the DGLAP evolution and to the hard cross sections, whenever available, up to NNLO in the strong coupling. We likewise incorporate heavy quark mass corrections in the analysis of polarised inclusive DIS structure functions according to the FONLL general-mass scheme [35] as implemented in [36, 37]. We account for the uncertainties associated to missing higher-order QCD corrections (MHOU) by means of the methodology developed in [38–40], whereby MHOU are treated through a theory covariance matrix determined by scale variations. Theoretical predictions are computed with the PINELINE [41] framework, which combines various pieces of open-source software specifically designed for PDF determination: EKO [42, 43], for the evolution of PDFs; YADISM [44, 45], for the computation of inclusive DIS structure functions; and PINEAPPL [46, 47] for the delivery of theoretical predictions as PDF-independent fast interpolation grids. Here this computational framework has been extended to deal with polarised observables, including in the case in which unpolarised and polarised PDFs ought to be used simultaneously, such as in the computation of spin asymmetries.
3. We deploy the machine-learning methodology developed in [33]. Whereas the core ingredients of the fitting methodology are the same as in NNPDFPOL1.1 (a Monte Carlo sampling for uncertainty representation and a neural network for PDF parametrisation), all aspects of the parametrisation and optimisation (such as the neural network architecture or the choice of minimisation algorithm) are now selected through a hyperparameter optimisation procedure [48, 49], which consists in an automated scan of the space of models. To ensure that the optimal model does not lead to overfitted PDFs, a  $k$ -folding partition is used, which verifies the effectiveness of any given model on sets of data excluded in turn from the fit. In contrast to NNPDFPOL1.1, all data sets are fitted, instead of being partly fitted and partly being incorporated by means of Bayesian reweighting [50, 51]. Furthermore, model optimisation is realised through a gradient descent algorithm instead of a genetic algorithm.

The NNPDFPOL2.0 polarised PDF sets are released at LO, NLO and NNLO without and with MHOU for a single value of the strong coupling,  $\alpha_s(m_Z) = 0.118$ . The NNLO set remains approximate, insofar

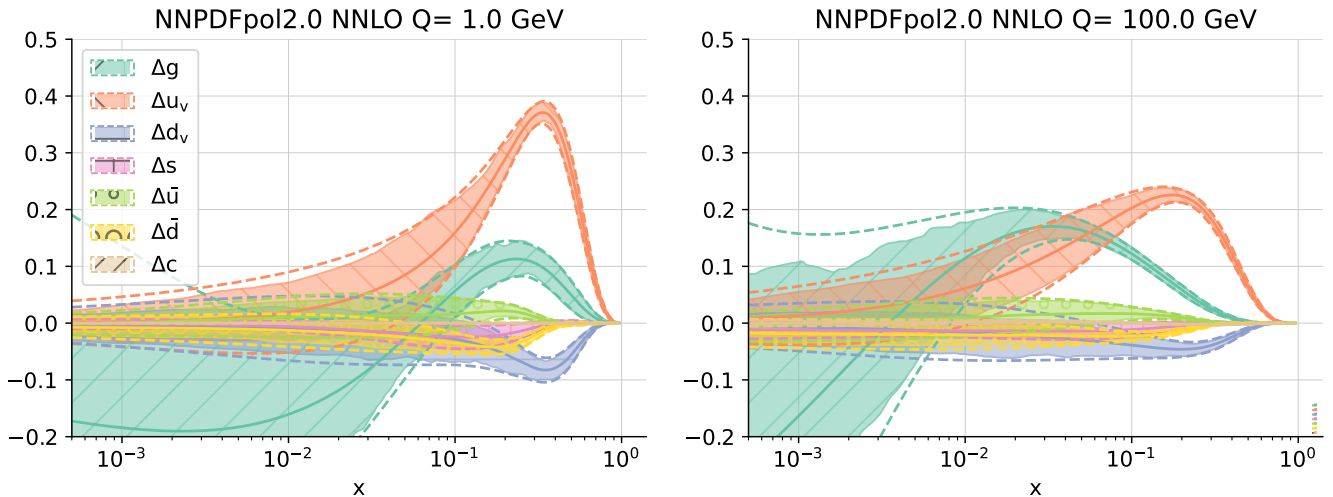


**Figure 1.1.** The NNPDF<sub>POL</sub>2.0 NNLO PDFs at  $Q = 1$  GeV (left) and  $Q = 100$  GeV (right). Bands with dashed contours correspond to one-sigma uncertainties, whereas bands with continuous contours correspond to 68% confidence-level uncertainties.

as NNLO corrections to single-inclusive jet and di-jet production asymmetries in polarised proton-proton collision are unknown. The corresponding PDFs, which represent the main outcome of this paper, are displayed in Fig. 1.1. All parton sets are made available in the LHAPDF format [52, 53] as ensembles of both 1000 and 100 Monte Carlo replicas, the latter being obtained from compression of the former with the algorithm developed in [54, 55]. The open-source NNPDF software [56] has been extended to include the input and tools needed to reproduce the NNPDF<sub>POL</sub>2.0 sets presented here.

The structure of this paper is as follows. In Section 2 we present the experimental and theoretical input entering the NNPDF<sub>POL</sub>2.0 determination. In Section 3 we discuss the methodology deployed to determine it, focusing on how aspects of PDF parametrisation, optimisation, and hyperoptimisation are adapted to the polarised case. In Section 4 we present the NNPDF<sub>POL</sub>2.0 parton set, study its fit quality and perturbative stability, compare it to NNPDF<sub>POL</sub>1.1 and to other polarised PDF sets, and assess its dependence on the positivity constraint and on the data. In Section 5 we demonstrate two applications of NNPDF<sub>POL</sub>2.0, specifically on the determination of the spin content of the proton and on the computation of theoretical predictions for longitudinal spin asymmetries of single-inclusive hadron production in DIS and polarised proton-proton collisions. The conclusion and an outlook are provided in Section 6. The paper is completed by Appendix A, in which we present a benchmark of the numerical accuracy of the PINEAPPLE grids used in this work, specifically to analyse  $W$ -boson production spin asymmetries.

## 2 Experimental and theoretical input

In this section, we present the experimental and theoretical input entering the NNPDF<sub>POL</sub>2.0 determination. We first introduce the data set, describing the details of each measurement, and the computational tools used to obtain the corresponding theoretical predictions. We then discuss their perturbative accuracy, and specifically the way in which we account for MHOUs.

### 2.1 The NNPDF<sub>POL</sub>2.0 data set

The NNPDF<sub>POL</sub>2.0 determination is based on measurements of three different polarised observables: the structure function  $g_1$  in longitudinally polarised inclusive lepton-nucleon DIS; the longitudinal single-spin asymmetry  $A_L^{W^\pm}$  for  $W^\pm$ -boson production in polarised proton-proton collisions; and the longitudinal double-spin asymmetry  $A_{LL}^{1-;2\text{-jet}}$  for single-inclusive jet and di-jet production in polarised proton-proton collisions. The definition of these observables can be found, *e.g.*, in Sect. 3 of [57], and in Sect. 6.2.2 of [58]. We review the measurements that we include in NNPDF<sub>POL</sub>2.0 for each of these observables in turn.

**Polarised inclusive DIS structure function.** We include measurements performed by the EMC [59],

| Data set                    | Ref. | $N_{\text{dat}}$ | $x$              | $Q^2$ [GeV <sup>2</sup> ] | Theory |
|-----------------------------|------|------------------|------------------|---------------------------|--------|
| EMC $g_1^p$                 | [59] | 10 (10)          | [0.015, 0.466]   | [3.5, 29.5]               | YADISM |
| SMC $g_1^p$                 | [60] | 13 (12)          | [0.002, 0.48]    | [0.50, 54.8]              | YADISM |
| SMC $g_1^d$                 | [60] | 13 (12)          | [0.002, 0.48]    | [0.50, 54.80]             | YADISM |
| SMC low- $x$ $g_1^p/F_1^p$  | [61] | 15 (8)           | [0.00011, 0.121] | [0.03, 23.1]              | YADISM |
| SMC low- $x$ $g_1^d/F_1^d$  | [61] | 15 (8)           | [0.00011, 0.121] | [0.03, 22.9]              | YADISM |
| COMPASS $g_1^p$             | [62] | 17 (17)          | [0.0036, 0.57]   | [1.1, 67.4]               | YADISM |
| COMPASS $g_1^d$             | [63] | 15 (15)          | [0.0046, 0.567]  | [1.1, 60.8]               | YADISM |
| E142 $g_1^n$                | [64] | 8 (8)            | [0.035, 0.466]   | [1.1, 5.5]                | YADISM |
| E143 $g_1^p$                | [65] | 28 (27)          | [0.035, 0.466]   | [1.27, 9.52]              | YADISM |
| E143 $g_1^d$                | [65] | 28 (27)          | [0.031, 0.749]   | [1.27, 9.52]              | YADISM |
| E154 $g_1^n$                | [66] | 11 (11)          | [0.017, 0.024]   | [1.2, 15.0]               | YADISM |
| E155 $g_1^p/F_1^p$          | [67] | 24 (24)          | [0.015, 0.750]   | [1.22, 34.72]             | YADISM |
| E155 $g_1^n/F_1^n$          | [67] | 24 (24)          | [0.015, 0.750]   | [1.22, 34.72]             | YADISM |
| HERMES $g_1^n$              | [68] | 9 (9)            | [0.033, 0.464]   | [1.22, 5.25]              | YADISM |
| HERMES $g_1^p$              | [69] | 15 (15)          | [0.0264, 0.7248] | [1.12, 12.21]             | YADISM |
| HERMES $g_1^d$              | [69] | 15 (15)          | [0.0264, 0.7248] | [1.12, 12.21]             | YADISM |
| JLab E06 014 $g_1^n/F_1^n$  | [70] | 6 (4)            | [0.277, 0.548]   | [3.078, 3.078]            | YADISM |
| JLab E97 103 $g_1^n$        | [71] | 5 (2)            | [0.160, 0.200]   | [0.57, 1.34]              | YADISM |
| JLab E99 117 $g_1^n/F_1^n$  | [72] | 3 (1)            | [0.33, 0.60]     | [2.71, 4.83]              | YADISM |
| JLab EG1 DVCS $g_1^p/F_1^p$ | [73] | 47 (21)          | [0.154, 0.578]   | [1.064, 4.115]            | YADISM |
| JLab EG1 DVCS $g_1^d/F_1^d$ | [73] | 44 (19)          | [0.158, 0.574]   | [1.078, 4.666]            | YADISM |
| JLab EG1B $g_1^p/F_1^p$     | [74] | 787 (114)        | [0.0262, 0.9155] | [0.0496, 4.96]            | YADISM |
| JLab EG1B $g_1^d/F_1^d$     | [74] | 2465 (301)       | [0.0295, 0.9337] | [0.0496, 4.16]            | YADISM |

**Table 2.1.** The polarised inclusive DIS measurements included in NNPDFPOL2.0. We denote each data set with the name used throughout this paper, and we indicate its reference, number of data points before (after) applying kinematic cuts, kinematic coverage (before cuts), and the piece of software used to compute the corresponding theoretical predictions.

SMC [60, 61], and COMPASS [62, 63] experiments at CERN, by the E142 [64], E143 [65], E154 [66], and E155 [67] experiments at SLAC, by the HERMES experiment at DESY [68, 69], and by the Hall A [70–72] and CLAS [73, 74] experiments at JLab. All of these experiments provide data for the polarised inclusive DIS structure function  $g_1$ , reconstructed from the longitudinal double-spin asymmetry (see, *e.g.*, Sect. 2.1 in [57] for details), except SMC low- $x$ , E155, Hall A, and CLAS, which instead provide data for  $g_1$  normalised to the unpolarised inclusive structure function  $F_1$ . The details of the measurements, including their kinematic coverage in the proton momentum fraction  $x$  and virtuality  $Q^2$ , are summarised in Table 2.1. In comparison to NNPDFPOL1.1, we update the COMPASS data with the legacy measurements of [62, 63], which combine events recorded in 2007 and 2011, and we add the JLab Hall A [70–72] and CLAS [73, 74] data. Note also that in NNPDFPOL1.1 we reconstructed  $g_1$  from the measured longitudinal and transverse spin asymmetries, assuming either a vanishing structure function  $g_2$  or relating  $g_2$  to  $g_1$  with the Wandzura-Wilczek relation [75]. Here we use instead the values of  $g_1$  reconstructed in the corresponding experimental papers. The two procedures lead to differences that are smaller than the uncertainty propagated by us or estimated in the experimental measurements, therefore we deem them to be equivalent.

We compute the corresponding theoretical predictions with YADISM [44], which we have developed to handle the computation of the polarised structure function  $g_1$  and interfaced to PINEAPPL. Predictions are accurate up to NNLO and include charm-quark mass corrections through the FONLL general-mass variable-flavour-number scheme [35], recently extended to the case of polarised structure functions [36]. Target mass corrections are also included as explained in Appendix B of [36]. We apply kinematic cuts on the virtuality  $Q^2$  and on the invariant mass of the final state  $W^2$ , by requiring  $Q^2 \geq Q_{\text{min}}^2 = 1.0 \text{ GeV}^2$  and  $W^2 \geq W_{\text{min}}^2 = 4.0 \text{ GeV}^2$ . These cuts remove, respectively, the region

| Data set         | Ref. | $N_{\text{dat}}$ | $\eta_\ell$      | $\sqrt{s}$ [GeV] | Theory |
|------------------|------|------------------|------------------|------------------|--------|
| STAR $A_L^{W^+}$ | [77] | 6                | $[-1.25, +1.25]$ | 510              | [23]   |
| STAR $A_L^{W^-}$ | [77] | 6                | $[-1.25, +1.25]$ | 510              | [23]   |

**Table 2.2.** Same as Table 2.1 for  $W^\pm$ -boson production data. The piece of software used for the computations is the version of MCFM developed in [23] and modified to produce PINEAPPL grids, see also Appendix A.

where perturbative QCD becomes unreliable due to the growth of the strong coupling, and the region where dynamical higher-twist corrections in the factorisation of  $g_1$  (which we do not include) may become sizeable. The cut on  $W^2$  also suppresses contributions from the resonance production region. Nuclear corrections affecting experiments that utilise a deuterium target are neglected. Whereas, in principle, they could be accounted for as described in [76], we consider that they be negligible in comparison to the precision of the experimental measurements. We therefore model the deuteron as the average of a proton and a neutron, and relate the PDFs of the latter to the PDFs of the former assuming exact isospin symmetry.

**$W$ -boson longitudinal single-spin asymmetry.** We include the measurement of the longitudinal single-spin asymmetry for  $W^\pm$ -boson production in polarised proton-proton collisions,  $A_L^{W^\pm}$ , performed by STAR at a centre-of-mass-energy  $\sqrt{s} = 510$  GeV [77]. The measurement combines events recorded during the 2011-2012 and 2013 runs, and it supersedes the previous one [78] used in NNPDFPOL1.1 [30]. It is given as a differential distribution in the lepton pseudorapidity  $\eta_{\ell^\pm}$ , which is strongly correlated to the  $W^\pm$ -boson rapidity, and it covers the interval  $-1.25 \leq \eta_{\ell^\pm} \leq +1.25$ . The details of the measurement are summarised in Table 2.2. We do not include measurements of the longitudinal single-spin asymmetry for  $W^\pm + Z^0$ -boson production,  $A_L^{W^\pm+Z^0}$ , measured by PHENIX [79], nor of the longitudinal double-spin asymmetry for  $W^\pm$ -boson production,  $A_{LL}^{W^\pm}$ , measured by STAR [77]. The reason being that these are expected to provide little constraints on polarised PDFs [30].

We compute the corresponding theoretical predictions with the modified version of MCFM [23], which we interfaced to PINEAPPL up to NLO, see Appendix A for a numerical benchmark. NNLO corrections to the partonic matrix elements are included, for both the unpolarised and polarised cross sections entering the asymmetry, by means of a bin-by-bin  $K$ -factor, which we compute with the same version of MCFM. We observe that NNLO corrections are generally small ( $K$ -factors are at most of  $\mathcal{O}(3\%)$ ) and that they are relatively independent from the lepton rapidity, consistently with Fig. 2 in [23]. This feature can be explained from the fact that cancellations occur between the polarised numerator and the unpolarised denominator in the asymmetry.

**Single-inclusive jet and di-jet longitudinal double-spin asymmetry.** We include measurements of the longitudinal double-spin asymmetry for single-inclusive jet and di-jet production in polarised proton-proton collisions,  $A_{LL}^{1;2\text{-jet}}$ , performed by PHENIX [80] at a centre-of-mass energy  $\sqrt{s} = 200$  GeV, and by STAR at centre-of-mass energies  $\sqrt{s} = 200$  GeV [81–83] and  $\sqrt{s} = 510$  GeV [84, 85]. The STAR measurements correspond, respectively, to the 2005-2006 [81], 2009 [82, 86, 87], 2012 [84], 2013 [85], and 2015 [83] runs. The measurements are given as distributions differential in the transverse momentum of the leading jet,  $p_T$ , in the case of single-inclusive jet production, and in the invariant mass of the di-jet system,  $m_{jj}$ , in the case of di-jet production. For di-jet production, we consider all the topologies provided. The details of these measurements, which include their kinematic coverage, are summarised in Table 2.3. The single-inclusive jet measurements presented in [80–82] were already included in NNPDFPOL1.1 [30].

We compute the corresponding theoretical predictions with the code presented in [88, 89], which we interfaced to PINEAPPL, and modified to handle the necessary kinematic cuts that define different di-jet topologies. For each data set, we use a jet algorithm consistent with that used in the corresponding experimental analysis. It was shown in [90] that single-inclusive jet and di-jet longitudinal double spin asymmetries are however rather insensitive to the jet algorithm, be it of cone- or  $k_t$ -type. Predictions are accurate up to NLO, given that NNLO corrections are not known. We therefore supplement them with a theory uncertainty, accounting for missing higher orders, estimated by varying

| Data set                            | Ref.     | $N_{\text{dat}}$ | $p_T$ or $m_{jj}$ [GeV] | $\sqrt{s}$ [GeV] | Theory   |
|-------------------------------------|----------|------------------|-------------------------|------------------|----------|
| PHENIX $A_{LL}^{1\text{-jet}}$      | [80]     | 6                | [2.4, 10.]              | 200              | [88, 89] |
| STAR $A_{LL}^{1\text{-jet}}$ (2005) | [81]     | 10               | [2.4, 11.]              | 200              | [88, 89] |
| STAR $A_{LL}^{1\text{-jet}}$ (2006) | [81]     | 9                | [8.5, 35.]              | 200              | [88, 89] |
| STAR $A_{LL}^{1\text{-jet}}$ (2009) | [82]     | 22               | [5.5, 32.]              | 200              | [88, 89] |
| STAR $A_{LL}^{2\text{-jet}}$ (2009) | [86, 87] | 33               | [17., 68.]              | 200              | [88, 89] |
| STAR $A_{LL}^{1\text{-jet}}$ (2012) | [84]     | 14               | [6.8, 55.]              | 510              | [88, 89] |
| STAR $A_{LL}^{2\text{-jet}}$ (2012) | [84]     | 42               | [20., 110.]             | 510              | [88, 89] |
| STAR $A_{LL}^{1\text{-jet}}$ (2013) | [85]     | 14               | [8.7, 63.]              | 510              | [88, 89] |
| STAR $A_{LL}^{2\text{-jet}}$ (2013) | [85]     | 49               | [14., 133.]             | 510              | [88, 89] |
| STAR $A_{LL}^{1\text{-jet}}$ (2015) | [83]     | 22               | [5.8, 34.]              | 200              | [88, 89] |
| STAR $A_{LL}^{2\text{-jet}}$ (2015) | [83]     | 14               | [20., 71.]              | 200              | [88, 89] |

**Table 2.3.** Same as Table 2.1 for single-inclusive jet and di-jet production data. The pieces of software used to compute the corresponding theoretical predictions [88, 89] have been extended to allow for the generation of PINEAPPL grids.

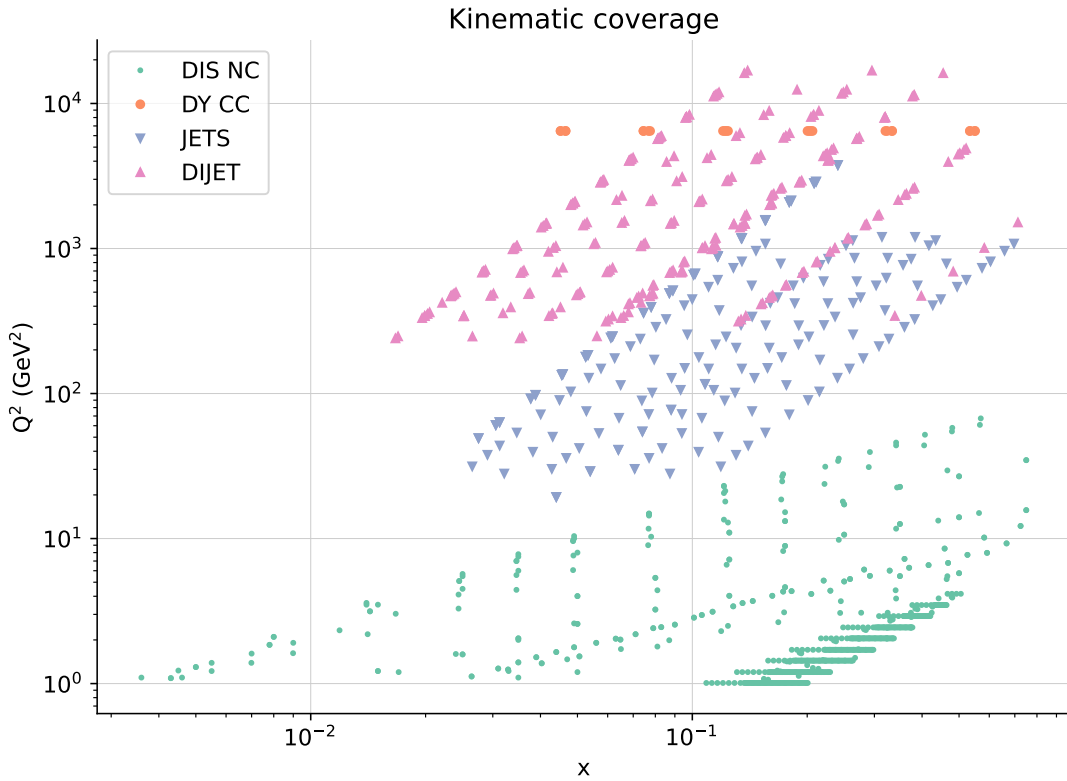


**Figure 2.1.** The kinematic coverage of the NNPDFPOL2.0 data set in the  $(x, Q^2)$  plane after applying kinematic cuts. The data sets are categorised as explained in Sect. 2.2.

the renormalisation scale, as we explain in Sect. 2.2.

The total number of data points included in NNPDFPOL2.0, after applying the aforementioned kinematic cuts, is  $N_{\text{dat}} = 951$ , irrespective of the perturbative accuracy of the determination. The corresponding kinematic coverage in the  $(x, Q^2)$  plane is displayed in Fig. 2.1. The data sets are categorised as explained in Sect. 2.2. For  $W^\pm$ -boson, single-inclusive jet, and di-jet production in polarised proton-proton collisions, LO kinematic relations have been used to determine  $x$  and  $Q^2$  from the relevant hadronic variables.

As can be seen from Fig. 2.1, the largest number of data points correspond to polarised inclusive DIS measurements. Given the available coverage in the virtuality  $Q^2$ , the scattering is mediated by a virtual photon, hence it is neutral current. At LO, these measurements are therefore sensitive only to the singlet PDF flavour combination  $\Delta\Sigma$  and, thanks to the fact that deuteron and proton targets are used, also to the non-singlet triplet  $\Delta T_3$ . The sensitivity to the gluon PDF, which enters only at higher orders, is

suppressed by powers of the strong coupling. Valence-like PDF flavour combinations are probed thanks to  $W^\pm$ -boson production measurements in polarised proton-proton collisions, which is a parity-violating process. Complementary to this are measurements of single-hadron production in DIS, that however we do not consider because they require the simultaneous knowledge of FFs. Sensitivity to the gluon PDF is achieved thanks to the single-inclusive jet and di-jet production measurements in polarised proton-proton collisions, which account for the rest of our data set. Additional constraints on the gluon PDF may be provided by measurements of two other processes: single-hadron production in polarised proton-proton collisions, which we do not consider because of the need for the simultaneous knowledge of FFs; and open-charm production in DIS, which we do not consider because the available data sets were demonstrated to bring in a negligible amount of information [30].

The complete information on experimental uncertainties, including on their correlations, is taken into account whenever available from the HEPDATA repository [91] or from the corresponding publications. Specifically, full covariance matrices are provided only for the HERMES measurement of [69] and for the STAR jet measurements of [82–87]. Most notably, the latter include correlations between all the single-inclusive jet and di-jet bins, a fact that allows us to include all the measurements at the same time in the fit without incurring in double counting. Information on correlations is generally not provided by other experiments, except for the highlight of a multiplicative, fully correlated, uncertainty due to the beam polarisation. We use experimental uncertainties to construct the so-called experimental covariance matrix, see Eq. (8) in [92] for its definition. This covariance matrix will be used to present the fit quality in Sect. 4. We also construct the  $t_0$  covariance matrix, according to Eq. (9) in [92], whereby relative multiplicative uncertainties are multiplied by the corresponding theoretical predictions instead of experimental data. This prescription, which was designed to avoid D’Agostini bias [93], will be used for parameter optimisation.

## 2.2 Perturbative accuracy

The perturbative accuracy of the theoretical predictions corresponding to the measurements described in Sect. 2.1 depends on the perturbative accuracy of the partonic matrix elements and of the DGLAP splitting functions, which are both expanded as a series in the strong coupling. Concerning this perturbative accuracy, this work pursues two goals: first, to include corrections up to NNLO in both; and, second, to include MHOUs arising from the truncation of the expansion series to a finite accuracy.

The first goal is achieved by deploying a set of open-source computational tools specifically designed for PDF fitting. As already mentioned, these include: YADISM [44] for the computation of the polarised inclusive structure function  $g_1$ ; PINEAPPL [46, 47] (interfaced with the codes presented in [23, 88, 89] and used to compute the polarised proton-proton collision spin asymmetries) for the construction of PDF-independent fast interpolation grids; EKO [42, 43] for PDF evolution; and the PINELINE framework [41] to combine them all. Each of these pieces of software have been extended to handle the computation of the polarised observables at the desired accuracy. This amounted to the following. We implemented in YADISM the FONLL general-mass variable-flavour-number scheme up to NNLO [36, 37], which combines the massless computation [7] with the recent massive one [9] and its asymptotic limit [14]. We implemented in EKO the polarised splitting functions, including the known corrections up to NNLO [24–27] and their matching conditions [14] for heavy quarks. We have finally extended PINEAPPL and PINEKO to deal with polarised observables, including in the case in which unpolarised and polarised PDFs ought to be used simultaneously, such as in the computation of spin asymmetries. In all the computations, we use the same values of the physical parameters as in NNPDF4.0 [33].

The second goal is achieved following the methodology developed in [38–40]. Specifically, we supplement the experimental covariance matrix, constructed from knowledge of experimental uncertainties, with a MHOUs covariance matrix, constructed from renormalisation and factorisation scale variations

$$\text{cov}_{ij}^{(\text{tot})} = \text{cov}_{ij}^{(\text{exp})} + \text{cov}_{ij}^{(\text{mhou})}, \quad i, j = 1 \dots N_{\text{dat}}. \quad (2.1)$$

Renormalisation scale variations govern the scale dependence of matrix elements, while factorisation scale variations govern the scale dependence of DGLAP evolution equations. The former are correlated only across data points that belong to the same physical processes; the latter are correlated across all data points. To properly correlate renormalisation scale variations, we therefore define four process categories: neutral-current DIS (DIS NC), corresponding to measurements of  $g_1$ ; charged-current Drell-Yan (DY CC),



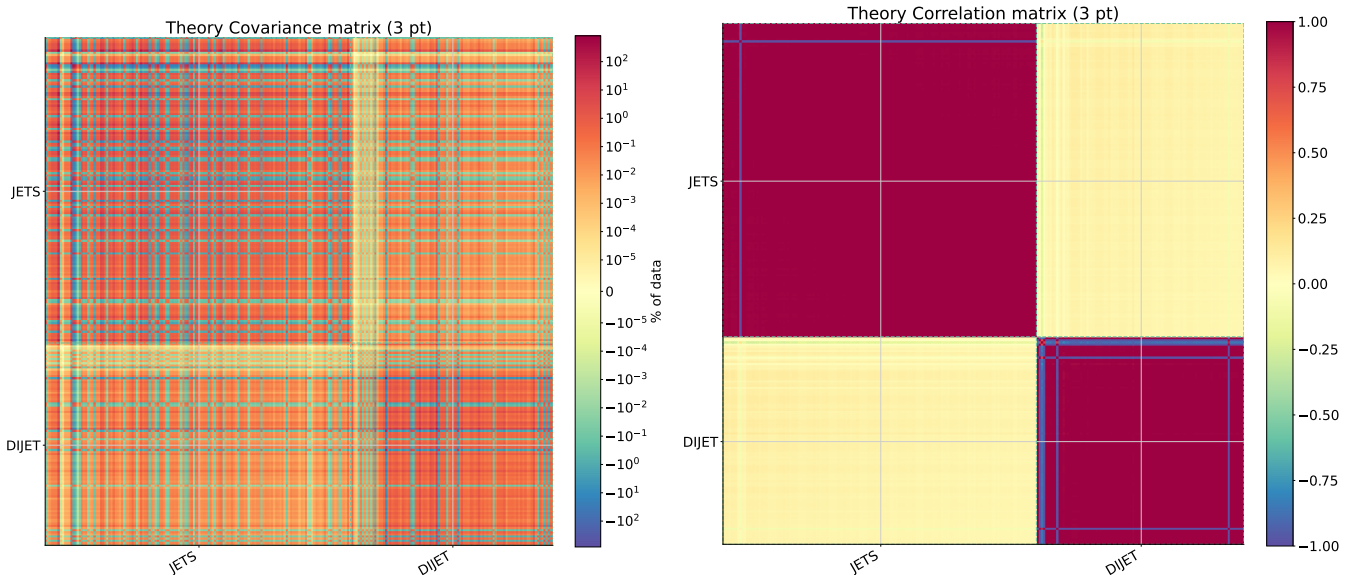


**Figure 2.2.** The JETS and DIJETS theory covariance (left) and correlation (right) matrices used to estimate unknown NNLO corrections to the corresponding matrix elements. The matrix is computed with renormalisation scale variations corresponding to prescription (i) and normalised for each row to the central value of the data point. Note the logarithmic (linear) scale used in the left (right) panel.

corresponding to measurements of  $A_L^{W^\pm}$ ; single-inclusive jet production (JETS), corresponding to measurements of  $A_{LL}^{1\text{-jet}}$ ; and di-jet production (DIJET), corresponding to measurements of  $A_{LL}^{2\text{-jet}}$ . We thus assume four independent renormalisation scales  $\mu_{r,i}$  and one common factorisation scale  $\mu_f$ . For the renormalisation  $\mu_r$  and factorisation  $\mu_f$  scales we define the normalised ratios  $\rho_{r,k} = \mu_{r,k}/Q$  and  $\rho_{f,k} = \mu_{f,k}/Q$ , respectively, where  $Q$  denotes the central scale of the process (*e.g.*  $Q = m_{jj}$  for di-jet production).

The computation of  $\text{cov}_{ij}^{(\text{mhou})}$  then follows the scheme B prescription detailed in [39]. Using an approach similar to that developed in [94], we can distinguish two different scale variation procedures, depending on which MHO component we want to estimate.

- (i) We adopt a 3-point renormalisation scale variation prescription to estimate missing NNLO corrections in the matrix elements of those processes for which they are unknown, that is, single-inclusive jet and di-jet production in polarised proton-proton collisions. We therefore vary the ratios  $\rho_{r,i}$  of the JETS and DIJET processes in the range  $\rho_{r,i} \in \{0.5, 1.0, 2.0\}$ . The resulting covariance matrix is shown in Fig. 2.2 (left), where each entry is expressed as a percentage of the experimental central value; there we also show the corresponding correlation matrix (right).
- (ii) We adopt a 7-point renormalisation and factorisation scale variation prescription to estimate the MHO for the complete data set. This prescription can be applied both at NLO and at NNLO. We therefore consider simultaneous variations of the factorisation and renormalisation scales in the range  $\rho_k = \{0.5, 1.0, 2.0\}$ , and discard the two outermost combinations, namely  $(\rho_{r,i}, \rho_f) = (0.5, 2.0)$  and  $(2.0, 0.5)$ . The resulting correlation matrix is displayed in Fig. 2.3, both at NLO (left) and at NNLO (right).

The two prescriptions are exclusive. Prescription (i) will be adopted only in the NNLO fits that we will call *without MHOUs* in Sect. 4. This nomenclature puts the emphasis on the fact that MHOUs are included only partially, and specifically only to account for unknown NNLO corrections. All the other fits called *without MHOUs*, either LO or NLO, will not use either prescription. Prescription (ii) will be adopted in all the fits, whether LO, NLO or NNLO, that we will call *with MHOUs* in Sect. 4. This nomenclature puts the emphasis on the fact that MHOUs, beyond the nominal accuracy of the fit, are included on all data points. Be that as it may, we have checked that MHOUs are generally smaller than experimental uncertainties, and that they are significantly more correlated. From Fig. 2.3 we can also appreciate how the NNLO MHO correlations are generally smaller than the NLO ones, indicating a consistent perturbative convergence of theoretical predictions.

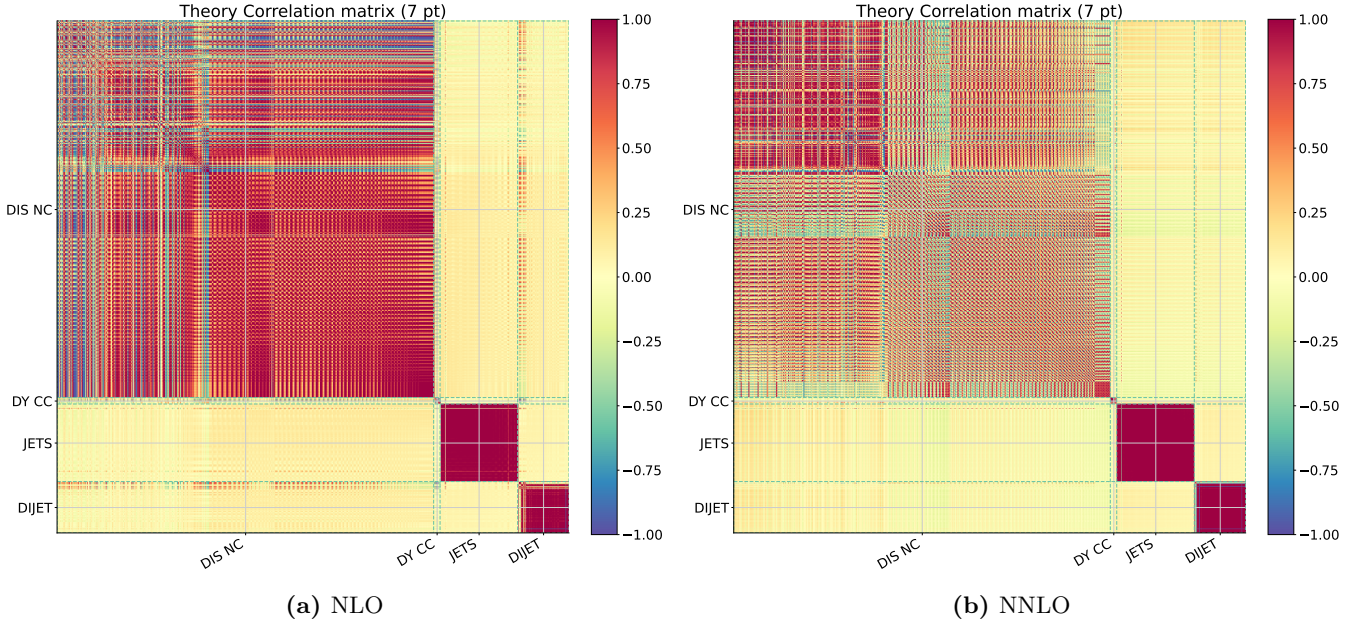


**Figure 2.3.** The MHO correlation matrix for all the data sets entering NNPDFPOL2.0, computed with the 7-point prescription (ii) at NLO (left) and NNLO (right).

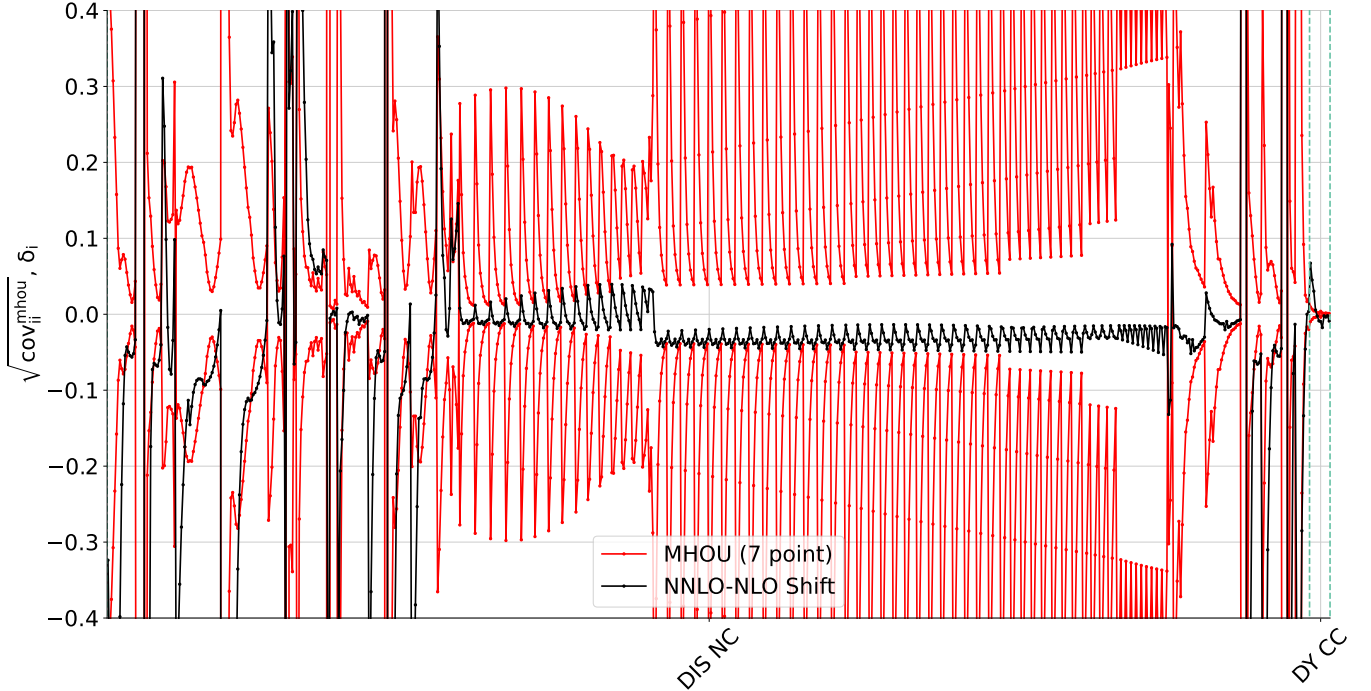


**Figure 2.4.** Comparison of the square root of the diagonal elements of the MHO covariance matrix  $\sqrt{\text{cov}_{ii}^{(\text{mhou})}}$  evaluated at NLO (red) with the NNLO-NLO shifts  $\delta_i$  (black) for the NC DIS and CC DY data points. Both quantities are normalised to the central value of the experimental data. The calculation of the MHO covariance matrix is obtained using the 7-point prescription in scheme B.

To verify whether the procedure is able to correctly estimate the magnitude of higher order corrections, we can compare the shift  $\delta_i$  between known NLO and NNLO predictions to the square root of the diagonal elements of the NLO MHO covariance matrix. This comparison is shown in Fig. 2.4 for the DIS NC and the DY CC data; the JETS and DIJET data are not shown because NNLO corrections are unknown. We observe that MHOUs and the shift display a very similar pattern, and, more importantly, that for most of the data points the NLO MHO overestimates the NLO-NNLO shift. We should however consider that the somewhat conservative estimate of MHOUs will be compensated by correlations once the corresponding covariance matrix is included in a PDF fit, as we will see in Sect. 4.

### 3 Fitting methodology

In this section, we present the methodology deployed to determine NNPDFPOL2.0 based on parametric regression with machine learning. This methodology closely follows the one used in [33, 56] for the determination of the NNPDF4.0 set of unpolarised PDFs. We review in turn which aspects of the PDF parametrisation, optimisation, and hyperoptimisation are upgraded and adapted from the unpolarised to the polarised case.

#### 3.1 Parametrisation

Parton distribution parametrisation entails two choices: first, a choice of parametrisation basis, that is, the set of linearly independent distributions that are parametrised; second, a choice of parametrisation form, that is, the function that maps the PDF parameters into the elements of the basis.

Concerning the parametrisation basis, we choose the set

$$\Delta f(x, Q_0^2) = \{\Delta g, \Delta \Sigma, \Delta T_3, \Delta T_8, \Delta V, \Delta V_3\}(x, Q_0^2), \quad (3.1)$$

made of the gluon PDF  $\Delta g$  and of five independent quark flavour PDF combinations: the singlet  $\Delta \Sigma$ , the non-singlet sea triplet  $\Delta T_3$  and octet  $\Delta T_8$ , the total valence  $\Delta V$ , and the non-singlet valence  $\Delta V_3$ . These PDF combinations are defined as

$$\begin{aligned} \Delta \Sigma(x, Q_0^2) &= \Delta u^+(x, Q_0^2) + \Delta d^+(x, Q_0^2) + \Delta s^+(x, Q_0^2), \\ \Delta T_3(x, Q_0^2) &= \Delta u^+(x, Q_0^2) - \Delta d^+(x, Q_0^2), \\ \Delta T_8(x, Q_0^2) &= \Delta u^+(x, Q_0^2) + \Delta d^+(x, Q_0^2) - 2\Delta s^+(x, Q_0^2), \\ \Delta V(x, Q_0^2) &= \Delta u^-(x, Q_0^2) + \Delta d^-(x, Q_0^2) + \Delta s^-(x, Q_0^2), \\ \Delta V_3(x, Q_0^2) &= \Delta u^-(x, Q_0^2) - \Delta d^-(x, Q_0^2), \end{aligned} \quad (3.2)$$

where  $\Delta q^\pm = \Delta q \pm \Delta \bar{q}$ , with  $q = u, d, s$ . The basis defined in Eq. (3.2) corresponds to the eigenbasis of the DGLAP evolution equations. The parametrisation scale is taken to be  $Q_0^2 = 1.0 \text{ GeV}^2$ ; PDFs are then evolved to the scale of the physical processes by means of DGLAP equations, see Sect. 2.

Because the available experimental data is essentially insensitive to a possible asymmetry between  $\Delta s$  and  $\Delta \bar{s}$ , we assume  $\Delta s(x, Q_0^2) = \Delta \bar{s}(x, Q_0^2)$ . At the parametrisation scale, the non-singlet distribution  $\Delta V_8(x, Q_0^2) = \Delta u^-(x, Q_0^2) + \Delta d^-(x, Q_0^2) - 2\Delta s^-(x, Q_0^2)$  is therefore equal to the total valence distribution,  $\Delta V_8(x, Q_0^2) = \Delta V(x, Q_0^2)$ . Small differences between  $\Delta s$  and  $\Delta \bar{s}$  occur for  $Q^2 > Q_0^2$  at NNLO and beyond, because higher-order QCD corrections induce a different evolution for the two distributions [95]. We assume that charm is generated from gluon splitting through parton evolution, therefore we set to zero, and do not parametrise, a possible polarised intrinsic charm component at the parametrisation scale  $Q_0^2$ .

Concerning the parametrisation form, we choose a feed-forward neural network with six output nodes, each of which corresponds to an element of the fitting basis defined in Eq. (3.1). The neural network has two input nodes that correspond to values of  $x$  and  $\ln x$ . The neural network architecture and activation functions are determined according to the hyperparameter optimisation procedure delineated in Sect. 3.3. The output of the neural network is then related to the polarised PDFs as

$$x\Delta f(x, Q_0^2, \boldsymbol{\theta}) = A_{\Delta f} x^{1-\alpha_{\Delta f}} (1-x)^{\beta_{\Delta f}} \text{NN}_{\Delta f}(x, \boldsymbol{\theta}), \quad (3.3)$$

where  $\Delta f$  denotes each element of the chosen basis,  $A_{\Delta f}$  is a normalisation factor,  $\alpha_{\Delta f}$  and  $\beta_{\Delta f}$  are preprocessing exponents, and  $\text{NN}_{\Delta f}(x, \boldsymbol{\theta})$  is the output of the neural network, which depends on weights and biases, collectively denoted as  $\boldsymbol{\theta}$ .

The normalisation factor  $A_{\Delta f}$  is equal to one for all PDFs but the non-singlet triplet and octet PDF combinations,  $\Delta T_3$  and  $\Delta T_8$ , for which we define

$$A_{\Delta T_3} = a_3 \left[ \int_{x_{\min}}^1 dx \Delta T_3(x, Q_0^2) \right]^{-1} \quad \text{and} \quad A_{\Delta T_8} = a_8 \left[ \int_{x_{\min}}^1 dx \Delta T_8(x, Q_0^2) \right]^{-1}. \quad (3.4)$$

Here  $a_3$  and  $a_8$  are the (scale-independent) baryon octet decay constants, whose experimental values are taken from the PDG review [96]

$$a_3 = 1.2756 \pm 0.0013 \quad \text{and} \quad a_8 = 0.585 \pm 0.025. \quad (3.5)$$

| $\Delta f$          | $\Delta\Sigma$ | $\Delta g$     | $\Delta T_3$   | $\Delta T_8$   | $\Delta V_3$   | $\Delta V$     |
|---------------------|----------------|----------------|----------------|----------------|----------------|----------------|
| $\alpha_{\Delta f}$ | [+1.09, +1.12] | [+0.82, +1.84] | [-0.44, +0.93] | [+0.59, +0.85] | [+0.47, +0.96] | [+0.08, +0.95] |
| $\beta_{\Delta f}$  | [+1.46, +3.00] | [+2.59, +5.70] | [+1.77, +3.33] | [+1.53, +3.44] | [+1.57, +3.56] | [+1.51, +3.45] |

**Table 3.1.** The initial ranges from which the small- and large- $x$  preprocessing exponents are sampled for each PDF replica. The ranges are the same for the LO, NLO, and NNLO fits, without and with MHOU.

The integrals in Eq. (3.4) are computed each time the parameters  $\theta$  change, taking  $x_{\min} = 10^{-4}$ . For each replica, the values of  $a_3$  and  $a_8$  are random numbers sampled from a Gaussian distribution with mean value and standard deviation equal to the corresponding experimental central value and uncertainty, Eq. (3.5). Enforcing Eq. (3.4) therefore corresponds to requiring that SU(2) and SU(3) flavour symmetries are exact up to the experimental uncertainties quoted in Eq. (3.5). A sizeable breaking of SU(3) is advocated in the literature [97], which may result in an increase of the uncertainty on  $a_8$  up to 30%. We take as default this more conservative estimate, and set  $a_8 = 0.585 \pm 0.176$ .

Finally, the preprocessing exponents  $\alpha_{\Delta f}$  and  $\beta_{\Delta f}$ , which are needed to speed up the neural network training, are determined by means of an iterative procedure, firstly introduced in [57]. Specifically, their values are initially random numbers sampled from a flat distribution in the ranges summarised in Table 3.1. These ranges are re-determined from PDFs after these are fitted to the data; PDFs are then refitted using values of the effective exponents that are sampled within the newly determined ranges. The procedure is repeated until PDFs do not change, a result that is typically reached in a couple of iterations. We use the ranges of Table 3.1 for all our LO, NLO, and NNLO fits, without and with MHOU.

### 3.2 Parameter optimisation

Optimisation of the neural network parameters  $\theta$  requires a choice of loss function and of optimisation algorithm, including a stopping criterion. We discuss each of these two choices in turn.

Concerning the loss function, we make considerations that are peculiar to the determination of polarised PDFs. For each Monte Carlo PDF replica  $k$ , we define the loss function  $L^{(k)}(\theta)$  as the sum of three contributions:

$$L^{(k)}(\theta) \equiv \chi_{t_0}^{2(k)}(\theta) + \Lambda_{\text{int}} R_{\text{int}}^{(k)}(\theta) + \Lambda_{\text{pos}} R_{\text{pos}}^{(k)}(\theta). \quad (3.6)$$

The first term in Eq. (3.6) is the usual Gaussian likelihood evaluated with the  $t_0$  prescription

$$\chi_{t_0}^{2(k)}(\theta) = \frac{1}{N_{\text{dat}}} \sum_{i,j=1}^{N_{\text{dat}}} \left[ T_i \left( \Delta f^{(k)}(x, Q_0^2, \theta) \right) - D_i^{(k)} \right] (\text{cov}_{t_0})_{ij}^{-1} \left[ T_j \left( \Delta f^{(k)}(x, Q_0^2, \theta) \right) - D_j^{(k)} \right], \quad (3.7)$$

where  $i, j$  are indices that run on the number of data points  $N_{\text{dat}}$ ,  $\text{cov}_{ij,t_0}$  is the  $t_0$  covariance matrix,  $D_i^{(k)}$  are the  $k$ -th experimental pseudodata replicas, and  $T_i \left( \Delta f^{(k)}(x, Q_0^2, \theta) \right)$  are the corresponding theoretical predictions. The covariance matrix is computed as explained in Sect. 2. Specifically, the  $t_0$  prescription [93] is used to determine the contribution due to experimental uncertainties in Eq. (2.1), whereas point prescriptions are used to determine the MHOU contribution, when these are taken into account.

Theoretical predictions are matched to experimental data, which consists of measurements of asymmetries, see Sect. 2.1. As such, they are given by the ratio between cross sections that depend on polarised PDFs and cross sections that depend on unpolarised PDFs, where the latter are not fitted to the data:

$$T_i \left( \Delta f(x, Q_0^2, \theta) \right) = \frac{T_i^{(\text{pol})} \left( \Delta f(x, Q_0^2, \theta) \right)}{T_i^{(\text{ump})} \left( f(x, Q_0^2) \right)}. \quad (3.8)$$

Therefore, parameter optimisation enters theoretical predictions only through the numerator of Eq. (3.8), which is evaluated by convolving the parametrised PDFs with fast-kernel (FK) interpolating tables that are pre-computed in the PINEAPPL format. The FK tables are in turn a convolution of partonic matrix elements and evolution kernel operators (EKOs), that evolve PDFs from the parametrisation scale  $Q_0^2$  to the scale  $Q^2$  of the physical process.

The numerical implementation of these theory predictions proceeds as follows. Given a grid of  $x$  values  $\{x\}_{n=1}^{N_{\text{grid}}}$ , a theoretical prediction for  $T^{(\text{pol})}$  is obtained as an interpolation from grid values

$$T^{(\text{pol})}(\Delta f(x, Q_0^2, \boldsymbol{\theta})) = \sum_a \sum_n \Delta f_a(x_n, Q_0^2, \boldsymbol{\theta}) \Delta \text{FK}_a(x_n, Q^2 \leftarrow Q_0^2), \quad (3.9)$$

$$T^{(\text{pol})}(\Delta f(x, Q_0^2, \boldsymbol{\theta})) = \sum_{a,b} \sum_{m,n} \Delta \mathcal{L}_{ab}^{\text{L}}(x_m, x_n, Q_0^2, \boldsymbol{\theta}) \Delta \text{FK}_{ab}^{\text{L}}(x_m, x_n, Q^2 \leftarrow Q_0^2), \quad (3.10)$$

$$T^{(\text{pol})}(\Delta f(x, Q_0^2, \boldsymbol{\theta})) = \sum_{a,b} \sum_{m,n} \Delta \mathcal{L}_{ab}^{\text{LL}}(x_m, x_n, Q_0^2, \boldsymbol{\theta}) \Delta \text{FK}_{ab}^{\text{LL}}(x_m, x_n, Q^2 \leftarrow Q_0^2), \quad (3.11)$$

for processes with one, Eq. (3.9), or two, Eqs. (3.10)-(3.11), partons in the initial state. The indexes  $a$  and  $b$  run over the active partons, whereas the indexes  $m$  and  $n$  run over the  $N_{\text{grid}}$  values of the  $x$  interpolating grid. The partonic luminosities  $\Delta \mathcal{L}_{ab}^{\text{L}}$  in Eq. (3.10) and  $\Delta \mathcal{L}_{ab}^{\text{LL}}$  in Eq. (3.11) are the product of two PDFs, in particular, depending on the kind of theoretical prediction, of an unpolarised and a polarised PDF or of two polarised PDFs:

$$\Delta \mathcal{L}_{ab}^{\text{L}}(x_m, x_n, Q_0^2, \boldsymbol{\theta}) = f_a(x_m, Q_0^2) \Delta f_b(x_n, Q_0^2, \boldsymbol{\theta}), \quad (3.12)$$

$$\Delta \mathcal{L}_{ab}^{\text{LL}}(x_m, x_n, Q_0^2, \boldsymbol{\theta}) = \Delta f_a(x_m, Q_0^2, \boldsymbol{\theta}) \Delta f_b(x_n, Q_0^2, \boldsymbol{\theta}). \quad (3.13)$$

The FK tables in Eqs. (3.9)-(3.11) are

$$\Delta \text{FK}_a(x_n, Q^2 \leftarrow Q_0^2) = \sum_{c,j,k,\ell} \alpha_s^{p+k} \Delta \text{EKO}_{a,n}^{c,j,\ell} \Delta \sigma_c^{(k)}(x_\ell, \mu_j^2), \quad (3.14)$$

$$\Delta \text{FK}_{ab}^{\text{L}}(x_m, x_n, Q^2 \leftarrow Q_0^2) = \sum_{c,d,j,k,\ell,o} \alpha_s^{p+k} \Delta \text{EKO}_{a,m}^{c,j,\ell} \text{EKO}_{b,n}^{d,j,o} \Delta \sigma_{cd}^{(k),\text{L}}(x_\ell, x_o, \mu_j^2), \quad (3.15)$$

$$\Delta \text{FK}_{ab}^{\text{LL}}(x_m, x_n, Q^2 \leftarrow Q_0^2) = \sum_{c,d,j,k,\ell,o} \alpha_s^{p+k} \Delta \text{EKO}_{a,m}^{c,j,\ell} \Delta \text{EKO}_{b,n}^{d,j,o} \Delta \sigma_{cd}^{(k),\text{LL}}(x_\ell, x_o, \mu_j^2), \quad (3.16)$$

where the indexes  $a, b, c$ , and  $d$  denote the active partons, the indexes  $m, n, \ell$ , and  $o$  denote points in the  $x$  interpolation grids, the index  $p$  denotes the leading power of the strong coupling for a given process, the index  $k$  denotes the perturbative order, and the index  $j$  labels the renormalisation and factorisation scale variations. Depending on the process, a single polarised EKO ( $\Delta \text{EKO}_{a,n}^{c,j,\ell}$ ) is required, a polarised and an unpolarised EKOs are required ( $\Delta \text{EKO}_{a,m}^{c,j,\ell} \text{EKO}_{b,n}^{d,j,o}$ ), or two polarised EKOs are required ( $\Delta \text{EKO}_{a,m}^{c,j,\ell} \Delta \text{EKO}_{b,n}^{d,j,o}$ ).

Note that, in Eq. (3.8) and in Eq. (3.12), the unpolarised PDF does not depend on the parameters  $\boldsymbol{\theta}$ , because this is not determined from the data in the optimisation process. It is instead kept fixed to an external PDF set, which is chosen to be NNPDF4.0. Specifically, we use PDF sets determined assuming perturbative charm, at a perturbative order consistent with that of the accuracy of the determination of the polarised PDF. At LO, we therefore use NNPDF40\_lo\_pch\_as\_01180, at NLO NNPDF40\_nlo\_pch\_as\_01180, and at NNLO NNPDF40\_nnlo\_pch\_as\_01180. These PDF sets were determined from an independent data set, therefore we expect little interplay between the unpolarised and polarised PDFs, also in light of the fact that the former are comparatively better constrained. The unpolarised and polarised PDFs are determined with the same values of the physical parameters and with the same methodology. Finally, the denominator in Eq. (3.8) is computed using FK tables as the numerator. The only difference being that the polarised PDF,  $\Delta f(x, Q_0^2, \boldsymbol{\theta})$ , in Eqs. (3.9), (3.12), and (3.13), and the polarised EKOs,  $\Delta \text{EKO}$ , and the polarised cross sections,  $\Delta \sigma$ , in Eqs. (3.14)-(3.16) are replaced with their unpolarised counterparts.

The second term in Eq. (3.6),  $\Lambda_{\text{int}} R_{\text{int}}(\boldsymbol{\theta})$ , is a regularisation term that enforces the lowest moments of polarised PDFs to be finite. This requirement follows from the assumption that the nucleon matrix element of the axial current be finite for each parton. Therefore, the small- $x$  behaviour of polarised PDFs must obey

$$\lim_{x \rightarrow 0} x \Delta f(x, Q^2) = 0 \quad \text{for } \Delta f = \Delta g, \Delta \Sigma, \Delta T_3, \Delta T_8, \quad (3.17)$$

$$\lim_{x \rightarrow 0} x^2 \Delta f(x, Q^2) = 0 \quad \text{for } \Delta f = \Delta V_3, \Delta V_8. \quad (3.18)$$

The first of these two conditions is fulfilled by construction for the polarised quark triplet and octet PDF combinations, given the choice of normalisation made in their parametrisation, see Eq. (3.4). The regulari-

sation term is defined as

$$\Lambda_{\text{int}} R_{\text{int}}(\boldsymbol{\theta}) = \Lambda_{\text{int}} \sum_f [x \Delta f(x_{\text{int}}, Q_{\text{int}}^2, \boldsymbol{\theta})]^2 \quad \text{for } \Delta f = \Delta g, \Delta \Sigma, \quad (3.19)$$

$$\Lambda_{\text{int}} R_{\text{int}}(\boldsymbol{\theta}) = \Lambda_{\text{int}} \sum_f [x^2 \Delta f(x_{\text{int}}, Q_{\text{int}}^2, \boldsymbol{\theta})]^2 \quad \text{for } \Delta f = \Delta V, \Delta V_3, \quad (3.20)$$

where  $Q_{\text{int}}^2 = 1 \text{ GeV}^2$  and  $x_{\text{int}} = 10^{-5}$ . The Lagrange multiplier  $\Lambda_{\text{int}}$  grows exponentially during the fit and reaches the maximum value  $\Lambda_{\text{int}} = 100$  at maximum training length.

The third term in Eq. (3.6),  $\Lambda_{\text{pos}} R_{\text{pos}}^{(k)}(\boldsymbol{\theta})$ , is a regularisation term that enforces PDFs to lead to positive cross sections. At LO, this implies that polarised PDFs are bound by their unpolarised counterparts for each parton  $f$ , for each  $x$ , and for each  $Q^2$  [98]

$$|\Delta f(x, Q^2)| \leq f(x, Q^2). \quad (3.21)$$

Beyond LO, bounds on polarised PDFs can be derived using physical cross sections. In the case of the gluon PDF, for instance, by studying Higgs boson production in polarised proton-proton collisions [99]. Be that as it may, however, NLO corrections distort the LO positivity condition, Eq. (3.21), only mildly at large  $x$ , where it can actually affect polarised PDFs [98, 100]. We therefore conclude that Eq. (3.21) can be effectively used to enforce positivity, without introducing a bias in our determination. This conclusion is supported by the results that we get if the positivity constraint, Eq. (3.21), is lifted from the fit, see Sect. 4.3. The regularisation term is defined as

$$\Lambda_{\text{pos}} R_{\text{pos}}^{(k)}(\boldsymbol{\theta}) = \Lambda_{\text{pos}} \sum_f \sum_{i=1}^n \text{ReLU}(-\mathcal{C}_f(x_{\text{pos}}^i, Q_{\text{pos}}^2, \boldsymbol{\theta})), \quad \text{ReLU}(t) = \begin{cases} t & \text{if } t > 0 \\ 0 & \text{if } t \leq 0 \end{cases}, \quad (3.22)$$

where the function

$$\mathcal{C}_f(x_{\text{pos}}^i, Q_{\text{pos}}^2, \boldsymbol{\theta}) = f(x_{\text{pos}}^i, Q_{\text{pos}}^2) - |\Delta f(x_{\text{pos}}^i, Q_{\text{pos}}^2, \boldsymbol{\theta})| + \sigma_f(x_{\text{pos}}^i, Q_{\text{pos}}^2), \quad (3.23)$$

encodes the positivity condition of Eq. (3.21), including the uncertainty on the unpolarised PDF. In Eqs. (3.22)-(3.23),  $f$  denotes the parton, and  $i$  denotes the point at which the function  $\mathcal{C}_f$  is evaluated. In particular,  $n = 20$  points are sampled in the range  $[5 \cdot 10^{-7}, 9 \cdot 10^{-1}]$ , half of which are logarithmically spaced below  $10^{-1}$  and half of which are linearly spaced above. The unpolarised PDF  $f$  and its one-sigma uncertainty  $\sigma_f$  are taken from NNPDF4.0, specifically from the same PDF set that enters the computation of theoretical predictions, see above. Finally,  $Q_{\text{pos}}^2 = 5 \text{ GeV}^2$  and the Lagrange multiplier  $\Lambda_{\text{pos}}$  grows exponentially during the fit, reaching the maximum value  $\Lambda_{\text{int}} = 10^{10}$  at maximum training length.

Optimisation of the parameters  $\boldsymbol{\theta}$  is achieved through stochastic gradient descent applied to the loss function, Eq. (3.6), as in NNPDF4.0, see in particular Sect. 3.2 of [33]. The specific optimisation algorithm is selected from those that are available in the KERAS library [101, 102] through hyperparameter optimisation, as discussed in Sect. 3.3. As in NNPDF4.0, cross-validation is used to avoid overfitting. To this purpose, for each pseudodata replica, the data points are split into a training and a validation sets, in a proportion of 60% and 40%. The loss function, Eq. (3.6), is then optimised on the training set and monitored on the validation set. The stopping criterion is as in NNPDF4.0, specifically, the fit stops when the validation loss does not improve for a number of epochs given by the product of the maximum number of epochs and the stopping patience. Both the maximum number of epochs and the stopping patience are hyperparameters whose values are obtained as explained in Sect. 3.3. Post-fit checks are enforced to exclude parameter configurations that violate the positivity constraint, or, as in NNPDF4.0, that have values of the  $\chi^2$  or the arc-length that are outside the four-sigma interval of their distribution.

### 3.3 Hyperparameter optimisation

Hyperparameter optimisation consists in an automated scan of the space of models, that are appraised according to a properly defined figure of merit, see, *e.g.*, Sect. 3.3 in [33]. To ensure that the optimal model does not lead to overfitted PDFs, a  $k$ -folding partition of the data set is used, which verifies the effectiveness of any given model on sets of data excluded in turn from the fit. A methodology to perform hyperparameter

| Fold 1                                   | Fold 2                                   | Fold 3                                   | Fold 4                                   |
|--|--|--|--|
| COMPASS $g_1^p$                          | COMPASS $g_1^d$                          | E143 $g_1^p$                             | E143 $g_1^d$                             |
| E142 $g_1^n$                             | E155 $g_1^p/F_1^p$                       | HERMES $g_1^n$                           | E154 $g_1^n$                             |
| E155 $g_1^n/F_1^n$                       | EMC $g_1^p$                              | SMC $g_1^d$                              | SMC $g_1^p$                              |
| HERMES $g_1^d$                           | HERMES $g_1^p$                           | SMC low- $x$ $g_1^p/F_1^p$               | SMC low- $x$ $g_1^d/F_1^d$               |
| STAR $A_L^{W^-}$                         | STAR $A_L^{W^+}$                         | STAR $A_L^{W^-}$                         | STAR $A_L^{W^+}$                         |
| STAR $A_{LL}^{1-\text{jet}}$ (2005)      | STAR $A_{LL}^{1-\text{jet}}$ (2006)      | STAR $A_{LL}^{1-\text{jet}}$ [CC] (2009) | STAR $A_{LL}^{1-\text{jet}}$ [CF] (2009) |
| STAR $A_{LL}^{1-\text{jet}}$ (2012)      | STAR $A_{LL}^{1-\text{jet}}$ (2013)      | STAR $A_{LL}^{1-\text{jet}}$ [CC] (2015) | STAR $A_{LL}^{1-\text{jet}}$ [CF] (2015) |
| STAR $A_{LL}^{2-\text{jet}}$ [A] (2009)  | STAR $A_{LL}^{2-\text{jet}}$ [B] (2009)  | STAR $A_{LL}^{2-\text{jet}}$ [C] (2009)  | PHENIX $A_{LL}^{1-\text{jet}}$ 200 GeV   |
| STAR $A_{LL}^{2-\text{jet}}$ [A] (2012)  | STAR $A_{LL}^{2-\text{jet}}$ [B] (2012)  | STAR $A_{LL}^{2-\text{jet}}$ [C] (2012)  | STAR $A_{LL}^{2-\text{jet}}$ [D] (2012)  |
| STAR $A_{LL}^{2-\text{jet}}$ [D] (2013)  | STAR $A_{LL}^{2-\text{jet}}$ [C] (2013)  | STAR $A_{LL}^{2-\text{jet}}$ [B] (2013)  | STAR $A_{LL}^{2-\text{jet}}$ [A] (2013)  |
| STAR $A_{LL}^{2-\text{jet}}$ [SS] (2019) | STAR $A_{LL}^{2-\text{jet}}$ [OS] (2015) | STAR $A_{LL}^{2-\text{jet}}$ [SS] (2015) | STAR $A_{LL}^{2-\text{jet}}$ [OS] (2009) |

**Table 3.2.** The partition of the NNPDFPOL2.0 data set into the four folds used in the  $k$ -folding hyperoptimisation procedure. The letters in brackets denote different topologies of the single-inclusive jet and di-jet measurements. The JLab measurements, not listed explicitly in the table, are included in each of the four folds.

optimisation therefore requires three choices: first, a selection of the hyperparameters to optimise; second, a partition of the data sets into folds; and third, a definition of the figure of merit to optimise.

Concerning the hyperparameters to optimise, similarly to what was done in NNPDF4.0, we scan the neural network architecture (specifically the number of layers, the number of nodes, and the form of the activation function), the optimiser, the value of the clipnorm, and the learning rate. We keep fixed the maximum number of training epochs, the stopping patience, and the initial values of the Lagrange multipliers in the integrability and positivity regularisation terms,  $\Lambda_{\text{int}}$  and  $\Lambda_{\text{pos}}$ , in the loss function, Eq. (3.6).

Concerning the  $k$ -folding partition, as in NNPDF4.0, we construct four different folds, by selecting individual measurements in such a way that each fold is representative of the global data set for both the kinematic coverage and process types. Our selection is reported in Table 3.2. The JLab data sets are included in all four folds, hence they are not explicitly listed in Table 3.2. This choice is motivated by the fact that they provide little constraints on polarised PDFs, despite being composed of a large number of data points.

Concerning the figure of merit to optimise, we make a choice that differs from NNPDF4.0. Specifically, instead of making our model selection based on fits to the central data, we now hyperoptimise at the level of the PDF distributions resulting from fits to a Monte Carlo PDF replica ensemble. This was not possible before due to several limitations, the main one being the inability to perform simultaneous fits of multiple replicas at once. Thanks to various technical improvements [49], it is now possible to perform simultaneous multiple replicas fits using graphics processing units (GPUs). Such improvements also allow us to distribute the hyperoptimisation scans across multiple GPUs, allowing for an asynchronous search of the parameter space. This development implies that the larger the number of GPUs utilised, the faster the scan of the hyperparameter space.

The algorithm starts each trial with a selected set of hyperparameter configurations from which  $n_{\text{folds}}$  folds are constructed. For each subset of folds, the  $p$ -th fold is left-out and the remaining folds are combined into a data set from which the neural network is optimised according to the procedure described in Sect. 3.2 by fitting simultaneously  $N_{\text{rep}}$  replicas. The figure of merit is then defined as the  $\chi_{\text{PDF}}^2$  of the non-fitted folds averaged over the folds,

$$L_{\text{hopt}}^{(\chi_{\text{PDF}}^2)}(\hat{\theta}) = \frac{1}{n_{\text{folds}}} \sum_{p=1}^{n_{\text{folds}}} \min_{\theta \in \Theta}^* \left( \left\langle \chi_{\text{PDF},p}^2(\theta, \hat{\theta}) \right\rangle_{\text{rep}} \right), \quad (3.24)$$

where we distinguish between the model parameters  $\theta$  (the neural network weights and biases) and hyperparameters  $\hat{\theta}$ . The  $\chi_p^{2(k)}$  of the  $p$ -th fold now includes contributions from the PDF uncertainties, added in quadrature to the experimental covariance matrix

$$\chi_{\text{PDF},p}^{2(k)}(\theta) = \frac{1}{n_p} \sum_{i,j \in p} \left( D_i^{(0)} - T_i^{(k)}(\theta) \right) \left( \text{cov}^{(\text{exp})} + \text{cov}^{(\text{PDF})} \right)_{ij}^{-1} \left( D_j^{(0)} - T_j^{(k)}(\theta) \right), \quad (3.25)$$

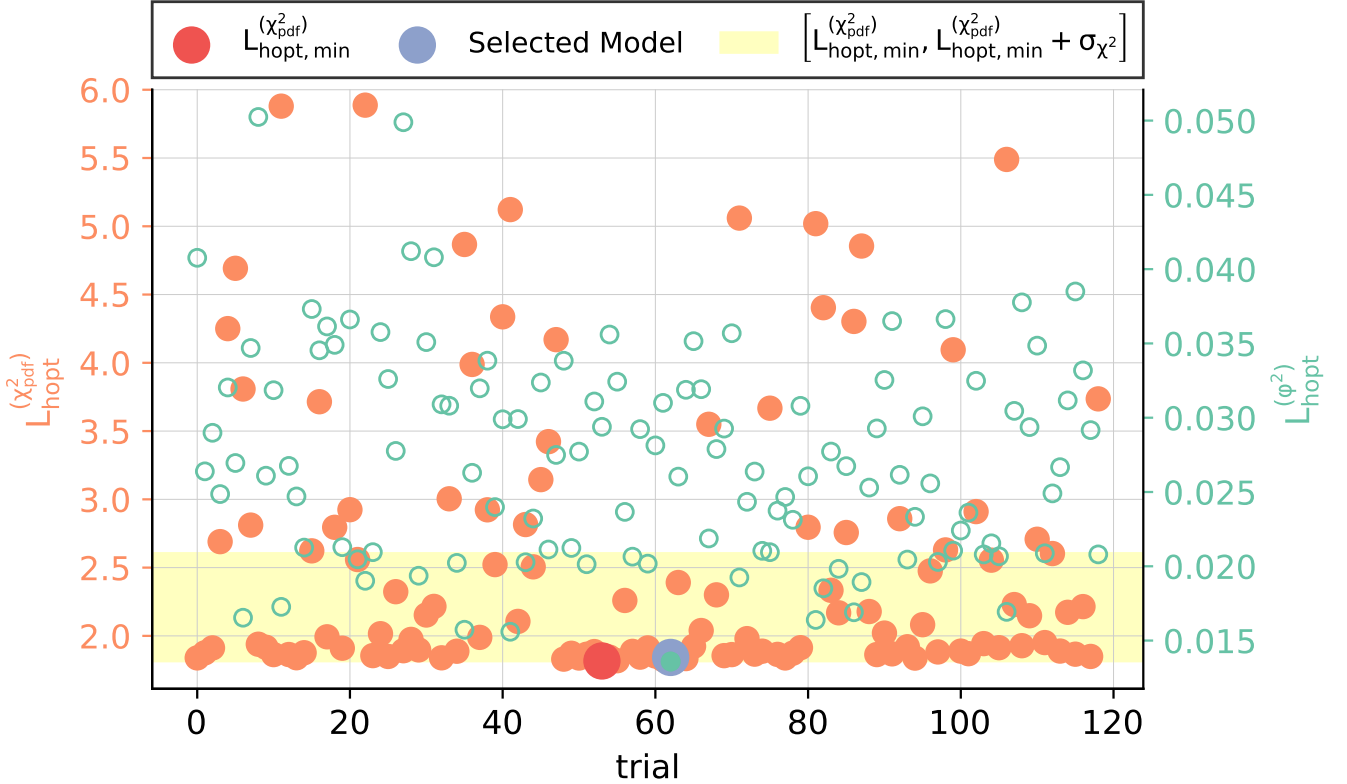


**Figure 3.1.** The values of the two hyperoptimisation metrics considered in this work, Eq. (3.24) and Eq. (3.26), displayed in the left and right  $y$ -axes respectively, for the  $n_{\text{trials}}$  considered configurations of model hyperparameters. The band indicates the selection range defined in Eq. (3.28).

following the theory covariance matrix formalism presented in [40, 103], and where  $n_p$  indicates the number of data points in the  $p$ -th fold.

For all the  $n_{\text{trials}}$  hyperparameter configurations explored in the parameter space, one obtains  $n_{\text{trials}}$  losses computed with Eq. (3.24). Additionally, for each point in the hyperparameter space, we also evaluate the standard deviation over the replica sample in units of the data uncertainty on the left-out folds. A suitable hyperoptimisation loss that displays such a property can be defined as [49]

$$L_{\text{hopt}}^{(\varphi^2)}(\hat{\theta}) \equiv \left( \frac{1}{n_{\text{folds}}} \sum_{p=1}^{n_{\text{folds}}} \varphi_{\chi_p^2}^2(\hat{\theta}) \right)^{-1}, \quad (3.26)$$

where the metric that probes the second moment of the PDF distribution is given by

$$\varphi_{\chi_p^2}^2 = \langle \chi_p^2 [T(\Delta f_{\text{fit}}), D] \rangle_{\text{rep}} - \chi_p^2 [\langle T(\Delta f_{\text{fit}}) \rangle_{\text{rep}}, D]. \quad (3.27)$$

This equation measures the PDF uncertainty on the scale of the data uncertainties, therefore given a successful fit to the data excluding the  $k$ -th fold, the preferred extrapolation to the non-fitted  $k$ -th fold is the one with the largest uncertainties, *i.e.* with small values of Eq. (3.26).

Given a set of successful models, for which  $L_{\text{hopt}}^{(\chi_{\text{pdf}}^2)} \leq L_{\text{hopt,threshold}}^{(\chi_{\text{pdf}}^2)}$ , we then select the best one as follows. We evaluate the standard deviation  $\sigma_{\chi^2}$  from the spread of  $\chi_{\text{PDF},k}^{2(k)}$ , Eq. (3.25), among the  $N_{\text{rep}}$  replicas of the selected fit given by  $\hat{\theta}^* \equiv L_{\text{hopt,min}}^{(\chi_{\text{pdf}}^2)}$ . We then use this value to define a selection range

$$\mathcal{R} : \left[ \hat{\theta}^*, \hat{\theta}^* + \sigma_{\chi^2} \right], \quad \text{with} \quad \hat{\theta}^* = \arg \min_{\hat{\theta} \in \hat{\Theta}} \left( L_{\text{hopt}}^{(\chi_{\text{pdf}}^2)}(\hat{\theta}) \right). \quad (3.28)$$

The optimal set of hyperparameters is then selected to be those that yield the lowest value of Eq. (3.26) within the range  $\mathcal{R}$ .



| Parameter                        | Sampled range        |                      | Optimal model                 |
|----------------------------------|----------------------|----------------------|-------------------------------|
|                                  | min.                 | max.                 |                               |
| NN architecture                  | $n_1, n_2, n_3 = 10$ | $n_1, n_2, n_3 = 40$ | $n_1 = 29, n_2 = 12, n_3 = 6$ |
| Number of layers                 | 2                    | 3                    | 3                             |
| NN initializer                   | GLOROT_NORMAL        | GLOROT_UNIFORM       | GLOROT_UNIFORM                |
| Activation functions             | TANH                 | SIGMOID              | TANH                          |
| Optimizer                        | NADAM                | ADAM                 | NADAM                         |
| Clipnorm                         | $10^{-7}$            | $10^{-4}$            | $2.95 \times 10^{-5}$         |
| Learning rate                    | $10^{-4}$            | $10^{-2}$            | $1.40 \times 10^{-3}$         |
| Maximum # training epochs        |                      | 17000                | 17000                         |
| Stopping patience                |                      | 0.1                  | 0.1                           |
| Initial positivity multiplier    |                      | 185                  | 185                           |
| Initial integrability multiplier |                      | 10                   | 10                            |

**Table 3.3.** The hyperparameters considered in this study and the values selected for the optimal model. Hyperparameters that are kept fixed are reported in the bottom part of the table.

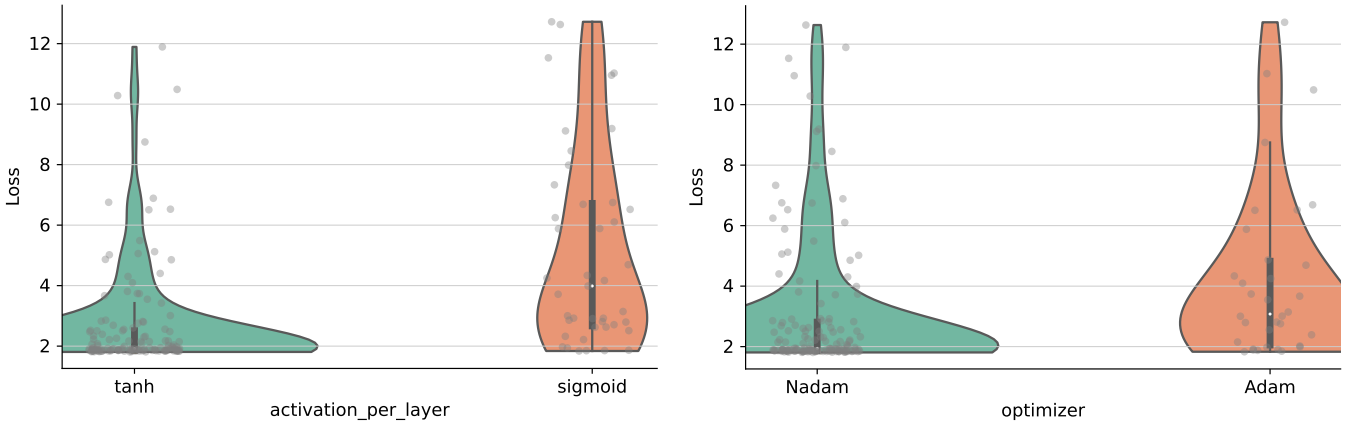


**Figure 3.2.** The values taken by the hyperoptimisation loss function Eq. (3.24) for the type of activation function (left) and the type of optimiser (right). Results are based on a scan of  $n_{\text{trials}} = 200$  configurations. The filled regions indicate the reconstructed probability distributions using the kernel density estimate method.

To determine the best set of hyperparameters in NNPDPOL2.0, we performed a scan of  $n_{\text{trials}} = 200$  possible configurations, distributed across four A100 Nvidia GPUs, with  $N_{\text{rep}} = 60$  replicas and  $n_{\text{folds}} = 4$  as in Table 3.2. The values of the two hyperoptimisation metrics considered here, Eq. (3.24) and Eq. (3.26), are displayed in Fig. 3.1 for all the  $n_{\text{trials}}$  configurations of model hyperparameters. The selected model is highlighted. As reported in the unpolarised case [49], while a large number of models displays a very similar quality of agreement with the central value of the non-fitted folds, Eq. (3.24), a much wider spread is obtained for the metric that measures the PDF uncertainties, Eq. (3.26), which is eventually used to select the optimal model. The selected values of the hyperparameters are reported in Table 3.3. These will be adopted in the rest of this paper. Finally, Fig. 3.2 displays the loss function, Eq. (3.24), for the type of activation function and the type of optimiser. The filled regions are the reconstructed probability distributions using the kernel density estimate method.

## 4 Results

In this section, we present the NNPDPOL2.0 parton set. We first discuss its perturbative stability, in terms of fit quality and of PDFs. We then compare the NNPDPOL2.0 PDFs to the previous NNPDPOL1.1 PDFs and to those in other recent NNLO determinations. We finally study the dependence of the NNPDPOL2.0 parton set upon variations of the positivity constraint and on the data set.

## 4.1 Fit quality, parton distributions, and perturbative stability

In Table 4.1, we display the number of data points  $N_{\text{dat}}$  and the  $\chi^2$  per data point corresponding to the LO, NLO, and NNLO NNPDFPOL2.0 baseline determinations. For each perturbative order, we display a pair of values, corresponding to fits without and with inclusion of MHOUs, as discussed in Sect. 2.2. Specifically, the values labelled as “no MHOUs” correspond to the  $\chi^2$  computed using the experimental covariance matrix (reconstructed only from knowledge of experimental uncertainties and their correlations), whereas the values labelled as “MHOUs” correspond to the  $\chi^2$  computed using the sum of the experimental and theory covariance matrices (estimated by means of the scale variation prescriptions outlined in Sect. 2.2). In neither case the  $\chi^2$  corresponds to the figure of merit utilised for parameter optimisation, Eq. (3.7). Values are displayed for each data set included in the fits, for data sets aggregated according to the process categorisation introduced in Sect. 2.2, and for the total data set.

From inspection of Table 4.1, we can assess the impact of the perturbative accuracy and of MHOUs on the fit quality, as quantified by the value of the  $\chi^2$  per data point. Without MHOUs, the  $\chi^2$  decreases when moving from LO to NLO, while it remains essentially unchanged when moving from NLO to NNLO. With MHOUs, it again decreases when moving from LO to NLO, whereas it slightly increases when moving from NLO to NNLO. The observed LO to NLO decrease amounts to 0.14 and 0.13, in the cases of fits without and with MHOUs, respectively. This corresponds to about three sigma in units of the distribution of the  $\chi^2$  per data point, with  $N_{\text{dat}} = 951$  data points. Comparatively, the NLO to NNLO increase observed in the fit with MHOUs amounts to 0.05, which is about one sigma. It can therefore be regarded as a statistical fluctuation. We also note that the difference between the  $\chi^2$  computed without and with MHOUs decreases as the perturbative order increases.

This trend, observed on the global data set, is mostly driven by the inclusive DIS data sets, which represent about 74% of the entire data set. In the case of inclusive DY, the  $\chi^2$  fluctuates a little more, again with a minimum at NLO, however we do not deem these fluctuations significant, given the smallness of the data set. In the case of single-inclusive jet and di-jet production, the fit quality is essentially insensitive to the perturbative order or the inclusion of MHOUs, and always remains of order one.

All of these facts lead us to three conclusions. First, that the impact of NNLO perturbative corrections on the fit quality is almost immaterial. Second, and consistently, that the impact of MHOUs is moderate at LO and NLO and very limited at NNLO. Third, and consequently, that, with the current data set, theoretical framework, and methodology, the perturbative expansion has converged. It is therefore plausible to expect that, had perturbative corrections to splitting functions and matrix elements been known beyond NNLO, one would have not observed a further improvement of the fit quality.

It is interesting to note that a similar behaviour was also seen in unpolarised PDFs [94], although one order higher in the perturbative expansion. In this respect, fits of polarised PDFs look significantly more insensitive to the perturbative accuracy than their unpolarised counterparts. We ascribe this evidence to the fact that unpolarised and polarised PDF fits rely on measurements for different physical observables: the former on cross sections; the latter on spin asymmetries. By definition, an asymmetry is a ratio of cross sections, whereby most of the theoretical corrections, including those of perturbative origin, cancel out.

We then examine the polarised PDFs. We compare the LO, NLO, and NNLO NNPDFPOL2.0 PDFs, obtained without and with inclusion of MHOUs, in Figs. 4.1 and 4.2, respectively. Specifically, we show the polarised up, anti-up, down, anti-down, strange and gluon PDFs, as a function of  $x$  in logarithmic scale at  $Q = 10$  GeV. Error bands correspond to one sigma PDF uncertainties, which do not (no MHOUs sets) or do (MHOUs sets) include MHOUs on theoretical predictions as specified in Sect. 2.2.

The features observed in the fit quality are consistently manifest on PDFs. Without MHOUs, we see that the PDF dependence on the perturbative order is generally mild, and milder when moving from NLO to NNLO than from LO to NLO. This can be noticed, in particular, in the polarised gluon PDF around  $x \sim 0.3$ , where the difference between the LO and NLO central values is about one sigma, whereas the same difference between the NLO and NNLO is almost null. With MHOUs, differences become even milder. The shift in the PDF central value due to inclusion of higher order corrections (both NLO and NNLO) is comfortably encompassed by the uncertainty of the LO PDF. This fact confirms that the MHOUs covariance matrix estimated through scale variation is correctly reproducing the effect due to higher perturbative orders.

We therefore conclude that the LO PDFs with MHOUs are almost as accurate as their NLO and NNLO counterparts. They are however a little less precise, as we can see from their uncertainties that are larger than those of their NLO and NNLO counterparts. This is particularly visible in the case of the polarised up

| Dataset                             | $N_{\text{dat}}$ | LO       |       | NLO      |       | NNLO     |       |
|-------------------------------------|------------------|----------|-------|----------|-------|----------|-------|
|                                     |                  | no MHOUs | MHOUs | no MHOUs | MHOUs | no MHOUs | MHOUs |
| EMC $g_1^p$                         | 10               | 0.86     | 0.75  | 0.64     | 0.93  | 0.71     | 0.72  |
| SMC $g_1^p$                         | 12               | 0.88     | 0.70  | 0.44     | 0.56  | 0.53     | 0.49  |
| SMC $g_1^d$                         | 12               | 1.25     | 1.38  | 1.32     | 1.24  | 1.29     | 1.04  |
| SMC low- $x$ $g_1^p/F_1^p$          | 8                | 1.80     | 1.42  | 1.51     | 1.21  | 1.48     | 1.22  |
| SMC low- $x$ $g_1^d/F_1^d$          | 8                | 0.52     | 0.56  | 0.54     | 0.56  | 0.52     | 0.49  |
| COMPASS $g_1^p$                     | 17               | 1.50     | 1.04  | 0.75     | 0.53  | 0.89     | 0.63  |
| COMPASS $g_1^d$                     | 15               | 0.86     | 1.07  | 0.57     | 0.76  | 0.62     | 0.57  |
| E142 $g_1^n$                        | 8                | 6.40     | 4.83  | 3.34     | 1.81  | 3.24     | 1.00  |
| E143 $g_1^p$                        | 27               | 2.81     | 1.57  | 0.99     | 0.84  | 1.00     | 0.98  |
| E143 $g_1^d$                        | 27               | 1.40     | 1.73  | 1.31     | 1.46  | 1.36     | 1.32  |
| E154 $g_1^n$                        | 11               | 1.20     | 0.63  | 0.30     | 0.43  | 0.40     | 0.33  |
| E155 $g_1^p/F_1^p$                  | 24               | 0.49     | 0.53  | 0.64     | 1.00  | 0.86     | 0.75  |
| E155 $g_1^n/F_1^n$                  | 24               | 0.64     | 0.58  | 0.62     | 0.56  | 0.75     | 0.49  |
| HERMES $g_1^n$                      | 9                | 0.26     | 0.23  | 0.24     | 0.20  | 0.22     | 0.19  |
| HERMES $g_1^p$                      | 15               | 3.71     | 1.85  | 1.07     | 1.03  | 1.46     | 1.29  |
| HERMES $g_1^d$                      | 15               | 2.04     | 2.22  | 1.10     | 1.30  | 1.33     | 1.20  |
| JLAB E06 014 $g_1^n/F_1^n$          | 4                | 4.58     | 3.49  | 4.57     | 3.35  | 4.73     | 4.01  |
| JLAB E97 103 $g_1^n$                | 2                | 13.4     | 0.91  | 4.29     | 1.02  | 4.44     | 0.68  |
| JLAB E99 117 $g_1^n/F_1^n$          | 1                | 0.36     | 0.01  | 0.53     | 0.05  | 0.75     | 0.32  |
| JLAB EG1 DVCS $g_1^p/F_1^p$         | 21               | 0.15     | 0.32  | 0.21     | 0.31  | 0.17     | 0.19  |
| JLAB EG1 DVCS $g_1^d/F_1^d$         | 19               | 0.37     | 0.26  | 0.30     | 0.38  | 0.27     | 0.23  |
| JLAB EG1B $g_1^p/F_1^p$             | 114              | 0.78     | 0.79  | 0.80     | 0.80  | 0.89     | 0.83  |
| JLAB EG1B $g_1^d/F_1^d$             | 301              | 0.94     | 0.93  | 0.93     | 0.94  | 0.93     | 0.92  |
| DIS NC                              | 704              | 1.15     | 1.03  | 0.97     | 0.86  | 0.95     | 0.93  |
| STAR $A_L^{W^+}$                    | 6                | 0.90     | 0.77  | 0.33     | 0.45  | 0.94     | 1.00  |
| STAR $A_L^{W^-}$                    | 6                | 1.56     | 1.44  | 0.80     | 1.05  | 1.05     | 1.06  |
| DY CC                               | 12               | 1.34     | 1.36  | 1.08     | 0.82  | 1.13     | 1.17  |
| PHENIX $A_{LL}^{1\text{-jet}}$      | 6                | 0.22     | 0.21  | 0.22     | 0.21  | 0.21     | 0.21  |
| STAR $A_{LL}^{1\text{-jet}}$ (2005) | 10               | 1.12     | 1.13  | 1.12     | 1.11  | 1.11     | 1.10  |
| STAR $A_{LL}^{1\text{-jet}}$ (2006) | 9                | 0.53     | 0.53  | 0.51     | 0.53  | 0.54     | 0.53  |
| STAR $A_{LL}^{1\text{-jet}}$ (2009) | 22               | 0.76     | 0.77  | 0.73     | 0.81  | 0.80     | 0.78  |
| STAR $A_{LL}^{1\text{-jet}}$ (2012) | 14               | 1.49     | 1.52  | 1.54     | 1.54  | 1.48     | 1.50  |
| STAR $A_{LL}^{1\text{-jet}}$ (2013) | 14               | 1.38     | 1.28  | 1.25     | 1.32  | 1.38     | 1.37  |
| STAR $A_{LL}^{1\text{-jet}}$ (2015) | 22               | 1.23     | 1.07  | 1.14     | 1.07  | 1.21     | 1.12  |
| JETS                                | 97               | 1.04     | 1.04  | 1.03     | 1.03  | 1.05     | 1.03  |
| STAR $A_{LL}^{2\text{-jet}}$ (2009) | 33               | 1.20     | 1.19  | 1.31     | 1.29  | 1.27     | 1.28  |
| STAR $A_{LL}^{2\text{-jet}}$ (2012) | 42               | 1.15     | 1.15  | 1.20     | 1.19  | 1.19     | 1.17  |
| STAR $A_{LL}^{2\text{-jet}}$ (2013) | 49               | 0.83     | 0.82  | 0.82     | 0.81  | 0.82     | 0.82  |
| STAR $A_{LL}^{2\text{-jet}}$ (2015) | 14               | 1.24     | 1.14  | 1.10     | 1.13  | 1.27     | 1.14  |
| DIJETS                              | 138              | 1.06     | 1.05  | 1.08     | 1.08  | 1.09     | 1.07  |
| Total                               | 951              | 1.12     | 1.03  | 0.98     | 0.90  | 0.97     | 0.95  |

**Table 4.1.** The number of data points  $N_{\text{dat}}$  and the  $\chi^2$  per data point corresponding to the LO, NLO, and aNNLO NNPDFPOL2.0 baseline determinations, without and with inclusion of MHOUs (see text for details). Values are quoted for each data set included in the fits, for data sets aggregated according to the process categorisation introduced in Sect. 2.2, and for the total data set.

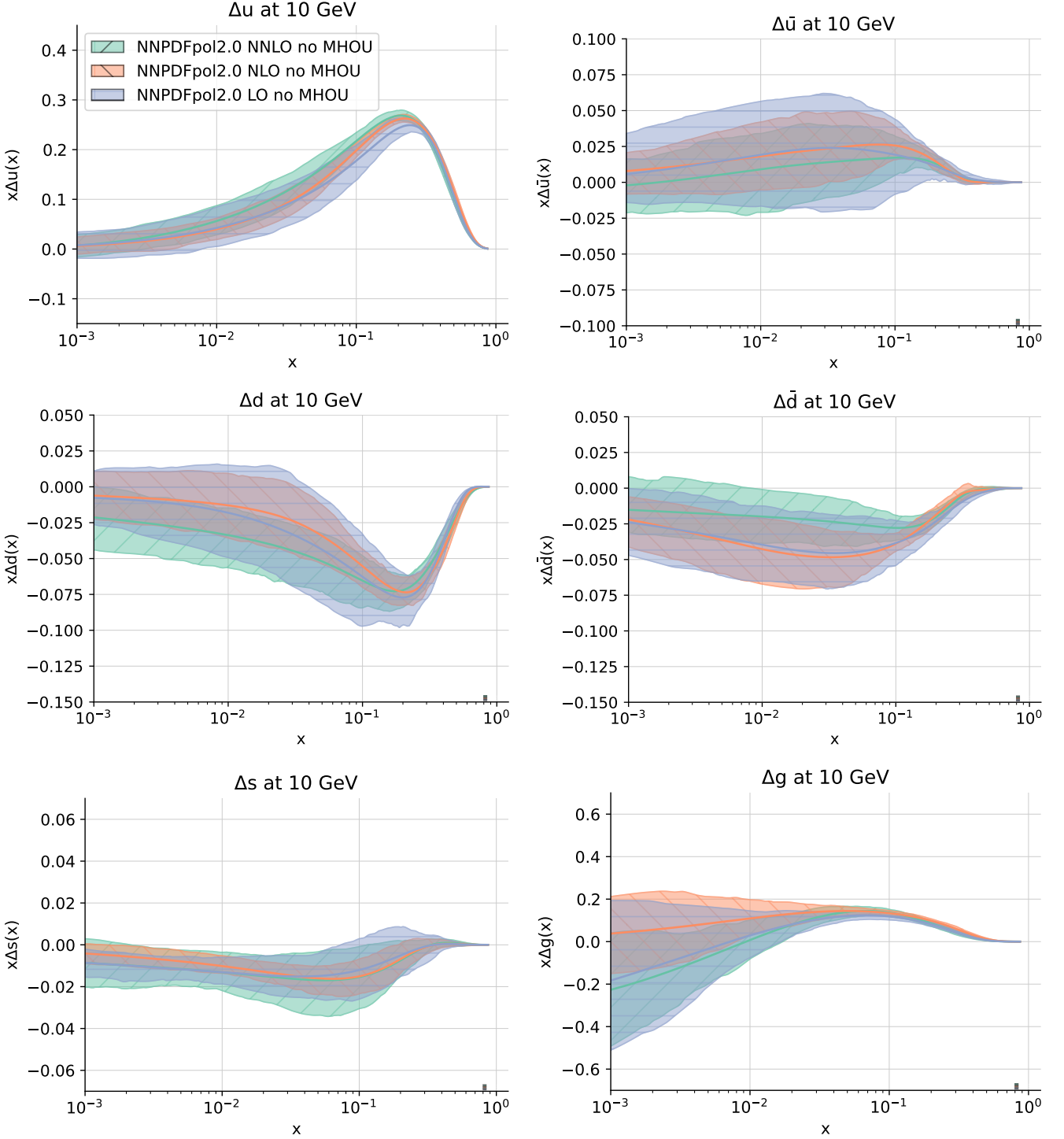


**Figure 4.1.** The LO, NLO, and NNLO NNPdfPOL2.0  $\Delta u$ ,  $\Delta \bar{u}$ ,  $\Delta d$ ,  $\Delta \bar{d}$ ,  $\Delta s$ , and  $\Delta g$  PDFs as a function of  $x$  in logarithmic scale at  $Q = 10$  GeV. Error bands correspond to one sigma PDF uncertainties, not including MHOUs on the theory predictions used in the fit.

and anti-up quarks at intermediate-to-large values of  $x$ . Inclusion of MHOUs does not inflate uncertainties significantly, as one can realise by comparing Fig. 4.1 with Fig. 4.2. This means that correlations across factorisation and renormalisation scale variations (see Fig. 2.3) counteract the inflation of the diagonal elements of the covariance matrix (see Fig. 2.4) due to the inclusion of the MHOUs covariance matrix.

A final evidence of the excellent perturbative stability of the NNPdfPOL2.0 sets is provided by the comparison of theoretical predictions and experimental data. In Fig. 4.3, we display such a comparison for a representative selection of the data sets included in NNPdfPOL2.0, specifically: the longitudinal single-spin asymmetry for  $W^\pm$ -boson production measured by the STAR experiment at a centre-of-mass energy of 510 GeV [77]; the longitudinal double-spin asymmetry for single-inclusive jet production from the

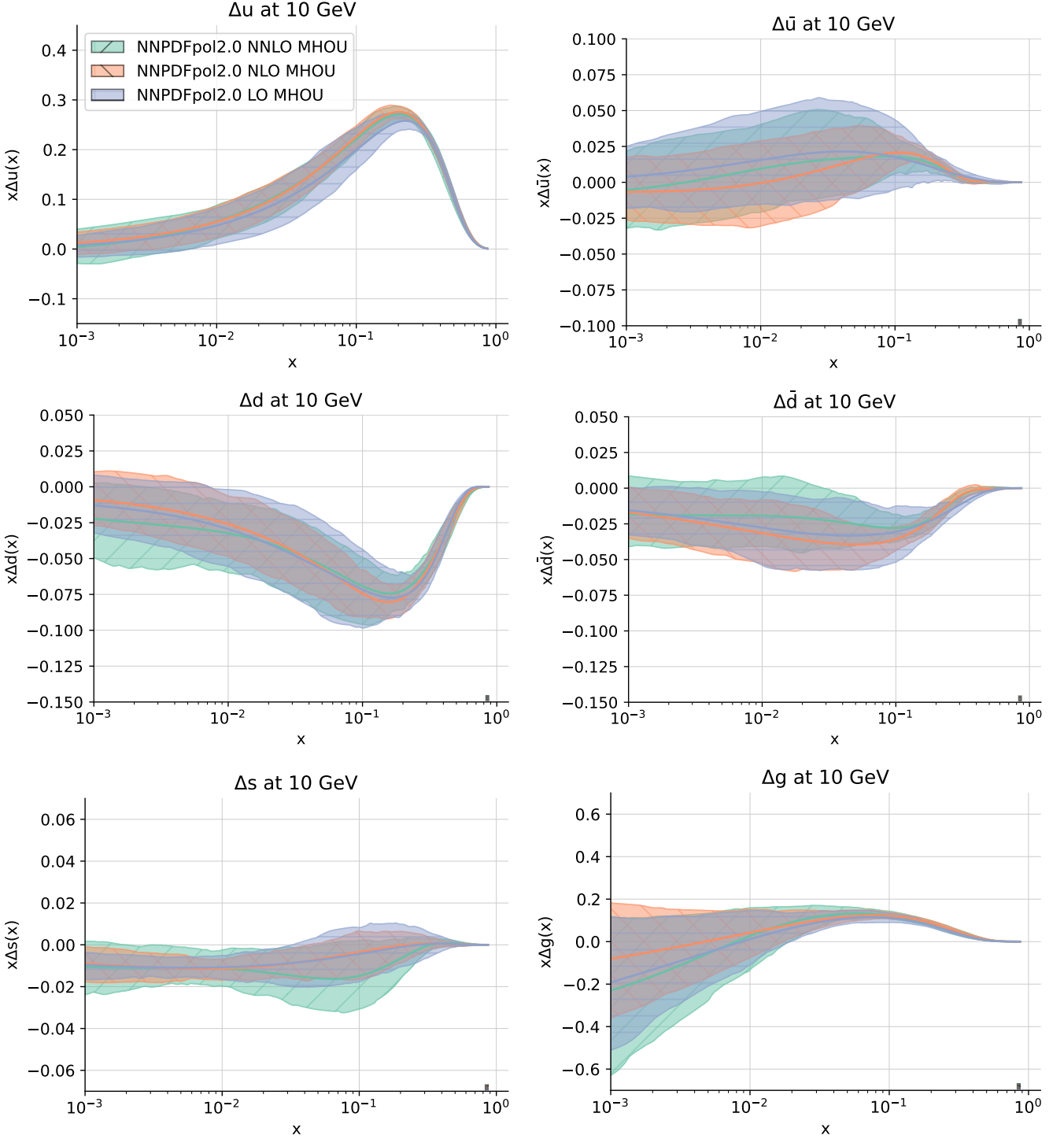


**Figure 4.2.** Same as Fig. 4.1 for the LO, NLO and NNLO NNPDFPOL2.0 PDFs that include MHOUs.

2013 [85] and 2015 (in the central rapidity region) [83] runs measured by the STAR experiment at centre-of-mass energies of 510 GeV and 200 GeV, respectively; and the longitudinal double-spin asymmetry for di-jet production from the same 2013 (topology [A]) [85] and 2015 (opposite-sign [OS] topology) [83] runs. Theoretical predictions are computed at LO, NLO, and NNLO with the corresponding MHOUs NNPDFPOL2.0 PDF sets. The unpolarised PDF is taken consistently from the LO, NLO, and NNLO NNPDF4.0 central set. For single-inclusive jet and di-jet asymmetries, NNLO predictions are approximate, in that splitting functions used for parton evolution are accurate to NNLO, whereas matrix elements are accurate only to NLO. Experimental uncertainties are the sum in quadrature of all statistical and systematic uncertainties. Uncertainties on theoretical predictions correspond to one-sigma polarised PDF uncertainties only. As we can see from Fig. 4.3, theoretical predictions are in good agreement with experimental data and vary only mildly with the perturbative accuracy.

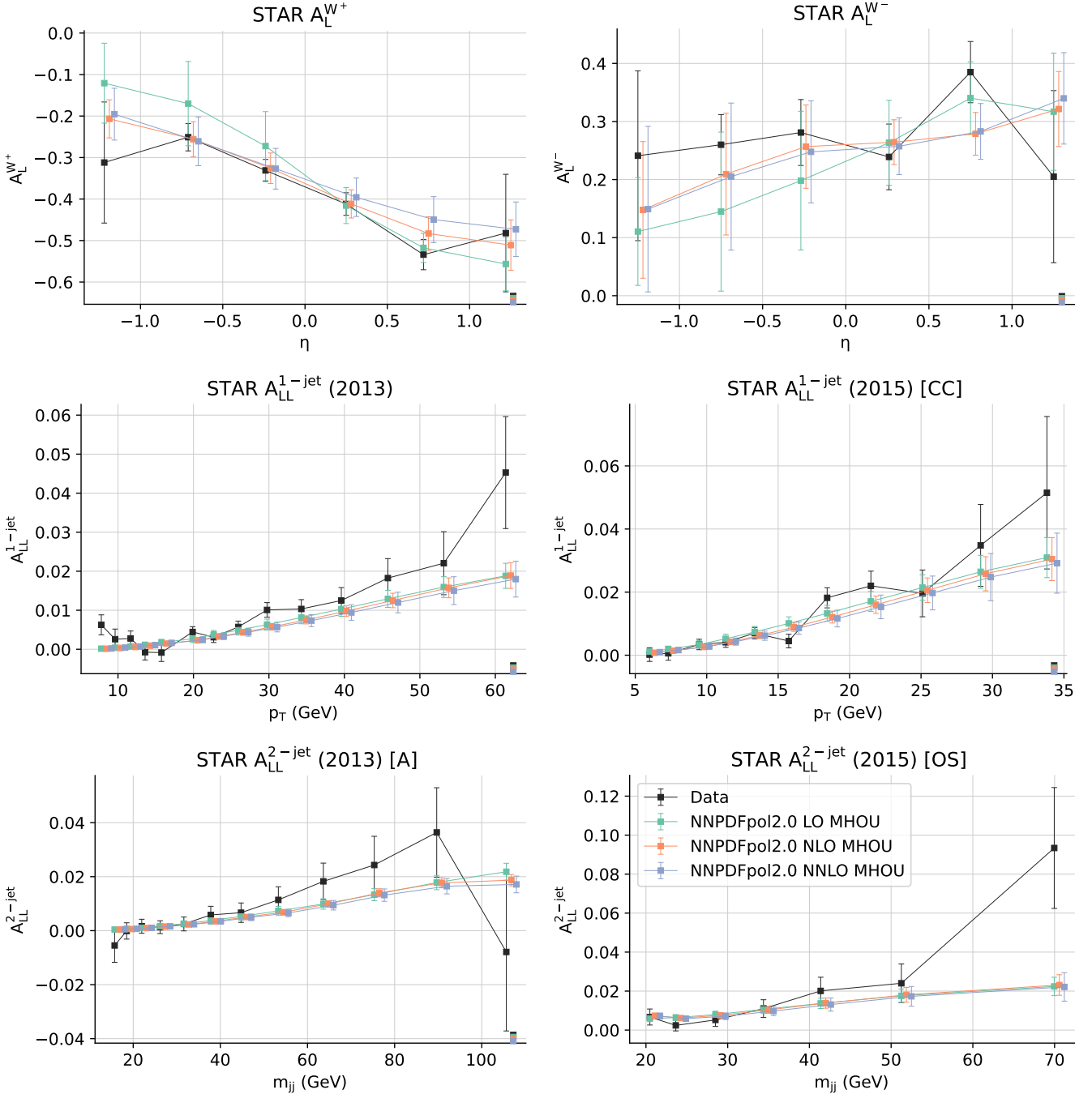


**Figure 4.3.** Comparison between a representative selection of the data sets included in NNPDFPOL2.0 and the corresponding theoretical predictions. Specifically, from top to bottom, we display: the longitudinal single-spin asymmetry for  $W^\pm$ -boson production measured by the STAR experiment at a centre-of-mass energy of 510 GeV [77]; the longitudinal double-spin asymmetry for single-inclusive jet production from the 2013 [85] and 2015 (in the central rapidity region) [83] runs measured by the STAR experiment at centre-of-mass energies of 510 GeV and 200 GeV, respectively; and the longitudinal double-spin asymmetry for di-jet production from the same 2013 (topology [A]) [85] and 2015 (opposite-sign [OS] topology) [83] runs. Theoretical predictions are computed at LO, NLO, and NNLO with the corresponding MHOUs NNPDFPOL2.0 PDF sets. The unpolarised PDF is taken consistently from the LO, NLO, and NNLO NNPDF4.0 central set. For single-inclusive jet and di-jet asymmetries, NNLO predictions are approximate, in that splitting functions used for parton evolution are accurate to NNLO, whereas matrix elements are accurate only to NLO. Experimental uncertainties are the sum in quadrature of all statistical and systematic uncertainties. Uncertainties on theoretical predictions correspond to one-sigma polarised PDF uncertainties only.

## 4.2 Comparison to NNPDFPOL1.1 and to other PDF sets

In Figs. 4.4 and 4.5 we compare the NNPDFPOL2.0 polarised PDFs, respectively, to the NNPDFPOL1.1 PDFs [30], and to other recent polarised PDFs, namely BDSSV24 [32] and MAPPDFPOL1.0 [31]. All these

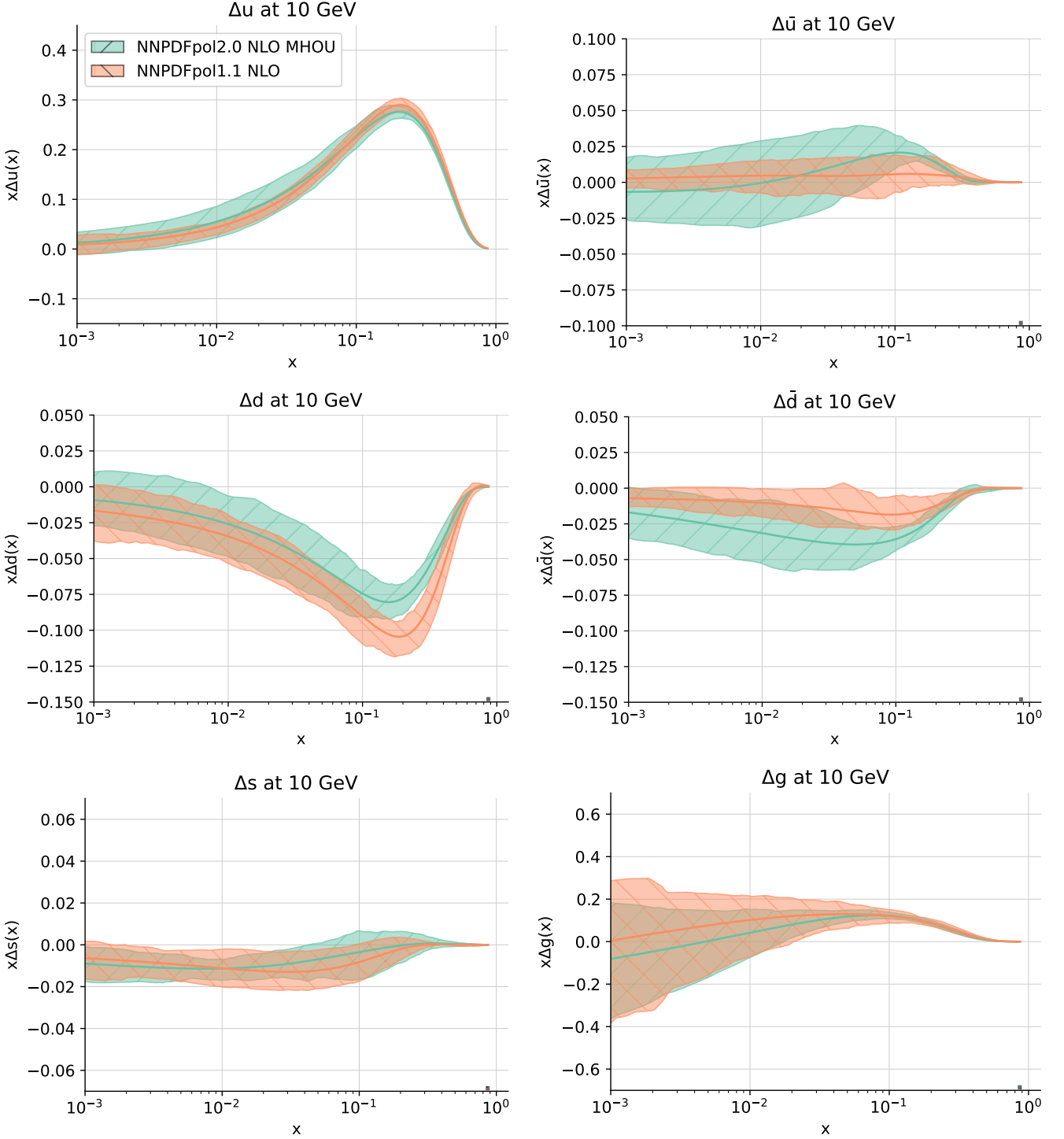


**Figure 4.4.** Comparison of the NLO NNPDFPOL2.0 and NNPDFPOL1.1 PDFs as a function of  $x$  at  $Q = 10$  GeV, in the same format as Fig. 4.1.

PDF sets are provided as Monte Carlo replica ensembles: therefore, bands correspond to one-sigma uncertainties computed over the corresponding nominal number of replicas. When comparing to NNPDFPOL1.1, we consider the NLO MHO version of NNPDFPOL2.0, given that the highest accuracy of NNPDFPOL1.1 is NLO. When comparing to BDSSV24 and MAPPDFPOL1.0, we consider the NNLO MHO version of NNPDFPOL2.0 and the NNLO version of the other sets. The comparisons in Figs. 4.4 and 4.5 are otherwise in the same format as Fig. 4.1.

We first inspect the comparison of NNPDFPOL2.0 to NNPDFPOL1.1. We generally observe a fair agreement between the two. For up and down polarised quarks and anti-quarks, differences between PDF central values are the largest around  $x \sim 0.1$ , where they amount to up to slightly more than  $\sqrt{2}$ -sigma. For the strange quark and gluon PDF central values, the two sets are in perfect agreement. Uncertainties

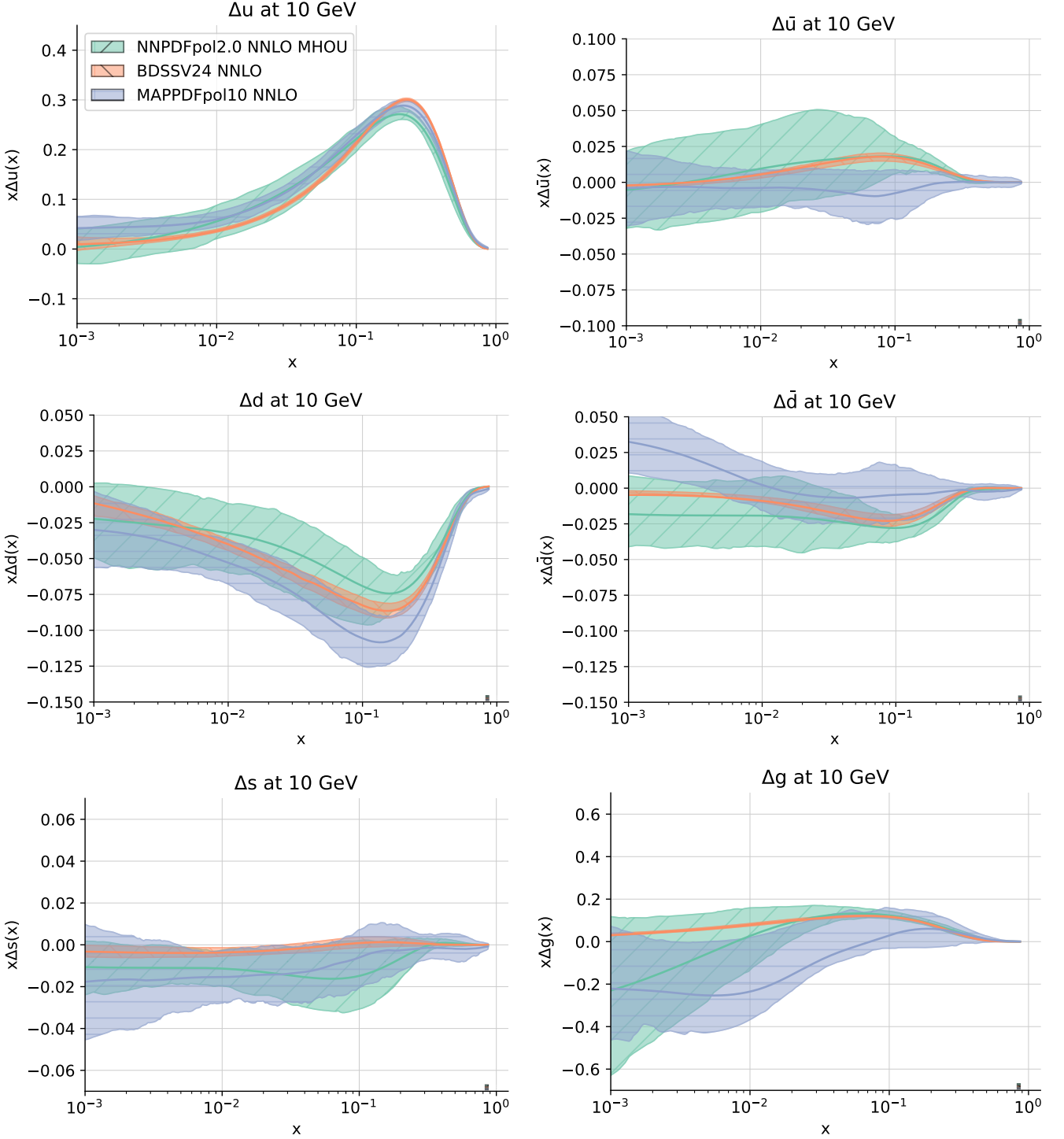


**Figure 4.5.** Comparison of the NNLO NNPDFPOL2.0 (with MHOUs), BDSSV, and MAPPDFpol10 PDFs as a function of  $x$  at  $Q = 10$  GeV, in the same format as Fig. 4.1.

are likewise similar, except for anti-quarks and the gluon PDFs. In the former case, they are smaller in NNPDFPOL1.1; in the latter case, they are smaller in NNPDFPOL2.0. To understand this behaviour, it is useful to remind what the differences are between the NNPDFPOL1.1 and NNPDFPOL2.0 determinations, both in terms of experimental data and methodological details of each of them.

Concerning experimental data, as detailed in Sect. 2.1, both analyses are based on fixed-target inclusive DIS data, and on collider  $W$ -boson and single-inclusive jet production data. The NNPDFPOL2.0 data set is however updated and extended with respect to the NNPDFPOL1.2 one. In particular, more modern DIS measurements for COMPASS and JLab experiments, the combined  $W$ -boson RHIC measurement, and a larger array of RHIC single-inclusive and di-jet measurements have been included in NNPDFPOL2.0. Among all of these, the RHIC data play a leading role. The replacement of the  $W$ -boson measurement of



Ref. [78], included in NNPDFPOL1.1, with the measurement of Ref. [77], now included in NNPDFPOL2.0, is responsible for the enhancement of the anti-up quark and the depletion of the anti-down quark at large  $x$ . As can be seen in Ref. [77] (see in particular Fig. 5), the newer measurement, which increases the luminosity of the older by about a factor of three, is not only more precise, but it also has a preference for values of the  $W^-$  ( $W^+$ ) cross section that are a little higher (lower) than those predicted by NNPDFPOL2.0. This means that, roughly, the anti-up quark should be enhanced and the anti-down quark should be suppressed, as we indeed observe in Fig. 4.4. This conclusion aligns with what the authors of Ref. [77] observe when reweighting NNPDFPOL1.1 with their newer measurement. At the same time, because the newer DIS data do not alter the sum of quarks and anti-quarks with respect to NNPDFPOL1.1, the NNPDFPOL2.0 polarised up (down) PDF is depleted (enhanced) by an amount equal to that by which the polarised anti-up (anti-down) PDF is enhanced (depleted). On the other hand, the significant amount of newer RHIC single-inclusive jet and di-jet production data are responsible for the reduction of the polarised gluon PDF uncertainty. We will further comment on the relative impact of single-inclusive jet and di-jet measurements in Sect. 4.3.

Concerning methodological details, NNPDFPOL1.1 was obtained by reweighting [51] a certain prior PDF set with collider  $W$ -boson and single-inclusive jet production data. The prior was constructed by performing a fit to inclusive DIS data only, and by enforcing the separation of up and down quark and anti-quark PDFs — to which inclusive DIS measurements are insensitive by construction — to the result of the DSSV fit [104, 105]. Up and down quark and anti-quark separation was achieved by fitting SIDIS data in DSSV. Different prior PDF sets were considered, by taking once, twice, three times or four times the nominal DSSV one-sigma uncertainty. It was checked that the posterior became insensitive to the prior for a sufficiently large inflation of the DSSV uncertainties (three-sigma or more). This methodology can bias PDF uncertainties, if anything because the available data cannot constrain the PDFs on the whole range of  $x$ . For instance, for  $x \lesssim 0.04$  the uncertainties on the polarised anti-up and anti-down NNPDFPOL1.1 PDFs are completely determined by the assumption made in the prior. Conversely, the NNPDFPOL2.0 PDFs are determined from a fit to all the data: because of the very flexible parametrisation, any bias in the prior is reduced in comparison to NNPDFPOL1.1. In light of these considerations, we ascribe the smaller uncertainties of NNPDFPOL1.1 in comparison to NNPDFPOL2.0 seen for up and down anti-quarks to a bias in the former. In this respect, NNPDFPOL2.0 is less precise but more accurate than NNPDFPOL1.1.

We now turn to compare the NNLO NNPDFPOL2.0 PDFs to the NNLO BDSSV and MAPPDFPOL1.0 PDFs. We generally observe a fair agreement among the three sets. The shape of the PDFs is generally very similar between NNPDFPOL2.0 and BDSSV24, despite the significantly smaller uncertainties of the latter. Particularly impressive is the gluon PDF, for which, in the region constrained by experimental data,  $x \gtrsim 0.02$ , the two determination are one spot on top of the other. Somewhat larger differences, though well within one-sigma uncertainties, are observed between NNPDFPOL2.0 and MAPPDFPOL1.0. These differences regard, in particular, the up and down quark/anti-quark PDFs and the gluon PDF: the polarised anti-up (anti-down) PDF is positive (negative) in NNPDFPOL2.0, whereas it is negative (positive) in MAPPDFPOL1.0; the polarised gluon PDF is significantly more positive in NNPDFPOL2.0 than in MAPPDFPOL1.0. The size of the uncertainties is very similar in the two PDF sets, except for the gluon PF at large  $x$ , where it is significantly smaller in NNPDFPOL2.0. In order to understand this behaviour we should again consider the differences due to the data set and the methodological details of each determination.

Concerning the data set, all the three analyses are based on very similar sets of inclusive DIS data; the BDSSV24 and MAPPDFPOL1.0 set also include semi-inclusive DIS data, from the COMPASS and HERMES experiments; the NNPDFPOL2.0 and BDSSV24 sets also include polarised collider data:  $W$ -boson and single-inclusive jet production measurements are included in both, whereas di-jet production measurements are included only in NNPDFPOL2.0. These differences explain differences of PDF central values. Quark/anti-quark separation is driven only by SIDIS data in MAPPDFPOL1.0, only by  $W$ -boson production data in NNPDFPOL2.0, and by an admixture of the two processes in BDSSV24. As we can see from Fig. 4.5, the BDSSV24 central values of the polarised up, anti-up, down, and anti-down PDFs lie in between the NNPDFPOL2.0 and MAPPDFPOL1.0 central values. This suggests that SIDIS and  $W$ -boson production measurements tend to pull polarised quark and anti-quark PDFs in slightly opposite directions: specifically, SIDIS measurements tend to suppress (enhance) the polarised anti-up (anti-down) PDF around  $x \sim 0.1$ , whereas  $W$ -boson production measurements tend to do the opposite. Because the sum of quark and anti-quark PDFs is well constrained by inclusive DIS data, the effect is that SIDIS measurements enhance

| Data set | $N_{\text{dat}}$ | baseline | no pos. | no di-jets | no s.-i. jets | no JLab |
|----------|------------------|----------|---------|------------|---------------|---------|
| DIS NC   | 704              | 0.93     | 0.91    | 0.92       | 0.91          | 0.88    |
| DY CC    | 12               | 1.17     | 0.98    | 1.05       | 0.98          | 0.66    |
| JETS     | 97               | 1.03     | 1.00    | 1.02       | —             | 1.01    |
| DIJET    | 138              | 1.07     | 1.07    | —          | 1.07          | 1.08    |
| Total    | 951              | 0.95     | 0.93    | 0.93       | 0.94          | 0.94    |

**Table 4.2.** The number of data points  $N_{\text{dat}}$  and the  $\chi^2$  per data point corresponding to the baseline NNPDFPOL2.0 NNLO MHO fit and to variants obtained without the positivity constraint (no pos.), without di-jet measurements (no di-jet), without single-inclusive jet measurements (no s.-i. jets), and without JLab measurements (no JLab). Numerical values are displayed for data sets aggregated according to the process categorisation introduced in Sect. 2.2, and for the total data set.

(suppress) the polarised up (down) PDF by a similar amount, whereas  $W$ -boson production measurements do the opposite. On the other hand, the polarised gluon PDF is constrained by higher-order (beyond LO) contributions to the matrix elements of (semi-)inclusive DIS data and to splitting functions in all the three analyses; in NNPDFPOL2.0 and in BDSSV24, it is further constrained by LO contributions to the matrix elements of single-inclusive jet (and di-jet) production measurements. This constraint is clearly dominant with respect to the one coming from the other data sets, as expected. Be that as it may, all these differences are well encompassed by PDF uncertainties. This fact suggests that there are no major tensions across data sets, and that a fit would possibly be able to accommodate all the data sets with ease, should they all be included in a fit at the same time.

Concerning the methodological details, all the three analyses are based on a Monte Carlo PDFs, whereby the data uncertainties are represented into PDF uncertainties by means of importance sampling. They do however make use of a different parametrisation of PDFs: whereas a neural network (with a different architecture) is used by NNPDFPOL2.0 and MAPPDFPOL1.0, a simpler polynomial form is used by BDSSV24. All the three analyses enforce positivity of cross sections as in Eq. (3.21), and require that the triplet and octet sum rules in Eq. (3.5) are fulfilled. The most relevant methodological difference across methodologies is therefore the parametrisation, which may be responsible for the observed differences in PDF uncertainties. These are indeed rather similar between NNPDFPOL2.0 and MAPPDFPOL2.0, which use a neural network, while they are significantly smaller for BDSSV24, which use a polynomial. Conclusive evidence of this fact can be only reached through a benchmark study, which, despite becoming compelling, will require dedicated future work.

### 4.3 Dependence on the positivity constraint and on the data set

We now turn to study the stability of the NNPDFPOL2.0 parton set upon variations of the positivity constraint and of the input data set. Among all the theoretical, methodological, and experimental choices that enter this analysis, as detailed in Sects. 2-3, we consider that these two have the largest impact on the polarised PDFs.

Concerning the positivity constraint, we recall that we incorporate Eq. (3.21) in Eq. 3.6 by means of the penalty term defined in Eqs. (3.22)-(3.23). This positivity constraint has been deemed essential to stabilise the NNPDFPOL1.0 fit [57], in particular to drive the behaviour of polarised PDFs at large values of  $x$ , due to the scarcity of experimental data in that region. The phenomenological effect of this positivity constraint and its interplay with various experimental data have been recently investigated in [106–108], in particular relationship with the sign of the polarised gluon PDF. There it was found that, if no positivity constraints are imposed in the fit, it is possible to attain a positive polarised gluon PDF only if one simultaneously accounts for RHIC measurements of single-inclusive jet production and JLab measurements of DIS production at very large values of  $x$ . On the other hand, the validity of the LO approximation behind Eq. (3.21) was recently re-assessed in [99]. The authors confirmed the results of [98], namely that violations of Eq. 3.21 are possible, though they are of the order of percent at most.

In order to check the impact of the positivity constraint on NNPDFPOL2.0, we have performed a fit in which we set the maximum value of the Lagrange multiplier  $\Lambda_{\text{pos}}$  in Eq. (3.6) to zero. The fit is

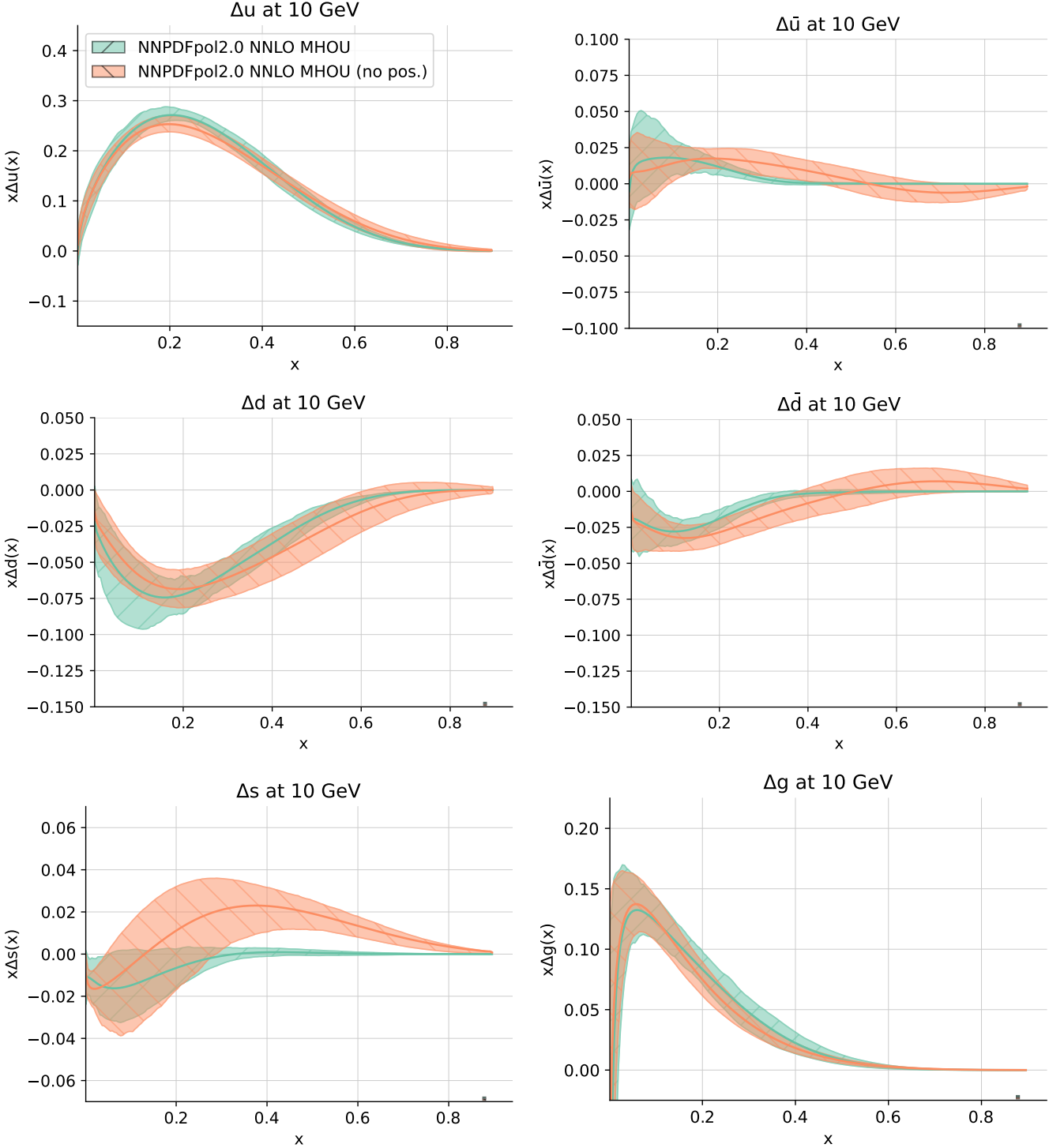


**Figure 4.6.** Comparison of the baseline NNPdfPOL2.0 NNLO MHOu polarised PDFs and PDFs obtained from an equivalent determination without the positivity constraint, Eq. (3.21). Parton distributions are reported as a function of  $x$  in linear scale at  $Q = 10$  GeV, with one-sigma uncertainty bands.

otherwise equivalent to the NNPdfPOL2.0 NNLO MHOu baseline determination. This effectively amounts to removing the positivity constraint from the fit. The corresponding fit quality, compared to the baseline, is reported, for data sets aggregated according to the process categorisation introduced in Sect. 2.2, and for the total data set, in Table 4.2. The corresponding PDFs, again compared to the baseline PDFs, are reported, as a function of  $x$  in linear scale at  $Q = 10$  GeV, in Fig. 4.6. Bands correspond to one-sigma uncertainties.

As we see from Table 4.2, the effect of removing the positivity constraint is almost immaterial on the fit quality. The improvement of the value of the  $\chi^2$ , for groups of data sets and for the total data set, is less than half a sigma, in units of the standard deviation of the  $\chi^2$  distribution, therefore it is not statistically

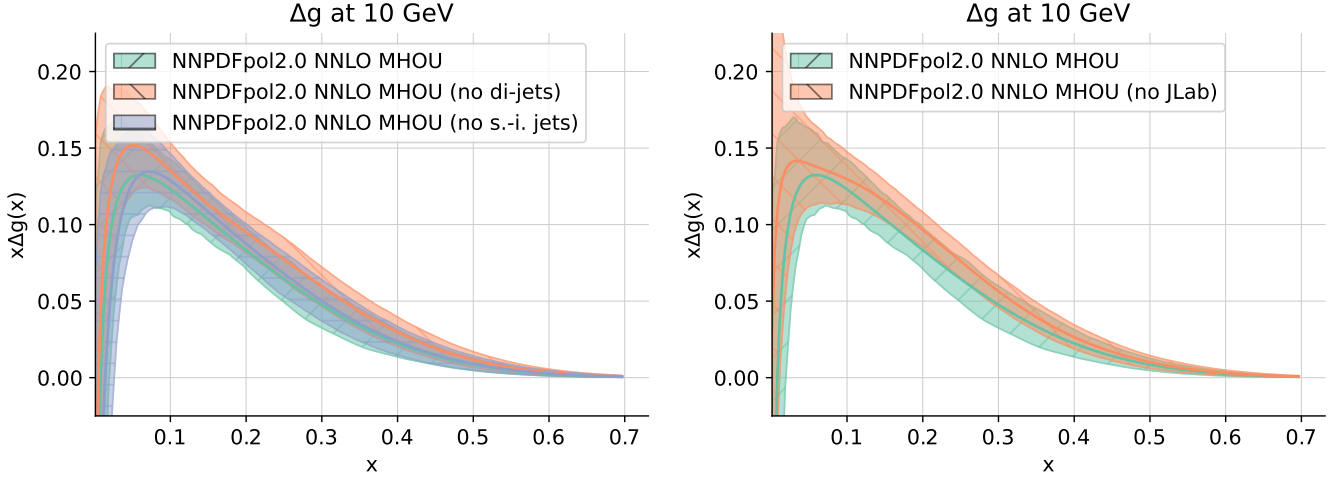


**Figure 4.7.** Comparison of the baseline NNPDFPOL2.0 NNLO MHOu polarised gluon PDF and the corresponding PDF obtained from equivalent determinations without the RHIC di-jet and single-inclusive jet measurements (left) or without the JLab DIS measurements (right). The PDF is displayed as a function of  $x$  in linear scale at  $Q = 10$  GeV, with one-sigma uncertainty bands.

significant. The effect of removing the positivity constraint is more noticeable on PDFs, for which we observe a marked increase of PDF uncertainties, especially at large values of  $x$ , see Fig. 4.6. Differences are apparent for the sea quark PDFs, in particular for the polarised strange PDF, which develops a preference for positive values. On the other hand, the variation of the gluon PDF remains rather limited, and amounts to a moderate increase of the PDF uncertainty. This fact suggests that the data included in the fit constrain the gluon PDF very well, as we discuss next.

Concerning the data set, we observe that variations are somewhat limited by the overall composition of the global data set, which does not allow us to remove measurements without affecting our ability to determine PDFs in a sufficiently sensible way. We therefore focus on three classes of measurements, which are collectively sensitive to the polarised gluon PDF at large values of  $x$ . These are the spin asymmetries measured by RHIC in di-jet and single-inclusive jet production and the structure functions measured by JLab in polarised DIS.

In order to check the impact of each of these classes of measurements, we have performed three additional fits, equivalent to the NNPDFPOL2.0 NNLO MHOu baseline determination, from which we have removed, respectively, the di-jet, the single-inclusive jet, and the JLab DIS measurements in turn. The corresponding fit quality, compared to the baseline, is reported, for data sets aggregated according to the process categorisation introduced in Sect. 2.2, and for the total data set, in Table 4.2. The corresponding gluon PDF, again compared to the baseline PDFs, are reported, as a function of  $x$  in linear scale at  $Q = 10$  GeV, in Fig. 4.7. Bands correspond to one-sigma uncertainties.

As we see from Table 4.2, the effect of removing either the di-jet or the single-inclusive jet measurements from the fit is immaterial: changes in fit quality are compatible with statistical fluctuations. The effect of removing JLab data is small. It leads to an improvement in the overall description of the DIS and DY data by about one sigma, in units of the standard deviation of the  $\chi^2$  distribution, which is however not noticeable on the global  $\chi^2$ . The effect of varying the data set is slightly more visible on the large- $x$  gluon PDF, see Fig. 4.7. In particular, we observe that single-inclusive jet measurements have a preference for a slightly larger gluon PDF in comparison to di-jet measurements. The latter actually drive the gluon PDF in the global fit, given that this is equivalent to that obtained in the fit without single-inclusive jet measurements. On the other hand, the JLab DIS measurements have a preference for a slightly smaller gluon in comparison to the global data set. All of these affects are however minor, as they are well encompassed by PDF uncertainties.

## 5 Phenomenological applications

In this section, we illustrate two phenomenological applications of the NNPDFPOL2.0 parton sets. First, we revisit the spin content of the proton, by computing the lowest moments of relevant polarised PDF

|          | $\langle \Delta g(Q) \rangle^{[\cdot, \cdot]}$ |                 |                 | $\langle \Delta \Sigma(Q) \rangle^{[\cdot, \cdot]}$ |                 |                 | $\langle \Delta g(Q) \rangle^{[\cdot, \cdot]} + 1/2 \langle \Delta \Sigma(Q) \rangle^{[\cdot, \cdot]}$ |                 |                 |
|----------|--|-----------------|-----------------|---|-----------------|-----------------|--|-----------------|-----------------|
|          | [0.001, 1]                                     | [0.02, 0.5]     | [0.05, 1]       | [0.001, 1]  | [0.02, 0.5]     | [0.05, 1]       | [0.001, 1]   | [0.02, 0.5]     | [0.05, 1]       |
| NNPDF1.1 | $0.53 \pm 0.77$                                | $0.32 \pm 0.10$ | $0.21 \pm 0.04$ | $0.13 \pm 0.07$                                     | $0.16 \pm 0.02$ | $0.16 \pm 0.01$ | $0.66 \pm 0.83$  | $0.48 \pm 0.10$ | $0.37 \pm 0.04$ |
| NNPDF2.0 | $0.11 \pm 0.81$                                | $0.31 \pm 0.08$ | $0.20 \pm 0.04$ | $0.14 \pm 0.09$                                     | $0.17 \pm 0.03$ | $0.16 \pm 0.02$ | $0.24 \pm 0.88$  | $0.48 \pm 0.08$ | $0.36 \pm 0.04$ |
| BDSSV    | $0.47 \pm 0.07$                                | $0.29 \pm 0.02$ | $0.19 \pm 0.01$ | $0.18 \pm 0.01$                                     | $0.19 \pm 0.01$ | $0.19 \pm 0.01$ | $0.65 \pm 0.08$  | $0.48 \pm 0.02$ | $0.38 \pm 0.01$ |

**Table 5.1.** The truncated moments, Eq. (5.1), of the gluon, singlet, and the sum of the former and of half of the latter, computed with the NNPDFpol1.1 NLO (NNpol1.1), NNPDFpol2.0 NNLO MHOU (NNpol2.0), and BDSSV24 NNLO (BDSSV) PDF sets, at  $Q = 10$  GeV in three integration intervals  $[x_{\min}, x_{\max}]$ : [0.001, 1], [0.02, 0.5], and [0.05, 1]. Errors correspond to one-sigma PDF uncertainties.

combinations. Second, we compare predictions of single-hadron production in polarised DIS and in proton-proton collisions with recent experimental measurements.

## 5.1 The spin content of the proton revisited

The lowest moments of the gluon and singlet polarised PDFs are proportional to the proton axial currents, which express the fraction of the proton spin carried by gluons and quarks. If one defines these moments as

$$\langle \Delta f(Q) \rangle^{[x_{\min}, x_{\max}]} = \int_{x_{\min}}^{x_{\max}} dx \Delta f(x, Q), \quad (5.1)$$

the Jaffe-Manohar sum rule [109] reads, in natural units, as

$$\frac{1}{2} = \langle \Delta g(Q) \rangle^{[0,1]} + \frac{1}{2} \langle \Delta \Sigma(Q) \rangle^{[0,1]} + \mathcal{L}_g(Q) + \mathcal{L}_q(Q), \quad (5.2)$$

where  $\mathcal{L}_g(Q)$  and  $\mathcal{L}_q(Q)$  are the canonical gluon and quark orbital angular momenta. We therefore seek to compute the first two terms of Eq. (5.2). However, because the available piece of experimental information does not allow for an accurate determination of polarised PDFs over the whole range of  $x$  [110], we rather consider truncated quantities, for which  $x_{\min} > 0$  and  $x_{\max} < 1$ .

In Fig. 5.1 we display the truncated moments, Eq. (5.1), of the gluon and quark PDFs, together with the sum of the former and of half of the latter. The moments are computed as a function of  $x_{\min}$ , with  $5 \cdot 10^{-4} < x_{\min} < 1$ , with fixed  $x_{\max} = 1$ , and at  $Q = 10$  GeV. The NNPDFPOL2.0 NLO and NNLO PDF sets, without and with MHOU are used. Bands correspond to one-sigma PDF uncertainties. In Table 5.1 we report the values of the same quantities computed with the NNPDFPOL1.1 NLO (NNpol1.1), NNPDFPOL2.0 NNLO MHOU (NNpol2.0), and BDSSV24 NNLO (BDSSV) PDF sets. Values are determined at  $Q = 10$  GeV, in three integration intervals  $[x_{\min}, x_{\max}]$ : [0.001, 1], [0.02, 0.5], and [0.05; 1]. These roughly correspond to the kinematic ranges covered by the entire data set, by the single-inclusive jet and di-jet data, and by the large- $x$  DIS data.

From inspection of Fig. 5.1 and Table 5.1, we make the following observations on the determination of the truncated moments of the gluon and singlet PDFs. These observations also apply to the residual proton spin fraction not carried by the spin of gluons and quarks. First, the accuracy of the determination depends very weakly on the perturbative accuracy of the PDF fit. This result is consistent with the conclusions on fit quality and perturbative stability reached in Section 4.1. Second, the precision of the determination strongly depends on the contribution coming from the small- $x$  integration region, which remains completely unknown. Because of this fact, the spin of gluons and quarks could account for the total proton spin budget. Third, in the region covered by experimental data, the three determinations obtained using different PDF sets are in remarkable agreement with each other. Moving from NNPDFPOL1.1 to NNPDFPOL2.0, we observe a slight reduction of the uncertainty on the truncated moment of the gluon PDF in the integration region [0.02,0.5] covered by single-inclusive jet and di-jet measurements; on the other hand, we observe a slight increase of the uncertainty on the truncated moment of both the gluon and singlet PDFs in the widest integration region [0.001, 1]. As discussed in Section 4.2, the first effect is due to the largest array of RHIC measurements included in NNPDFPOL2.0, whereas the second effect is due to an extrapolation bias in NNPDFPOL1.1 associated to the choice of Bayesian prior. Moving from NNPDFPOL2.0 to BDSSV24, we

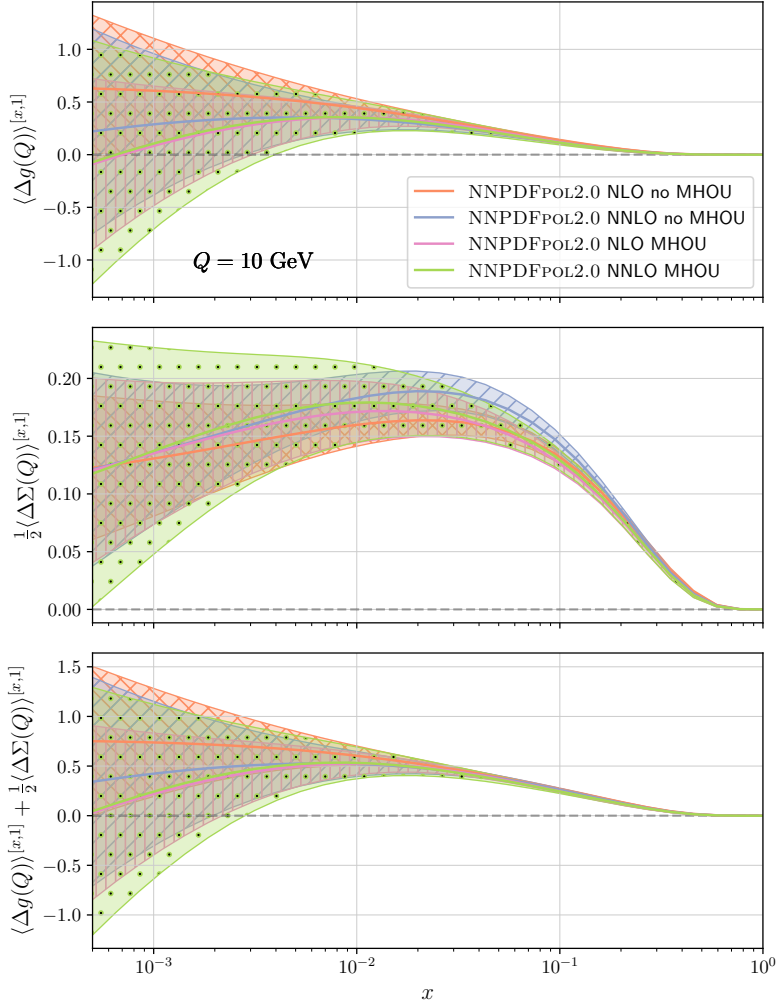


**Figure 5.1.** The truncated moments, Eq. (5.1), of the gluon (top) and singlet (middle) PDFs, together with the sum of the former and of half of the latter (bottom). The moments are computed as a function of  $x_{\min}$ , with  $5 \cdot 10^{-4} < x_{\min} < 1$ , with fixed  $x_{\max} = 1$ , and at  $Q = 10$  GeV. The NLO and NNLO NNPdFpol2.0 PDF sets, without and with MHOUs are used. Bands correspond to one-sigma PDF uncertainties.

|          | $\langle \Delta u^+(Q) \rangle_{[0.001,1]}$ |                  | $\langle \Delta d^+(Q) \rangle_{[0.001,1]}$ |                  | $\langle \Delta s^+(Q) \rangle_{[0.001,1]}$ |                  | $\langle x(\Delta u^- - \Delta d^-)(Q) \rangle_{[0.001,1]}$ |                  |
|----------|---|------------------|---|------------------|---|------------------|---|------------------|
|          | $Q = 2$ GeV                                 | $Q = 10$ GeV     | $Q = 2$ GeV                                 | $Q = 10$ GeV     | $Q = 2$ GeV                                 | $Q = 10$ GeV     | $Q = 2$ GeV   | $Q = 10$ GeV     |
| NNpol2.0 | $+0.81 \pm 0.07$                            | $+0.79 \pm 0.08$ | $-0.40 \pm 0.05$                            | $-0.39 \pm 0.06$ | $-0.13 \pm 0.13$                            | $-0.13 \pm 0.13$ | $+0.17 \pm 0.02$  | $+0.13 \pm 0.01$ |

**Table 5.2.** The truncated moments corresponding to the charge-even PDF combinations  $\Delta u^+ = \Delta u + \Delta \bar{u}$ ,  $\Delta d^+ = \Delta d + \Delta \bar{d}$ , and  $\Delta s^+ = \Delta s + \Delta \bar{s}$ , and to the PDF combination  $x(\Delta u^- - \Delta d^-) = x(\Delta u - \Delta \bar{u} - \Delta d + \Delta \bar{d})$ . The moments are computed in the integration interval  $[0.001,1]$ , at  $Q = 2$  GeV and  $Q = 10$  GeV, with the NNPdFpol2.0 NNLO MHOU PDF set (NNpol2.0).

observe larger uncertainties in the results obtained with the former PDF set, especially when extending the integration interval to the small- $x$  region, again consistently with what was observed in Section 4.2.

Finally, we compute the truncated moments corresponding to the charge-even PDF combinations  $\Delta u^+ = \Delta u + \Delta \bar{u}$ ,  $\Delta d^+ = \Delta d + \Delta \bar{d}$ , and  $\Delta s^+ = \Delta s + \Delta \bar{s}$ , and to the PDF combination  $x(\Delta u^- - \Delta d^-) = x(\Delta u - \Delta \bar{u} - \Delta d + \Delta \bar{d})$ . These combinations are routinely determined using lattice QCD [111,112], therefore these results can serve as a benchmark for those studies. We use the NNPdFpol2.0 NNLO MHOU PDF set, an integration interval  $[0.001,1]$ , and two energy scales,  $Q = 2$  GeV and  $Q = 10$  GeV, respectively. Our results are collected in Table 5.2.

## 5.2 Single-inclusive particle production

As an illustration of the predictive power of NNPDFPOL2.0, we now present predictions for the longitudinal double-spin asymmetries  $A_{LL}^h$  of single-inclusive particle production in polarised DIS and in proton-proton collisions. These asymmetries are defined, respectively, in Eq. (2) of [113] and in Eq. (17) of [30] as ratios of polarised to unpolarised cross sections with the same final-state particle. In the case of semi-inclusive DIS, we further approximate the longitudinal double-spin asymmetry with the virtual-photon-nucleon asymmetry  $A_1^h$  (see Eq. (6) in [113]), which is the ratio between the polarised and unpolarised SIDIS structure functions.

We compute predictions for these processes at NLO accuracy in perturbative QCD. For single-hadron production in DIS, NNLO corrections to the matrix elements are known [20–22], whereas they are not in proton-proton collisions. Because our aim is solely to demonstrate an application of NNPDFPOL2.0, and not to perform a detailed phenomenological study, we stick to NLO matrix elements in both cases. Theoretical predictions require knowledge of FFs, in particular for separate quark and anti-quark flavours and for the gluon. Such knowledge is lacking in available NNFF sets [114, 115] because of the limited amount of measurements included in the corresponding determinations. We therefore select FFs from the MAPFF1.0 set [116, 117]. These were determined from a comprehensive analysis of single-hadron production measurements in electron-positron annihilation and in DIS with a methodology similar to that used for NNPDFPOL2.0. We use the NNPDF4.0 set for the required initial-state unpolarised proton PDFs. In the case of single-hadron production in polarised DIS, we use a piece of software that we have developed for the purpose of this study, whereas we use the code of [118] in the case of single-hadron production in polarised proton-proton collisions.

In Fig. 5.2, we compare our predictions for negatively charged pion and kaon production in polarised semi-inclusive electron-deuteron DIS to measurements performed by the HERMES experiment [113] with a beam energy of 27.6 GeV. The asymmetry  $A_1^h$  is reported as a function of  $z$ , the fraction of the virtual-photon energy carried by the observed final-state hadron, in three bins of  $x$ . In Fig. 5.3, we compare our predictions for neutral pion production in polarised proton-proton collisions by the PHENIX [119] and STAR [120] experiments at a centre-of-mass energy of 200 GeV. The asymmetry  $A_{LL}^h$  is reported as a function of the transverse momentum  $p_T$  of the neutral pion. In both Fig. 5.2 and Fig. 5.3, matrix elements are accurate to NLO. Error bands correspond to one-sigma uncertainties computed from the NNPDFPOL2.0 NLO or NNLO polarised PDF sets; the unpolarised PDF and the FF are fixed to the central value of the NNPDF4.0 and MAPFF1.0 NLO sets.

Our predictions are always in good agreement with the data within experimental uncertainties. These remain rather larger than the uncertainty on the prediction, therefore one may question whether these additional data can provide any additional constraint on the polarised PDFs. In this respect, we make two considerations. First, the longitudinal double-spin asymmetry measured by PHENIX may actually have some impact on the polarised gluon PDF, thanks to the precision of the small- $p_T$  data points. Second, the uncertainty displayed in Figs. 5.2 and 5.3, as mentioned, only represents the polarised PDF uncertainty. On top of this, there are MHO uncertainties and uncertainties coming from the PDF and FF. This last uncertainty, in particular, may be non-negligible. The results displayed in Figs. 5.2 and 5.3 may therefore have a simultaneous impact on polarised PDFs and FFs, the assessment of which requires a determination of FFs beyond the scope of this work.

## 6 Summary and delivery

In this work, we have presented NNPDFPOL2.0, a new set of polarised PDFs of the proton accurate at LO, NLO, and NNLO in the strong coupling expansion that systematically incorporates, for the first time, MHOUs. This determination is based on legacy measurements of polarised structure functions in inclusive DIS and of longitudinally polarised spin asymmetries for the production of  $W$  bosons, single-inclusive jets, and di-jet in polarised proton-proton collisions. These measurements amount to most of all of those that are currently available, and that are relevant to constrain polarised PDFs. The only notable exception being measurements whose analysis requires an explicit knowledge of FFs, namely those for single-hadron production in polarised DIS and proton-proton collisions. NNPDFPOL2.0 makes use of a state-of-the-art machine learning methodology, that allows not only for the reduction of parametrisation bias, through a neural network parametrisation, but also for the selection of the optimal fitting model, through an automated hyperparameter scan.

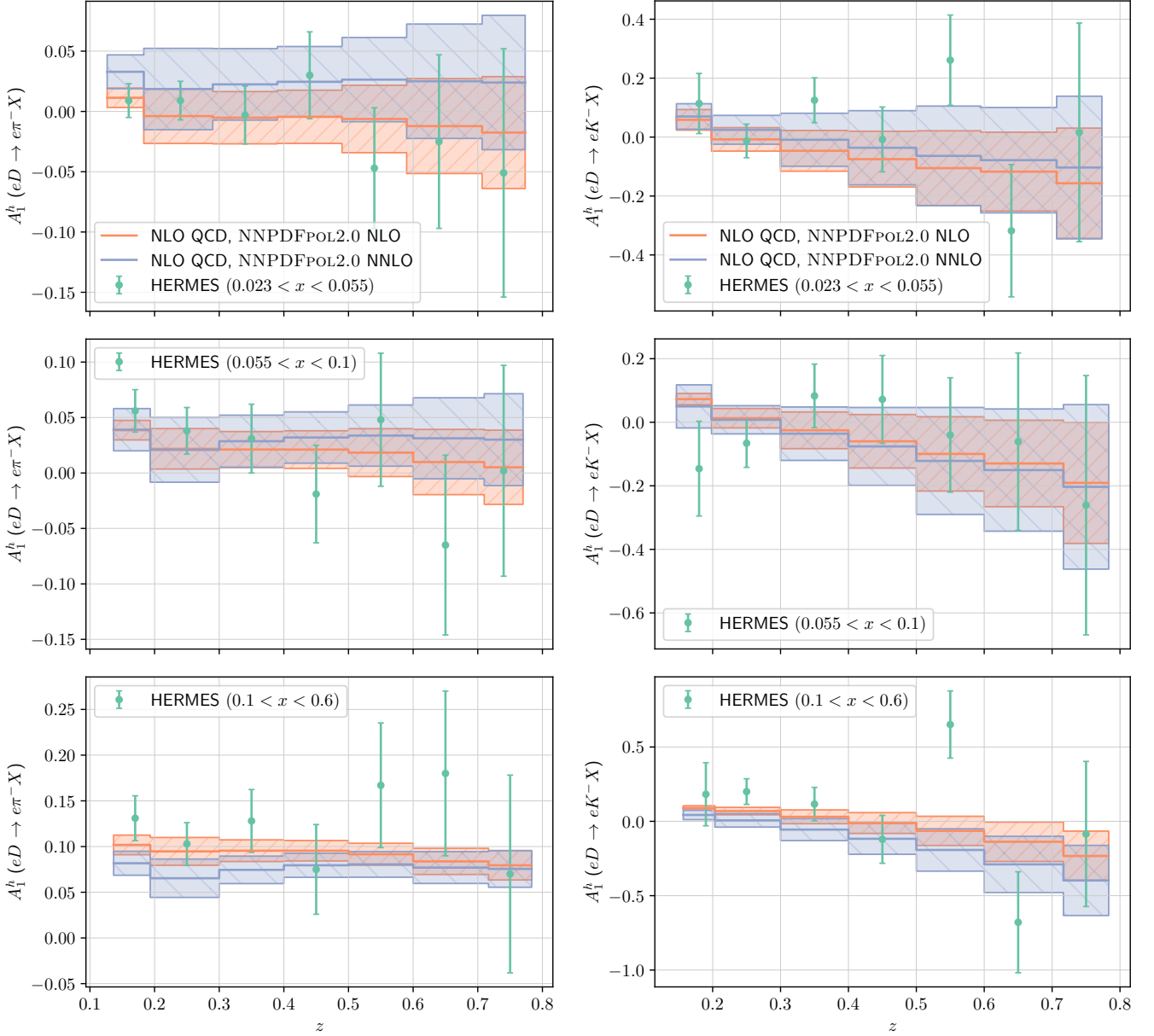


**Figure 5.2.** Comparison between experimental measurements of the spin asymmetry  $A_1^h$  for the production of single-inclusive negative pions (left) and kaons (right) in polarised semi-inclusive DIS and the corresponding theoretical predictions. Experimental data are displayed as a function of  $z$  for three  $x$  bins of the HERMES experiment [113], see text for details. Theoretical predictions are obtained with matrix elements accurate to NLO and with NNPDFPOL2.0 NLO or NNLO polarised PDF sets; the unpolarised PDF and the FF are fixed to the central value of the NNPDF4.0 and MAPFF1.0 NLO sets. Therefore, error bands only account for one-sigma polarised PDF uncertainties.

Our results indicate that NNPDFPOL2.0 is a reliable determination of polarised PDFs. In particular, it displays an excellent fit quality for all of the considered data sets, a remarkable perturbative stability upon inclusion of higher-order corrections or MHOUs, and a good consistency upon relaxation of the positivity constraint or variations of the input data set. Two outcomes are outstanding. First, the determination exhibits less sensitivity to the perturbative accuracy than its unpolarised counterpart: the impact of NNLO perturbative corrections on the fit quality is almost immaterial, and the impact of MHOUs is moderate at LO and NLO and very limited at NNLO. We therefore conclude that, with the current data set, theoretical framework, and methodology, the perturbative expansion has converged. Second, the determination confirms the relevance of the RHIC data in constraining key aspects of the polarised PDFs. Measurements of longitudinal spin asymmetries for single-inclusive jet and di-jet production in polarised proton-proton collisions are such that the polarised gluon PDF is conclusively positive, albeit only in the  $x$  region constrained by the data,  $x \gtrsim 0.02$ . This result is largely independent of the positivity constraint and from the other data sets included in the fit. Measurements of longitudinal spin asymmetries for  $W$ -boson production in



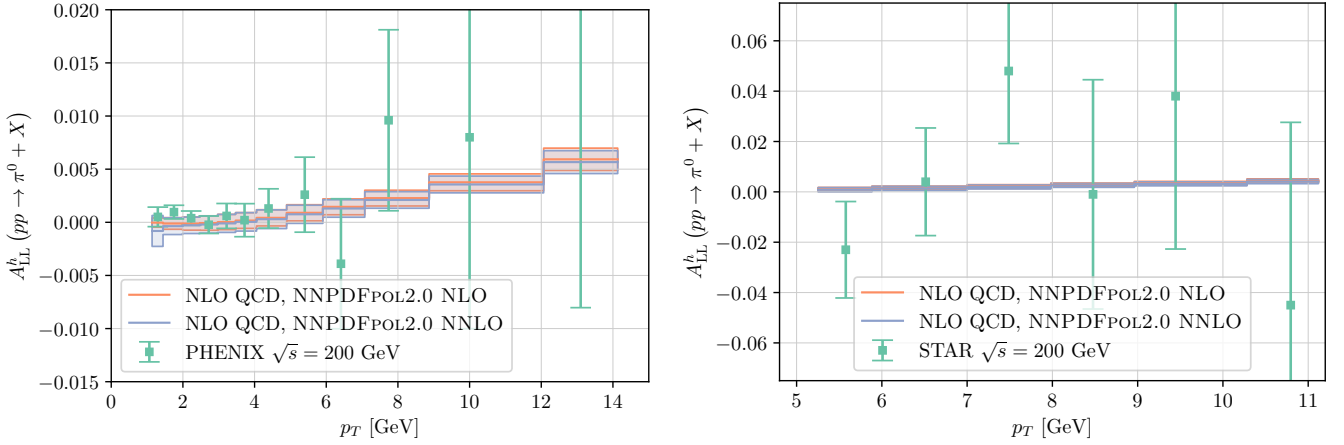


**Figure 5.3.** Comparison between experimental measurements of the double-spin asymmetry  $A_{LL}^h$  for the production of single-inclusive neutral pions in polarised proton-proton collisions and the corresponding theoretical predictions. Experimental data are from the PHENIX (left) [119] and STAR (right) [120] experiments. Theoretical predictions are obtained with matrix elements accurate to NLO and with NNPDFPOL2.0 NLO or NNLO polarised PDF sets; the unpolarised PDF and the FF are fixed to the central value of the NNPDF4.0 and MAPFF1.0 NLO sets. Therefore, error bands only account for one-sigma polarised PDF uncertainties.

polarised proton-proton collisions confirm that the difference between up and down antiquark PDF is positive, and actually a little larger than what was found in NNPDFPOL1.1. The NNPDFPOL2.0 PDFs are compatible with other recent NNLO polarised PDF determinations, in particular with MAPPDFPOL1.0 and BDSSV24.

From a phenomenological perspective, we have revisited the spin content of the proton, showing that the fraction of proton spin carried by gluons and quarks remains consistent with NNPDFPOL1.1, though it is still subject to large uncertainties coming from the small- $x$  kinematic region. We have also demonstrated the applicability of NNPDFPOL2.0 in computing predictions for single-inclusive hadron production in polarised DIS and proton-proton collisions, showing good agreement with the available experimental data. Our work could naturally be extended to incorporate these measurements in a fit. However, this task would first require to develop a consistent methodological framework to determine FFs. This is a non-trivial endeavour which requires combining PDFs and FFs, with their respective perturbative evolution, and to account for their possible interplay in physical observables that depend on both of them. In principle, a simultaneous fit to both should be performed to quantify this interplay. This exercise will be part of future work.

Together with the NNPDF4.0 parton sets [33, 40, 94], NNPDFPOL2.0 completes a global set of unpolarised and polarised PDFs determined with a consistent methodology, including consistent positivity constraints. These parton sets provide altogether a baseline for the upcoming physics program of the EIC. The LO, NLO, and NNLO NNPDFPOL2.0 PDF sets without and with MHOUs are made publicly available in the LHAPDF format [52, 53] as ensembles of both 1000 and 100 Monte Carlo replicas, the latter being obtained from compression of the former with the algorithm developed in [54]. These sets are also available through the NNPDF web page [121]. The open-source NNPDF software [56] has been extended to include the input and tools needed to reproduce the NNPDFPOL2.0 sets presented here.

The list of available PDF sets, all with a fixed value of the strong coupling  $\alpha_s(m_Z) = 0.118$ , is as follows.

- Baseline LO, NLO, and NNLO PDF sets without MHOUs, 1000 Monte Carlo replicas

```

NNPDFpol20_lo_as_01180_1000
NNPDFpol20_nlo_as_01180_1000
NNPDFpol20_nnlo_as_01180_1000

```

- Baseline LO, NLO, and NNLO PDF sets with MHOUs, 1000 Monte Carlo replicas

```

NNPDFpol20_lo_as_01180_mhou_1000
NNPDFpol20_nlo_as_01180_mhou_1000
NNPDFpol20_nnlo_as_01180_mhou_1000

```

- Compressed LO, NLO, and NNLO PDF sets without MHOUs, 100 Monte Carlo replicas

```

NNPDFpol20_lo_as_01180
NNPDFpol20_nlo_as_01180
NNPDFpol20_nnlo_as_01180

```

- Compressed LO, NLO, and NNLO PDF sets with MHOUs, 100 Monte Carlo replicas

```

NNPDFpol20_lo_as_01180_mhou
NNPDFpol20_nlo_as_01180_mhou
NNPDFpol20_nnlo_as_01180_mhou

```

## Acknowledgements

Special thanks are due to Christopher Schwan for his continuous and friendly support with PINEAPPL. We thank Elke Aschenauer for clarifications on the usage of the STAR data, Daniel de Florian and Werner Vogelsang for providing us with the piece of software of [88, 89], Frank Petriello and Hai Tao Li for providing us with the modified version of MCFM developed in [23], and all the members of the NNPDF collaboration for interesting discussions.

F.H. is supported by the Academy of Finland project 358090 and is funded as a part of the Center of Excellence in Quark Matter of the Academy of Finland, project 346326. E.R.N. is supported by the Italian Ministry of University and Research (MUR) through the “Rita Levi-Montalcini” Program. G.M. and J.R. are partially supported by NWO, the Dutch Research Council. J.R. and T.R.R. are supported by an ASDI grant from the Netherlands eScience Center (NLLeSC).

## A Benchmark of the PINEAPPL grids

As discussed in Section 2, we compute theoretical predictions corresponding to the data included in the NNPDFPOL2.0 fits by convolving PDFs with pre-computed PDF-independent fast interpolation grids. We compute these grids in the PINEAPPL format [46], starting from various pieces of external software, that were typically developed to compute cross sections of a specific production process. Making these pieces of software able to generate PINEAPPL grids requires nontrivial modifications, therefore one may wonder whether these introduce a loss of accuracy in the computation of physical observables. In this appendix, we show, for the specific case of  $W$ -boson production in polarised proton-proton collisions, as implemented in the modified version of MCFM [23], that this is not the case.

To this purpose, we perform the following benchmark. We compute the longitudinal double-spin asymmetry in two ways. First, by running the unmodified version of the code of [23]. In this case, the convolution between PDFs and matrix elements is performed at every step of the Monte Carlo integration. Second, by convolving PDFs with the PINEAPPL grids generated from a modified version of the same code. In this case, PDFs are effectively multiplied by the weights stored in the grids only once. The result obtained with the latter method is equivalent to the result obtained with the former method, within Monte Carlo and interpolation uncertainties, only if the required modification to the code in [23] are properly implemented. Given that the accuracy of the integration and of the interpolation does not depend on the choice of the renormalisation and factorisation scales, it is sufficient to check the results obtained with the central scale.

In Fig. A.1, we compare the results obtained from the two aforementioned methods, normalised to the former. Specifically, we compare the Monte Carlo integration error of the first method with the interpolation error of the second method. We observe that Monte Carlo errors are below one permil, except for the leftmost bin in the positron pseudorapidity of the  $W^+$  boson, where they are of the order of 1.5%. Interpolation uncertainties are smaller than that: indeed the difference between the two central values is of the order of 0.5% at most, with very negligible fluctuations across different pseudorapidity bins. We therefore conclude that the two methods are equivalent, and, in particular, that the generation of PINEAPPL grids does not result in any accuracy loss.

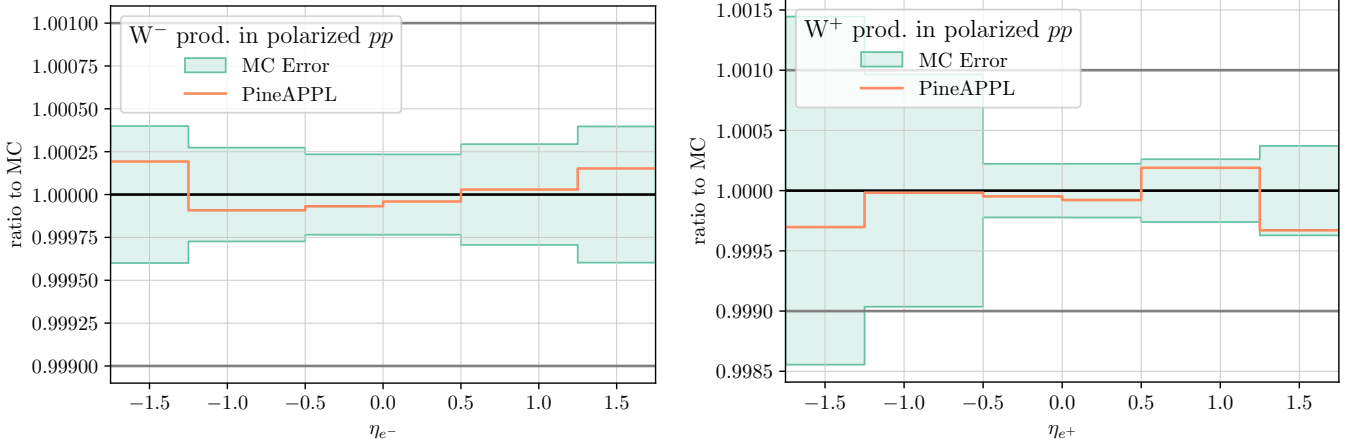


**Figure A.1.** Predictions of the longitudinal spin asymmetry for  $W^-$  (left) and  $W^+$  (right) boson production in polarised proton-proton collisions obtained from the code of [23] or from convolution of PDFs with PINEAPPL grids generated from a modified version of the same code. The results are normalised to the former. The band corresponds to Monte Carlo uncertainties due to numerical integration performed with the code of [23].

## References

- [1] J. J. Ethier and E. R. Nocera, “Parton Distributions in Nucleons and Nuclei,” [Ann. Rev. Nucl. Part. Sci.](#) **70** (2020) 43–76, [arXiv:2001.07722 \[hep-ph\]](#).
- [2] M. Anselmino, A. Efremov, and E. Leader, “The Theory and phenomenology of polarized deep inelastic scattering,” [Phys. Rept.](#) **261** (1995) 1–124, [arXiv:hep-ph/9501369](#). [Erratum: Phys.Rept. 281, 399–400 (1997)].
- [3] X. Ji, F. Yuan, and Y. Zhao, “What we know and what we don’t know about the proton spin after 30 years,” [Nature Rev. Phys.](#) **3** no. 1, (2021) 27–38, [arXiv:2009.01291 \[hep-ph\]](#).
- [4] R. Abdul Khalek et al., “Science Requirements and Detector Concepts for the Electron-Ion Collider: EIC Yellow Report,” [Nucl. Phys. A](#) **1026** (2022) 122447, [arXiv:2103.05419 \[physics.ins-det\]](#).
- [5] R. Abdul Khalek et al., “Snowmass 2021 White Paper: Electron Ion Collider for High Energy Physics,” [arXiv:2203.13199 \[hep-ph\]](#).
- [6] J. C. Collins, D. E. Soper, and G. F. Sterman, “Factorization of Hard Processes in QCD,” [Adv. Ser. Direct. High Energy Phys.](#) **5** (1989) 1–91, [arXiv:hep-ph/0409313](#).
- [7] E. B. Zijlstra and W. L. van Neerven, “Order- $\alpha_s^2$  corrections to the polarized structure function  $g_1(x, Q^2)$ ,” [Nucl. Phys. B](#) **417** (1994) 61–100. [Erratum: Nucl.Phys.B 426, 245 (1994), Erratum: Nucl.Phys.B 773, 105–106 (2007), Erratum: Nucl.Phys.B 501, 599–599 (1997)].
- [8] J. Blümlein, P. Marquard, C. Schneider, and K. Schönwald, “The massless three-loop Wilson coefficients for the deep-inelastic structure functions  $F_2$ ,  $F_L$ ,  $xF_3$  and  $g_1$ ,” [JHEP](#) **11** (2022) 156, [arXiv:2208.14325 \[hep-ph\]](#).
- [9] F. Hekhorn and M. Stratmann, “Next-to-Leading Order QCD Corrections to Inclusive Heavy-Flavor Production in Polarized Deep-Inelastic Scattering,” [Phys. Rev. D](#) **98** no. 1, (2018) 014018, [arXiv:1805.09026 \[hep-ph\]](#).
- [10] A. Behring, J. Blümlein, A. De Freitas, A. von Manteuffel, and C. Schneider, “The 3-Loop Non-Singlet Heavy Flavor Contributions to the Structure Function  $g_1(x, Q^2)$  at Large Momentum Transfer,” [Nucl. Phys. B](#) **897** (2015) 612–644, [arXiv:1504.08217 \[hep-ph\]](#).
- [11] J. Ablinger, A. Behring, J. Blümlein, A. De Freitas, A. von Manteuffel, C. Schneider, and K. Schönwald, “The three-loop single mass polarized pure singlet operator matrix element,” [Nucl. Phys. B](#) **953** (2020) 114945, [arXiv:1912.02536 \[hep-ph\]](#).

- [12] A. Behring, J. Blümlein, A. De Freitas, A. von Manteuffel, K. Schönwald, and C. Schneider, “The polarized transition matrix element  $A_{gq}(N)$  of the variable flavor number scheme at  $O(\alpha_s^3)$ ,” [\*Nucl. Phys. B\* \*\*964\*\* \(2021\) 115331](#), [arXiv:2101.05733 \[hep-ph\]](#).
- [13] J. Blümlein, A. De Freitas, M. Saragnese, C. Schneider, and K. Schönwald, “Logarithmic contributions to the polarized  $O(\alpha_s^3)$  asymptotic massive Wilson coefficients and operator matrix elements in deeply inelastic scattering,” [\*Phys. Rev. D\* \*\*104\*\* no. 3, \(2021\) 034030](#), [arXiv:2105.09572 \[hep-ph\]](#).
- [14] I. Bierenbaum, J. Blümlein, A. De Freitas, A. Goedicke, S. Klein, and K. Schönwald, “ $O(\alpha_s^2)$  polarized heavy flavor corrections to deep-inelastic scattering at  $Q^2 \gg m^2$ ,” [\*Nucl. Phys. B\* \*\*988\*\* \(2023\) 116114](#), [arXiv:2211.15337 \[hep-ph\]](#).
- [15] J. Ablinger, A. Behring, J. Blümlein, A. De Freitas, A. Goedicke, A. von Manteuffel, C. Schneider, and K. Schönwald, “The unpolarized and polarized single-mass three-loop heavy flavor operator matrix elements  $A_{gg,Q}$  and  $\Delta A_{gg,Q}$ ,” [\*JHEP\* \*\*12\*\* \(2022\) 134](#), [arXiv:2211.05462 \[hep-ph\]](#).
- [16] J. Ablinger, A. Behring, J. Blümlein, A. De Freitas, A. von Manteuffel, C. Schneider, and K. Schönwald, “The first-order factorizable contributions to the three-loop massive operator matrix elements  $A_{Qg(3)}$  and  $\Delta A_{Qg(3)}$ ,” [\*Nucl. Phys. B\* \*\*999\*\* \(2024\) 116427](#), [arXiv:2311.00644 \[hep-ph\]](#).
- [17] J. Ablinger, A. Behring, J. Blümlein, A. De Freitas, A. von Manteuffel, C. Schneider, and K. Schönwald, “The non-first-order-factorizable contributions to the three-loop single-mass operator matrix elements  $A_{Qg(3)}$  and  $\Delta A_{Qg(3)}$ ,” [\*Phys. Lett. B\* \*\*854\*\* \(2024\) 138713](#), [arXiv:2403.00513 \[hep-ph\]](#).
- [18] I. Borsa, D. de Florian, and I. Pedron, “The full set of polarized deep inelastic scattering structure functions at NNLO accuracy,” [\*Eur. Phys. J. C\* \*\*82\*\* no. 12, \(2022\) 1167](#), [arXiv:2210.12014 \[hep-ph\]](#).
- [19] M. Abele, D. de Florian, and W. Vogelsang, “Approximate NNLO QCD corrections to semi-inclusive DIS,” [\*Phys. Rev. D\* \*\*104\*\* no. 9, \(2021\) 094046](#), [arXiv:2109.00847 \[hep-ph\]](#).
- [20] L. Bonino, T. Gehrmann, M. Löchner, K. Schönwald, and G. Stagnitto, “Polarized Semi-Inclusive Deep-Inelastic Scattering at Next-to-Next-to-Leading Order in QCD,” [\*Phys. Rev. Lett.\* \*\*133\*\* no. 21, \(2024\) 211904](#), [arXiv:2404.08597 \[hep-ph\]](#).
- [21] S. Goyal, R. N. Lee, S.-O. Moch, V. Pathak, N. Rana, and V. Ravindran, “Next-to-Next-to-Leading Order QCD Corrections to Polarized Semi-Inclusive Deep-Inelastic Scattering,” [\*Phys. Rev. Lett.\* \*\*133\*\* \(2024\) 211905](#), [arXiv:2404.09959 \[hep-ph\]](#).
- [22] S. Goyal, R. N. Lee, S.-O. Moch, V. Pathak, N. Rana, and V. Ravindran, “NNLO QCD corrections to unpolarized and polarized SIDIS,” [arXiv:2412.19309 \[hep-ph\]](#).
- [23] R. Boughezal, H. T. Li, and F. Petriello, “ $W$ -boson production in polarized proton-proton collisions at RHIC through next-to-next-to-leading order in perturbative QCD,” [\*Phys. Lett. B\* \*\*817\*\* \(2021\) 136333](#), [arXiv:2101.02214 \[hep-ph\]](#).
- [24] S. Moch, J. A. M. Vermaseren, and A. Vogt, “The Three-Loop Splitting Functions in QCD: The Helicity-Dependent Case,” [\*Nucl. Phys. B\* \*\*889\*\* \(2014\) 351–400](#), [arXiv:1409.5131 \[hep-ph\]](#).
- [25] S. Moch, J. A. M. Vermaseren, and A. Vogt, “On  $\gamma_5$  in higher-order QCD calculations and the NNLO evolution of the polarized valence distribution,” [\*Phys. Lett. B\* \*\*748\*\* \(2015\) 432–438](#), [arXiv:1506.04517 \[hep-ph\]](#).
- [26] J. Blümlein, P. Marquard, C. Schneider, and K. Schönwald, “The three-loop unpolarized and polarized non-singlet anomalous dimensions from off shell operator matrix elements,” [\*Nucl. Phys. B\* \*\*971\*\* \(2021\) 115542](#), [arXiv:2107.06267 \[hep-ph\]](#).

- [27] J. Blümlein, P. Marquard, C. Schneider, and K. Schönwald, “The three-loop polarized singlet anomalous dimensions from off-shell operator matrix elements,” *JHEP* **01** (2022) 193, [arXiv:2111.12401 \[hep-ph\]](#).
- [28] F. Taghavi-Shahri, H. Khanpour, S. Atashbar Tehrani, and Z. Alizadeh Yazdi, “Next-to-next-to-leading order QCD analysis of spin-dependent parton distribution functions and their uncertainties: Jacobi polynomials approach,” *Phys. Rev. D* **93** no. 11, (2016) 114024, [arXiv:1603.03157 \[hep-ph\]](#).
- [29] D. de Florian, R. Sassot, M. Stratmann, and W. Vogelsang, “Evidence for polarization of gluons in the proton,” *Phys. Rev. Lett.* **113** no. 1, (2014) 012001, [arXiv:1404.4293 \[hep-ph\]](#).
- [30] **NNPDF** Collaboration, E. R. Nocera, R. D. Ball, S. Forte, G. Ridolfi, and J. Rojo, “A first unbiased global determination of polarized PDFs and their uncertainties,” *Nucl. Phys. B* **887** (2014) 276–308, [arXiv:1406.5539 \[hep-ph\]](#).
- [31] **MAP** Collaboration, V. Bertone, A. Chiefa, and E. R. Nocera, “Helicity-dependent parton distribution functions at next-to-next-to-leading order accuracy from inclusive and semi-inclusive deep-inelastic scattering data,” [arXiv:2404.04712 \[hep-ph\]](#).
- [32] I. Borsa, M. Stratmann, W. Vogelsang, D. de Florian, and R. Sassot, “Next-to-Next-to-Leading Order Global Analysis of Polarized Parton Distribution Functions,” *Phys. Rev. Lett.* **133** no. 15, (2024) 151901, [arXiv:2407.11635 \[hep-ph\]](#).
- [33] **NNPDF** Collaboration, R. D. Ball et al., “The path to proton structure at 1% accuracy,” *Eur. Phys. J. C* **82** no. 5, (2022) 428, [arXiv:2109.02653 \[hep-ph\]](#).
- [34] E. R. Nocera, “Constraints on polarized parton distributions from open charm and W production data,” *PoS DIS2013* (2013) 211, [arXiv:1307.0146 \[hep-ph\]](#).
- [35] S. Forte, E. Laenen, P. Nason, and J. Rojo, “Heavy quarks in deep-inelastic scattering,” *Nucl. Phys. B* **834** (2010) 116–162, [arXiv:1001.2312 \[hep-ph\]](#).
- [36] F. Hekhorn, G. Magni, E. R. Nocera, T. R. Rabemananjara, J. Rojo, A. Schaus, and R. Stegeman, “Heavy quarks in polarised deep-inelastic scattering at the electron-ion collider,” *Eur. Phys. J. C* **84** no. 2, (2024) 189, [arXiv:2401.10127 \[hep-ph\]](#).
- [37] A. Barontini, A. Candido, F. Hekhorn, G. Magni, and R. Stegeman, “An FONLL prescription with coexisting flavor number PDFs,” *JHEP* **10** (2024) 004, [arXiv:2408.07383 \[hep-ph\]](#).
- [38] **NNPDF** Collaboration, R. Abdul Khalek et al., “A first determination of parton distributions with theoretical uncertainties,” *Eur. Phys. J. C* (2019) 79:838, [arXiv:1905.04311 \[hep-ph\]](#).
- [39] **NNPDF** Collaboration, R. Abdul Khalek et al., “Parton Distributions with Theory Uncertainties: General Formalism and First Phenomenological Studies,” *Eur. Phys. J. C* **79** no. 11, (2019) 931, [arXiv:1906.10698 \[hep-ph\]](#).
- [40] **NNPDF** Collaboration, R. D. Ball et al., “Determination of the theory uncertainties from missing higher orders on NNLO parton distributions with percent accuracy,” *Eur. Phys. J. C* **84** no. 5, (2024) 517, [arXiv:2401.10319 \[hep-ph\]](#).
- [41] A. Barontini, A. Candido, J. M. Cruz-Martinez, F. Hekhorn, and C. Schwan, “Pipeline: Industrialization of high-energy theory predictions,” *Comput. Phys. Commun.* **297** (2024) 109061, [arXiv:2302.12124 \[hep-ph\]](#).
- [42] A. Candido, F. Hekhorn, and G. Magni, “EKO: evolution kernel operators,” *Eur. Phys. J. C* **82** no. 10, (2022) 976, [arXiv:2202.02338 \[hep-ph\]](#).
- [43] A. Candido, F. Hekhorn, and G. Magni, “N3pdf/eko: Paper,” Mar., 2022. <https://doi.org/10.5281/zenodo.6340153>.

- [44] A. Candido, F. Hekhorn, G. Magni, T. R. Rabemananjara, and R. Stegeman, “Yadism: yet another deep-inelastic scattering module,” *Eur. Phys. J. C* **84** no. 7, (2024) 698, [arXiv:2401.15187 \[hep-ph\]](#).
- [45] A. Candido, F. Hekhorn, and G. Magni, “Nnpdf/yadism: Nc polarized structure functions up to mlo,” June, 2023. <https://doi.org/10.5281/zenodo.8066034>.
- [46] S. Carrazza, E. R. Nocera, C. Schwan, and M. Zaro, “PineAPPL: combining EW and QCD corrections for fast evaluation of LHC processes,” *JHEP* **12** (2020) 108, [arXiv:2008.12789 \[hep-ph\]](#).
- [47] C. Schwan, A. Candido, F. Hekhorn, S. Carrazza, T. Rabemananjara, T. Sharma, A. Barontini, J. Wissmann, and J. M. Cruz-Martinez, “Nnpdf/pineappl: v0.8.2,” July, 2024. <https://doi.org/10.5281/zenodo.12795745>.
- [48] S. Carrazza and J. Cruz-Martinez, “Towards a new generation of parton densities with deep learning models,” *Eur. Phys. J. C* **79** no. 8, (2019) 676, [arXiv:1907.05075 \[hep-ph\]](#).
- [49] J. Cruz-Martinez, A. Jansen, G. van Oord, T. R. Rabemananjara, C. M. R. Rocha, J. Rojo, and R. Stegeman, “Hyperparameter Optimisation in Deep Learning from Ensemble Methods: Applications to Proton Structure,” [arXiv:2410.16248 \[hep-ph\]](#).
- [50] **NNPDF** Collaboration, R. D. Ball, V. Bertone, F. Cerutti, L. Del Debbio, S. Forte, A. Guffanti, J. I. Latorre, J. Rojo, and M. Ubiali, “Reweighting NNPDFs: the W lepton asymmetry,” *Nucl. Phys. B* **849** (2011) 112–143, [arXiv:1012.0836 \[hep-ph\]](#). [Erratum: *Nucl.Phys.B* 854, 926–927 (2012), Erratum: *Nucl.Phys.B* 855, 927–928 (2012)].
- [51] R. D. Ball, V. Bertone, F. Cerutti, L. Del Debbio, S. Forte, et al., “Reweighting and Unweighting of Parton Distributions and the LHC W lepton asymmetry data,” *Nucl.Phys.* **B855** (2012) 608–638, [arXiv:1108.1758 \[hep-ph\]](#).
- [52] A. Buckley, J. Ferrando, S. Lloyd, K. Nordström, B. Page, M. Rüfenacht, M. Schönherr, and G. Watt, “LHAPDF6: parton density access in the LHC precision era,” *Eur. Phys. J. C* **75** (2015) 132, [arXiv:1412.7420 \[hep-ph\]](#).
- [53] <https://www.lhapdf.org/>.
- [54] S. Carrazza, J. M. Cruz-Martinez, and T. R. Rabemananjara, “Compressing PDF sets using generative adversarial networks,” *Eur. Phys. J. C* **81** no. 6, (2021) 530, [arXiv:2104.04535 \[hep-ph\]](#).
- [55] T. R. Rabemananjara, J. M. Cruz-Martinez, and S. Carrazza, “N3pdf/pycompressor: pycompressor v1.1.0,” 2020. <https://doi.org/10.5281/zenodo.4616385>.
- [56] **NNPDF** Collaboration, R. D. Ball et al., “An open-source machine learning framework for global analyses of parton distributions,” *Eur. Phys. J. C* **81** no. 10, (2021) 958, [arXiv:2109.02671 \[hep-ph\]](#).
- [57] **NNPDF** Collaboration, R. D. Ball, S. Forte, A. Guffanti, E. R. Nocera, G. Ridolfi, and J. Rojo, “Unbiased determination of polarized parton distributions and their uncertainties,” *Nucl. Phys. B* **874** (2013) 36–84, [arXiv:1303.7236 \[hep-ph\]](#).
- [58] E. R. Nocera, [Unbiased spin-dependent Parton Distribution Functions](#). PhD thesis, Milan U., 2014. [arXiv:1403.0440 \[hep-ph\]](#).
- [59] **European Muon** Collaboration, J. Ashman et al., “An Investigation of the Spin Structure of the Proton in Deep Inelastic Scattering of Polarized Muons on Polarized Protons,” *Nucl. Phys. B* **328** (1989) 1.

- [60] **Spin Muon** Collaboration, B. Adeva *et al.*, “Spin asymmetries  $A(1)$  and structure functions  $g_1$  of the proton and the deuteron from polarized high-energy muon scattering,” [Phys. Rev. D \*\*58\*\* \(1998\) 112001](#).
- [61] **Spin Muon** Collaboration, B. Adeva *et al.*, “Spin asymmetries  $A(1)$  of the proton and the deuteron in the low  $x$  and low  $Q^2$  region from polarized high-energy muon scattering,” [Phys. Rev. D \*\*60\*\* \(1999\) 072004](#). [Erratum: Phys.Rev.D 62, 079902 (2000)].
- [62] **COMPASS** Collaboration, C. Adolph *et al.*, “The spin structure function  $g_1^p$  of the proton and a test of the Bjorken sum rule,” [Phys. Lett. B \*\*753\*\* \(2016\) 18–28](#), [arXiv:1503.08935 \[hep-ex\]](#).
- [63] **COMPASS** Collaboration, C. Adolph *et al.*, “Final COMPASS results on the deuteron spin-dependent structure function  $g_1^d$  and the Bjorken sum rule,” [Phys. Lett. B \*\*769\*\* \(2017\) 34–41](#), [arXiv:1612.00620 \[hep-ex\]](#).
- [64] **E142** Collaboration, P. L. Anthony *et al.*, “Deep inelastic scattering of polarized electrons by polarized He-3 and the study of the neutron spin structure,” [Phys. Rev. D \*\*54\*\* \(1996\) 6620–6650](#), [arXiv:hep-ex/9610007](#).
- [65] **E143** Collaboration, K. Abe *et al.*, “Measurements of the proton and deuteron spin structure functions  $g(1)$  and  $g(2)$ ,” [Phys. Rev. D \*\*58\*\* \(1998\) 112003](#), [arXiv:hep-ph/9802357](#).
- [66] **E154** Collaboration, K. Abe *et al.*, “Precision determination of the neutron spin structure function  $g_1(n)$ ,” [Phys. Rev. Lett. \*\*79\*\* \(1997\) 26–30](#), [arXiv:hep-ex/9705012](#).
- [67] **E155** Collaboration, P. L. Anthony *et al.*, “Measurements of the  $Q^2$  dependence of the proton and neutron spin structure functions  $g(1)^{*p}$  and  $g(1)^{*n}$ ,” [Phys. Lett. B \*\*493\*\* \(2000\) 19–28](#), [arXiv:hep-ph/0007248](#).
- [68] **HERMES** Collaboration, K. Ackerstaff *et al.*, “Measurement of the neutron spin structure function  $g_1(n)$  with a polarized He-3 internal target,” [Phys. Lett. B \*\*404\*\* \(1997\) 383–389](#), [arXiv:hep-ex/9703005](#).
- [69] **HERMES** Collaboration, A. Airapetian *et al.*, “Precise determination of the spin structure function  $g(1)$  of the proton, deuteron and neutron,” [Phys. Rev. D \*\*75\*\* \(2007\) 012007](#), [arXiv:hep-ex/0609039](#).
- [70] **Jefferson Lab Hall A** Collaboration, D. Flay *et al.*, “Measurements of  $d_2^n$  and  $A_1^n$ : Probing the neutron spin structure,” [Phys. Rev. D \*\*94\*\* no. 5, \(2016\) 052003](#), [arXiv:1603.03612 \[nucl-ex\]](#).
- [71] **Jefferson Lab E97-103** Collaboration, K. M. Kramer, “The Search for Higher Twist Effects in the Spin-Structure Functions of the Neutron,” [AIP Conf. Proc. \*\*675\*\* no. 1, \(2003\) 615–619](#).
- [72] **Jefferson Lab Hall A** Collaboration, X. Zheng *et al.*, “Precision measurement of the neutron spin asymmetries and spin-dependent structure functions in the valence quark region,” [Phys. Rev. C \*\*70\*\* \(2004\) 065207](#), [arXiv:nucl-ex/0405006](#).
- [73] **CLAS** Collaboration, Y. Prok *et al.*, “Precision measurements of  $g_1$  of the proton and the deuteron with 6 GeV electrons,” [Phys. Rev. C \*\*90\*\* no. 2, \(2014\) 025212](#), [arXiv:1404.6231 \[nucl-ex\]](#).
- [74] **CLAS** Collaboration, K. V. Dharmawardane *et al.*, “Measurement of the  $x$ - and  $Q^2$ -dependence of the asymmetry  $A(1)$  on the nucleon,” [Phys. Lett. B \*\*641\*\* \(2006\) 11–17](#), [arXiv:nucl-ex/0605028](#).
- [75] S. Wandzura and F. Wilczek, “Sum Rules for Spin Dependent Electroproduction: Test of Relativistic Constituent Quarks,” [Phys. Lett. B \*\*72\*\* \(1977\) 195–198](#).
- [76] R. D. Ball, E. R. Nocera, and R. L. Pearson, “Deuteron Uncertainties in the Determination of Proton PDFs,” [Eur. Phys. J. C \*\*81\*\* no. 1, \(2021\) 37](#), [arXiv:2011.00009 \[hep-ph\]](#).
- [77] **STAR** Collaboration, J. Adam *et al.*, “Measurement of the longitudinal spin asymmetries for weak boson production in proton-proton collisions at  $\sqrt{s} = 510$  GeV,” [Phys. Rev. D \*\*99\*\* no. 5, \(2019\) 051102](#), [arXiv:1812.04817 \[hep-ex\]](#).

- [78] **STAR** Collaboration, L. Adamczyk *et al.*, “Measurement of longitudinal spin asymmetries for weak boson production in polarized proton-proton collisions at RHIC,” [\*Phys. Rev. Lett.\* \*\*113\*\* \(2014\) 072301](#), [arXiv:1404.6880 \[nucl-ex\]](#).
- [79] **PHENIX** Collaboration, A. Adare *et al.*, “Measurement of parity-violating spin asymmetries in  $W^\pm$  production at midrapidity in longitudinally polarized  $p + p$  collisions,” [\*Phys. Rev. D\* \*\*93\*\* no. 5, \(2016\) 051103](#), [arXiv:1504.07451 \[hep-ex\]](#).
- [80] **PHENIX** Collaboration, A. Adare *et al.*, “Event Structure and Double Helicity Asymmetry in Jet Production from Polarized  $p + p$  Collisions at  $\sqrt{s} = 200$  GeV,” [\*Phys. Rev. D\* \*\*84\*\* \(2011\) 012006](#), [arXiv:1009.4921 \[hep-ex\]](#).
- [81] **STAR** Collaboration, L. Adamczyk *et al.*, “Longitudinal and transverse spin asymmetries for inclusive jet production at mid-rapidity in polarized  $p + p$  collisions at  $\sqrt{s} = 200$  GeV,” [\*Phys. Rev. D\* \*\*86\*\* \(2012\) 032006](#), [arXiv:1205.2735 \[nucl-ex\]](#).
- [82] **STAR** Collaboration, L. Adamczyk *et al.*, “Precision Measurement of the Longitudinal Double-spin Asymmetry for Inclusive Jet Production in Polarized Proton Collisions at  $\sqrt{s} = 200$  GeV,” [\*Phys. Rev. Lett.\* \*\*115\*\* no. 9, \(2015\) 092002](#), [arXiv:1405.5134 \[hep-ex\]](#).
- [83] **STAR** Collaboration, M. S. Abdallah *et al.*, “Longitudinal double-spin asymmetry for inclusive jet and dijet production in polarized proton collisions at  $\sqrt{s} = 200$  GeV,” [\*Phys. Rev. D\* \*\*103\*\* no. 9, \(2021\) L091103](#), [arXiv:2103.05571 \[hep-ex\]](#).
- [84] **STAR** Collaboration, J. Adam *et al.*, “Longitudinal double-spin asymmetry for inclusive jet and dijet production in pp collisions at  $\sqrt{s} = 510$  GeV,” [\*Phys. Rev. D\* \*\*100\*\* no. 5, \(2019\) 052005](#), [arXiv:1906.02740 \[hep-ex\]](#).
- [85] **STAR** Collaboration, M. S. Abdallah *et al.*, “Longitudinal double-spin asymmetry for inclusive jet and dijet production in polarized proton collisions at  $\sqrt{s} = 510$  GeV,” [\*Phys. Rev. D\* \*\*105\*\* no. 9, \(2022\) 092011](#), [arXiv:2110.11020 \[hep-ex\]](#).
- [86] **STAR** Collaboration, L. Adamczyk *et al.*, “Measurement of the cross section and longitudinal double-spin asymmetry for di-jet production in polarized  $pp$  collisions at  $\sqrt{s} = 200$  GeV,” [\*Phys. Rev. D\* \*\*95\*\* no. 7, \(2017\) 071103](#), [arXiv:1610.06616 \[hep-ex\]](#).
- [87] **STAR** Collaboration, J. Adam *et al.*, “Longitudinal double-spin asymmetries for dijet production at intermediate pseudorapidity in polarized  $pp$  collisions at  $\sqrt{s} = 200$  GeV,” [\*Phys. Rev. D\* \*\*98\*\* no. 3, \(2018\) 032011](#), [arXiv:1805.09742 \[hep-ex\]](#).
- [88] D. de Florian, S. Frixione, A. Signer, and W. Vogelsang, “Next-to-leading order jet cross-sections in polarized hadronic collisions,” [\*Nucl. Phys. B\* \*\*539\*\* \(1999\) 455–476](#), [arXiv:hep-ph/9808262](#).
- [89] B. Jager, M. Stratmann, and W. Vogelsang, “Single inclusive jet production in polarized  $pp$  collisions at  $O(\alpha_s^3)$ ,” [\*Phys. Rev. D\* \*\*70\*\* \(2004\) 034010](#), [arXiv:hep-ph/0404057](#).
- [90] A. Mukherjee and W. Vogelsang, “Jet production in (un)polarized pp collisions: dependence on jet algorithm,” [\*Phys. Rev. D\* \*\*86\*\* \(2012\) 094009](#), [arXiv:1209.1785 \[hep-ph\]](#). [Erratum: *Phys. Rev. D* **107**, 119901 (2023)].
- [91] E. Maguire, L. Heinrich, and G. Watt, “HEPData: a repository for high energy physics data,” [\*J. Phys. Conf. Ser.\* \*\*898\*\* no. 10, \(2017\) 102006](#), [arXiv:1704.05473 \[hep-ex\]](#).
- [92] R. D. Ball *et al.*, “Parton Distribution Benchmarking with LHC Data,” [\*JHEP\* \*\*04\*\* \(2013\) 125](#), [arXiv:1211.5142 \[hep-ph\]](#).
- [93] **NNPDF** Collaboration, R. D. Ball, L. Del Debbio, S. Forte, A. Guffanti, J. I. Latorre, J. Rojo, and M. Ubiali, “Fitting Parton Distribution Data with Multiplicative Normalization Uncertainties,” [\*JHEP\* \*\*05\*\* \(2010\) 075](#), [arXiv:0912.2276 \[hep-ph\]](#).



- [94] **NNPDF** Collaboration, R. D. Ball et al., “The path to N<sup>3</sup>LO parton distributions,” [\*Eur. Phys. J. C\* \*\*84\*\* no. 7, \(2024\) 659, \[arXiv:2402.18635 \\[hep-ph\\]\]\(#\)](#).
- [95] S. Catani, D. de Florian, G. Rodrigo, and W. Vogelsang, “Perturbative generation of a strange-quark asymmetry in the nucleon,” [\*Phys. Rev. Lett.\* \*\*93\*\* \(2004\) 152003, \[arXiv:hep-ph/0404240\]\(#\)](#).
- [96] **Particle Data Group** Collaboration, S. Navas et al., “Review of particle physics,” [\*Phys. Rev. D\* \*\*110\*\* no. 3, \(2024\) 030001](#).
- [97] R. Flores-Mendieta, E. E. Jenkins, and A. V. Manohar, “SU(3) symmetry breaking in hyperon semileptonic decays,” [\*Phys. Rev. D\* \*\*58\*\* \(1998\) 094028, \[arXiv:hep-ph/9805416\]\(#\)](#).
- [98] G. Altarelli, S. Forte, and G. Ridolfi, “On positivity of parton distributions,” [\*Nucl. Phys. B\* \*\*534\*\* \(1998\) 277–296, \[arXiv:hep-ph/9806345\]\(#\)](#).
- [99] D. de Florian, S. Forte, and W. Vogelsang, “Higgs production at RHIC and the positivity of the gluon helicity distribution,” [\*Phys. Rev. D\* \*\*109\*\* no. 7, \(2024\) 074007, \[arXiv:2401.10814 \\[hep-ph\\]\]\(#\)](#).
- [100] F. Hekhorn, “On the positivity of MSbar distributions,” in *58th Rencontres de Moriond on QCD and High Energy Interactions*. 5, 2024. [arXiv:2405.08643 \[hep-ph\]](#).
- [101] F. Chollet et al., “Keras.” <https://keras.io>, 2015.
- [102] M. Abadi, A. Agarwal, P. Barham, E. Brevdo, Z. Chen, C. Citro, G. S. Corrado, A. Davis, J. Dean, M. Devin, S. Ghemawat, I. Goodfellow, A. Harp, G. Irving, M. Isard, Y. Jia, R. Jozefowicz, L. Kaiser, M. Kudlur, J. Levenberg, D. Mané, R. Monga, S. Moore, D. Murray, C. Olah, M. Schuster, J. Shlens, B. Steiner, I. Sutskever, K. Talwar, P. Tucker, V. Vanhoucke, V. Vasudevan, F. Viégas, O. Vinyals, P. Warden, M. Wattenberg, M. Wicke, Y. Yu, and X. Zheng, “TensorFlow: Large-scale machine learning on heterogeneous systems,” 2015. <https://www.tensorflow.org/>. Software available from tensorflow.org.
- [103] J. Cruz-Martinez, S. Forte, and E. R. Nocera, “Future tests of parton distributions,” [\*Acta Phys. Polon. B\* \*\*52\*\* \(2021\) 243, \[arXiv:2103.08606 \\[hep-ph\\]\]\(#\)](#).
- [104] D. de Florian, R. Sassot, M. Stratmann, and W. Vogelsang, “Global Analysis of Helicity Parton Densities and Their Uncertainties,” [\*Phys. Rev. Lett.\* \*\*101\*\* \(2008\) 072001, \[arXiv:0804.0422 \\[hep-ph\\]\]\(#\)](#).
- [105] D. de Florian, R. Sassot, M. Stratmann, and W. Vogelsang, “Extraction of Spin-Dependent Parton Densities and Their Uncertainties,” [\*Phys. Rev. D\* \*\*80\*\* \(2009\) 034030, \[arXiv:0904.3821 \\[hep-ph\\]\]\(#\)](#).
- [106] **Jefferson Lab Angular Momentum (JAM)** Collaboration, Y. Zhou, N. Sato, and W. Melnitchouk, “How well do we know the gluon polarization in the proton?,” [\*Phys. Rev. D\* \*\*105\*\* no. 7, \(2022\) 074022, \[arXiv:2201.02075 \\[hep-ph\\]\]\(#\)](#).
- [107] **Jefferson Lab Angular Momentum, HadStruc** Collaboration, J. Karpie, R. M. Whitehill, W. Melnitchouk, C. Monahan, K. Orginos, J. W. Qiu, D. G. Richards, N. Sato, and S. Zafeiropoulos, “Gluon helicity from global analysis of experimental data and lattice QCD Ioffe time distributions,” [\*Phys. Rev. D\* \*\*109\*\* no. 3, \(2024\) 036031, \[arXiv:2310.18179 \\[hep-ph\\]\]\(#\)](#).
- [108] **JAM** Collaboration, N. T. Hunt-Smith, C. Cocuzza, W. Melnitchouk, N. Sato, A. W. Thomas, and M. J. White, “New Data-Driven Constraints on the Sign of Gluon Polarization in the Proton,” [\*Phys. Rev. Lett.\* \*\*133\*\* no. 16, \(2024\) 161901, \[arXiv:2403.08117 \\[hep-ph\\]\]\(#\)](#).
- [109] R. L. Jaffe and A. Manohar, “The  $g_1$  Problem: Fact and Fantasy on the Spin of the Proton,” [\*Nucl. Phys. B\* \*\*337\*\* \(1990\) 509–546](#).
- [110] D. Adamiak, H. Mäntysaari, and Y. Tawabutr, “Proton spin from small- $x$  with constraints from the valence quark model,” [arXiv:2502.16604 \[hep-ph\]](#).

- [111] H.-W. Lin *et al.*, “Parton distributions and lattice QCD calculations: a community white paper,” [Prog. Part. Nucl. Phys.](#) **100** (2018) 107–160, [arXiv:1711.07916 \[hep-ph\]](#).
- [112] M. Constantinou *et al.*, “Parton distributions and lattice-QCD calculations: Toward 3D structure,” [Prog. Part. Nucl. Phys.](#) **121** (2021) 103908, [arXiv:2006.08636 \[hep-ph\]](#).
- [113] **HERMES** Collaboration, A. Airapetian *et al.*, “Longitudinal double-spin asymmetries in semi-inclusive deep-inelastic scattering of electrons and positrons by protons and deuterons,” [Phys. Rev. D](#) **99** no. 11, (2019) 112001, [arXiv:1810.07054 \[hep-ex\]](#).
- [114] **NNPDF** Collaboration, V. Bertone, S. Carrazza, N. P. Hartland, E. R. Nocera, and J. Rojo, “A determination of the fragmentation functions of pions, kaons, and protons with faithful uncertainties,” [Eur. Phys. J. C](#) **77** no. 8, (2017) 516, [arXiv:1706.07049 \[hep-ph\]](#).
- [115] **NNPDF** Collaboration, V. Bertone, N. P. Hartland, E. R. Nocera, J. Rojo, and L. Rottoli, “Charged hadron fragmentation functions from collider data,” [Eur. Phys. J. C](#) **78** no. 8, (2018) 651, [arXiv:1807.03310 \[hep-ph\]](#). [Erratum: [Eur.Phys.J.C](#) 84, 155 (2024)].
- [116] **MAP (Multi-dimensional Analyses of Partonic distributions)** Collaboration, R. A. Khalek, V. Bertone, and E. R. Nocera, “Determination of unpolarized pion fragmentation functions using semi-inclusive deep-inelastic-scattering data,” [Phys. Rev. D](#) **104** no. 3, (2021) 034007, [arXiv:2105.08725 \[hep-ph\]](#).
- [117] **MAP (Multi-dimensional Analyses of Partonic distributions)** Collaboration, R. Abdul Khalek, V. Bertone, A. Khoudli, and E. R. Nocera, “Pion and kaon fragmentation functions at next-to-next-to-leading order,” [Phys. Lett. B](#) **834** (2022) 137456, [arXiv:2204.10331 \[hep-ph\]](#).
- [118] B. Jager, A. Schafer, M. Stratmann, and W. Vogelsang, “Next-to-leading order QCD corrections to high p(T) pion production in longitudinally polarized pp collisions,” [Phys. Rev. D](#) **67** (2003) 054005, [arXiv:hep-ph/0211007](#).
- [119] **PHENIX** Collaboration, A. Adare *et al.*, “Inclusive double-helicity asymmetries in neutral-pion and eta-meson production in  $\vec{p} + \vec{p}$  collisions at  $\sqrt{s} = 200$  GeV,” [Phys. Rev. D](#) **90** no. 1, (2014) 012007, [arXiv:1402.6296 \[hep-ex\]](#).
- [120] **STAR** Collaboration, J. Adam *et al.*, “Longitudinal Double-Spin Asymmetries for  $\pi^0$ s in the Forward Direction for 510 GeV Polarized  $pp$  Collisions,” [Phys. Rev. D](#) **98** no. 3, (2018) 032013, [arXiv:1805.09745 \[hep-ex\]](#).
- [121] <https://nnpdf.mi.infn.it/>.